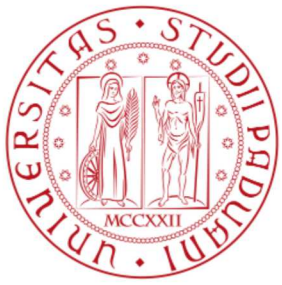

UNIVERSITÀ DEGLI STUDI DI PADOVA

Dipartimento di Fisica e Astronomia "Galileo Galilei"

Master Degree in Physics

Final Dissertation

On Non-Linear Wave-Plasma Interaction in the NORTH Tokamak

Thesis supervisor

Dr. Gianluigi Serianni

Thesis co-supervisors

Prof. Stefan Kragh Nielsen

Dr. Mads Givskov Senstius

Candidate

Nicola Lonigro

Academic Year 2020/2021

Abstract

Many are the challenges that need to be addressed on the path to commercial nuclear fusion. A thorough understanding of the heating process is required to model correctly the behaviour of the plasma in magnetic confinement fusion and by testing the models at different sizes, the results can be scaled to reactor size devices. A common method to heat the plasma consists in injecting high-power microwaves at the electron cyclotron frequency (ECRH). Parametric decay instabilities (PDI) can convert part of the heating power into high-power waves at frequencies different from the desired ECRH one. This can introduce losses in the heating system, affect the behaviour of the plasma and damage diagnostic equipment not shielded appropriately. In this work, the parametric decay of the ECRH microwaves at the upper hybrid layer in the NORTH tokamak has been studied. By testing this effect, previously measured on the ASDEX-U tokamak, on NORTH, a much smaller device, it is possible to validate the model on a very different scale. In the first part of the work, predictions on the threshold of the effect and the frequencies of the additional waves generated by the decay are studied using a previously developed analytical model and validated using particle in cell simulations. In the second part of the work, the decay has been experimentally studied on the NORTH tokamak by first developing a radiometer for this purpose and then performing a series of experiments using both the radiometer and a high-frequency Langmuir probe. A threshold ranging from a few 10's to a few 100's of Watts and a low-frequency daughter in the range of 10-30 MHz has been predicted on NORTH, depending on experimental conditions, and the presence of the decay has been validated in the simulations. No clear evidence of the high-frequency daughter could be found measuring either the electromagnetic waves coming out of the plasma with a radiometer or the floating potential fluctuations using a high-frequency Langmuir probe due to the many sources of background in the system. Evidence for the low-frequency daughter has instead been found using the probe and the signal frequency appears to change with the heating power, the pressure and the magnetic field as would be expected.

Contents

Chapter 1

Introduction

Nuclear fusion reactors are part of the solution to the world's increasing power demands and to the necessity of reducing CO_2 emissions in the fight against climate change. Creating a reactor that is able to generate enough power to run its own heating systems as well as put power on the grid has proven challenging and it has been at the center of a very active research field for some decades. In the development of a functioning reactor, it is important to know as much as possible of the physics driving the system to ensure that the predictions made during development are representative of the final product. To this end, many plasma physics experiments have been built around the world to study the system on different scales and then interpolate the results to reactor size machines. When considering the power balance of a reactor the inefficiencies involved in converting the thermal power into electric currents as well as the inefficiencies of the power systems strongly modify the physics requirements for a working reactor. In this work the existence of parametric decay instabilities, a type of non-linear instability that can reduce the efficiency of microwave-based heating systems, is investigated on NORTH, a small tokamak experiment operated by the Plasma Physics and Fusion Energy section of the Technical University of Denmark.

1.1 Nuclear Fusion

Nuclear fusion consists of the fusion of two light nuclei to produce a heavier one, releasing some energy in the process. The typical reactions relevant for this energy production mechanism are

$$
\begin{aligned}
{}^2\mathrm{D} + {}^2\mathrm{D} &\longrightarrow {}^3\mathrm{He} + {}^1\mathrm{n} + 3.27\mathrm{MeV} \\
{}^2\mathrm{D} + {}^2\mathrm{D} &\longrightarrow {}^3\mathrm{T} + {}^1\mathrm{H} + 4.03\mathrm{MeV} \\
{}^2\mathrm{D} + {}^3\mathrm{T} &\longrightarrow {}^4\mathrm{He} + {}^1\mathrm{n} + 17.6\mathrm{MeV}
\end{aligned}
$$

where ^{2}D and ^{3}T are the deuterium and tritium isotopes of hydrogen respectively. The energy released from a single reaction is of the order of a few MeV, which is 6 orders of magnitudes greater than the energy released in typical chemical reactions, on the order of 10 eV. Another great advantage of this mechanism is that deuterium is a natural isotope of hydrogen that can be abundantly found in ocean water, while tritium can be produced on-site from Lithium, another very common element, leading to a virtually unlimited fuel source. The difficulty in realizing this type of process comes from the Coulomb interaction between the bare nuclei, that repel each other due to being both positively charged. To overcome this repulsion, the nuclei must be energetic enough and this can be achieved in two ways: using accelerators or heating the system. While it is quite possible to achieve nuclear fusion using accelerated beams and this is commonly done in nuclear physics studies to probe the interactions governing the nucleus, it is unfeasible to extract energy from the process. Most interactions between the beam and the target will result in elastic scattering, wasting the energy required to accelerate that nucleus. To ensure the nuclei have the possibility to interact many times until one of the interactions results in a fusion process it is necessary to confine the energetic nuclei. This can be achieved using appropriate magnetic fields and the most utilized configuration is the tokamak. In this configuration

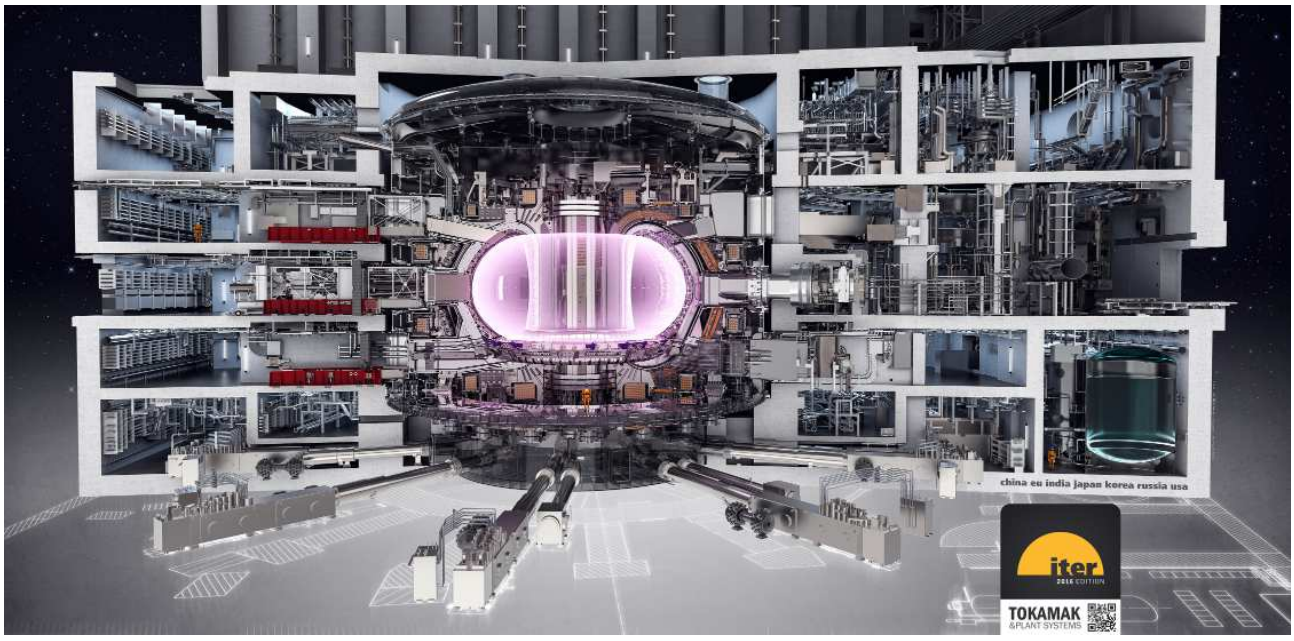

Figure 1.1: The ITER tokamak

a series of toroidally symmetric field coils generate a toroidal field inside the vacuum vessel while a current is driven in the plasma by a central solenoid. The purpose of the plasma current is to generate a poloidal field that reduces radial particle drifts and results in an increased confinement time. A pictorial representation of the ITER tokamak, the largest tokamak in the world currently under construction in Cadaranche (France) is shown in Fig. 1.1.

Among the possible reactions mentioned, the most relevant one and the one that will be actually used in working plants is the fusion of deuterium and tritium. By comparing the cross sections, shown in Fig. 1.2, it is clear that between the fusion reactions of light nuclei the D-T reaction has a much higher cross section at lower temperatures, increasing the energy output at the reactor-relevant temperatures of a few tens of keV's.

By balancing the power inputs and losses it is possible to determine a good metric for the design of a reactor, the so-called "triple product". In the region of temperatures of interest, a criterion for a viable reactor [2] is given by

$$nT\tau_E > 3 \times 10^{21} \frac{\text{skeV}}{\text{m}^3} \tag{1.1}$$

where n is the density of the plasma, T its temperature measured in keV and τ_E the energy confinement time. Much of the current research is focused on increasing τ_E but to have an efficient reactor design it is also of great importance that the power used to heat the plasma is used efficiently. To achieve the required triple product an efficient heating system that is able to meet the required temperature of tens of keVs is needed and it will be the topic of the next section.

1.2 Heating Systems in Nuclear Fusion Reactors

In a conventional tokamak the current driven through the plasma by the central solenoid, required to produce the confining magnetic field, will also act as a heating source through ohmic heating transferring to the plasma a power

$$P \propto I^2 R \tag{1.2}$$

It is impossible, however, to reach fusion relevant temperatures through ohmic heating alone, as the resistivity of the plasma drops with the temperature but losses increase with it, following the Spitzer expression

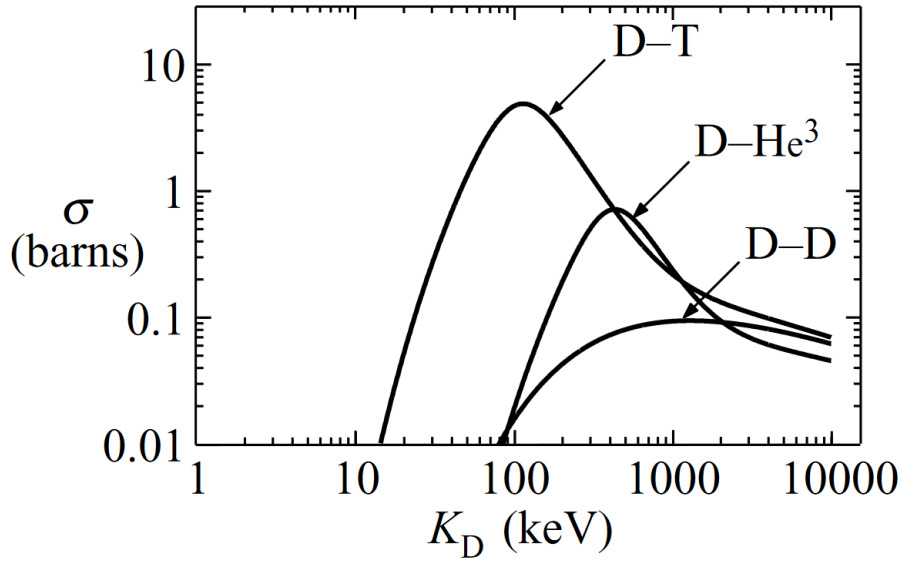

Figure 1.2: Cross sections of fusion reactions between light nuclei with $K_D = \frac{1}{2}mv^2$ the kinetic energy of the deuteron. [1]

$$\eta(\Omega\mathrm{m}) = 1.65 \times 10^{-9} \frac{\ln\Lambda}{T_e(\mathrm{keV})^{\frac{3}{2}}} \tag{1.3}$$

where $ln\Lambda \approx 10$ is the Coulomb logarithm. Typical temperatures that can be reached using ohmic heating alone are of a few keVs [2] and so additional heating systems are required. The two main other mechanisms to heat a plasma are

- Neutral beam injection
- Heating via injected electromagnetic waves

In neutral beam injection the plasma is heated via collisions with hot neutrals that are accelerated and injected in the plasma in the form of a highly energetic beam. The neutrals are not affected by the magnetic fields and so they are able to penetrate inside the plasma where they are quickly ionized and become trapped by the fields so that they can continue to cede their energy to the plasma via collisions. To generate a highly energetic neutral beam, due to the unresponsiveness of neutrals to electric fields, it is necessary to produce and accelerate a beam of ions which can then be neutralized while keeping its inertia before entering the plasma.
The last heating mechanism consists in injecting electromagnetic waves inside the plasma, where the wave can be dampened and cede its energy to heat the system. This can take different forms depending on the specific resonant mechanism used, with the main ones being

- Electron Cyclotron Resonance Heating (ECRH)
- Ion Cyclotron Resonance Heating (ICRH)
- Lower Hybrid Resonance Heating (LH)

The first two of these methods consist in using microwaves that couple to the electron and ion cyclotron resonances, respectively defined by

$$\omega_{ce} = \frac{eB}{m_e} \qquad\qquad \omega_{ci} = \frac{eB}{m_i} \tag{1.4}$$

Due to the dependency on the magnetic field and the variation of the field inside the tokamak ($B \propto R^{-1}$), it is possible to heat the plasma at a desired depth by choosing the frequency of the

heating wave. This allows for direct heating of the core of the plasma but can also be used to target other areas of the plasma to prevent the rise of specific instabilities. It is also possible to target higher harmonics of the cyclotron frequency ($\omega \approx n\omega_c$) but the coupling efficiency drops when using higher harmonics. Typical frequencies in medium-size devices are of 50-100 MHz for ICRH and 100-200 GHz for ECRH. A more in-depth discussion of ECRH is given in the next section. LH waves usually use frequencies of a few GHz [2] and are also used for current drive. The physical mechanism exploited in this process is called *Landau Damping* and leads to the acceleration of electrons traveling with the same velocity as the phase velocity of the waves, meaning that the electric field felt by the electron is always in the same direction. The use of alternative ways to drive the required current in the tokamak is an active field of research and the injection of high power microwaves is a promising approach to achieve a current drive mechanism suitable for steady-state operation.

1.3 Electron Cyclotron Resonance Heating

ECRH is a very common heating mechanism, used for example in the DIII-D and ASDEX-U tokamaks as well as in stellarators such as Wendelstein-7X. It is also planned for ITER to rely heavily on it. Typical heating powers are of a few MW and are injected from the low field side (from regions of higher radius towards regions of lower radius). While the system targets only the electrons they will quickly thermalize with the ions via collisions for reasonable density values. The mathematical description of the electromagnetic waves traveling in the plasma will be covered in chapter 2 but to understand the heating mechanism it is enough for now to mention that the waves can be injected perpendicularly to the magnetic field with two different types of polarization: X-mode or O-mode. The actual heating happens when the waves of the corresponding frequency reach either the electron cyclotron resonance, one of its harmonics or the upper hybrid resonance. X-waves injected from the low field side cannot reach the upper hybrid resonance as between the injection point and the resonance there is a region where X-waves cannot propagate. This leads to the use of either second-harmonic X-waves, as the second harmonic is located at lower magnetic fields, before the evanescence region is reached, or fundamental O-waves [2]. Injected heating waves are not necessarily absorbed during their first pass through the plasma and may be reflected from the walls many times. When injecting O-waves from the low field side, part of the wave may be converted into an X-wave when reflecting on a wall and the conversion fraction depends on the angle of reflection. This conversion will be stronger the first time the waves are reflected from a wall, as the amplitude of the wave becomes lower and lower while traveling through the plasma, and for waves injected from the low field side this will usually be the inner wall. The X-waves generated at the inner wall start from a region with high field and are able to reach both the fundamental cyclotron resonance and the upper hybrid resonance directly, without passing through any evanescent region. This mechanism is known as O-X heating scheme. As will be discussed in chapter 2, when reaching the upper hybrid resonance the X-waves can also be converted into electron Bernstein waves. These waves can also be absorbed by the plasma at the electron cyclotron frequency and are a different heating channel, known as O-X-B scheme. A schematic representation of the different mechanisms in a 1D representation is shown in Fig.1.3

It is worth stressing the fact that the resonances are surfaces physically located at different radial positions and it is at those radial positions that the heating takes place.

1.4 The NORTH Tokamak

NORTH [3] is a small tokamak put into operation in 2019 at the Technical University of Denmark. It was originally created as the ST-25 tokamak by the private company Tokamak Energy in the UK and then subsequently permanently lent to the university as a device intended both for training the next generation of fusion scientists and for research on basic plasma physics, new diagnostics and fusion-related problems. The vacuum vessel is composed of 4 stainless steel quadrants, each with 5 diagnostics ports. One of the ports on the high field side is equipped with a stationary microwave launcher used for ECRH heating while an additional port on the low field side is equipped with a steerable microwave launcher. The magnetic field is given by 8 toroidal field coils that can carry a

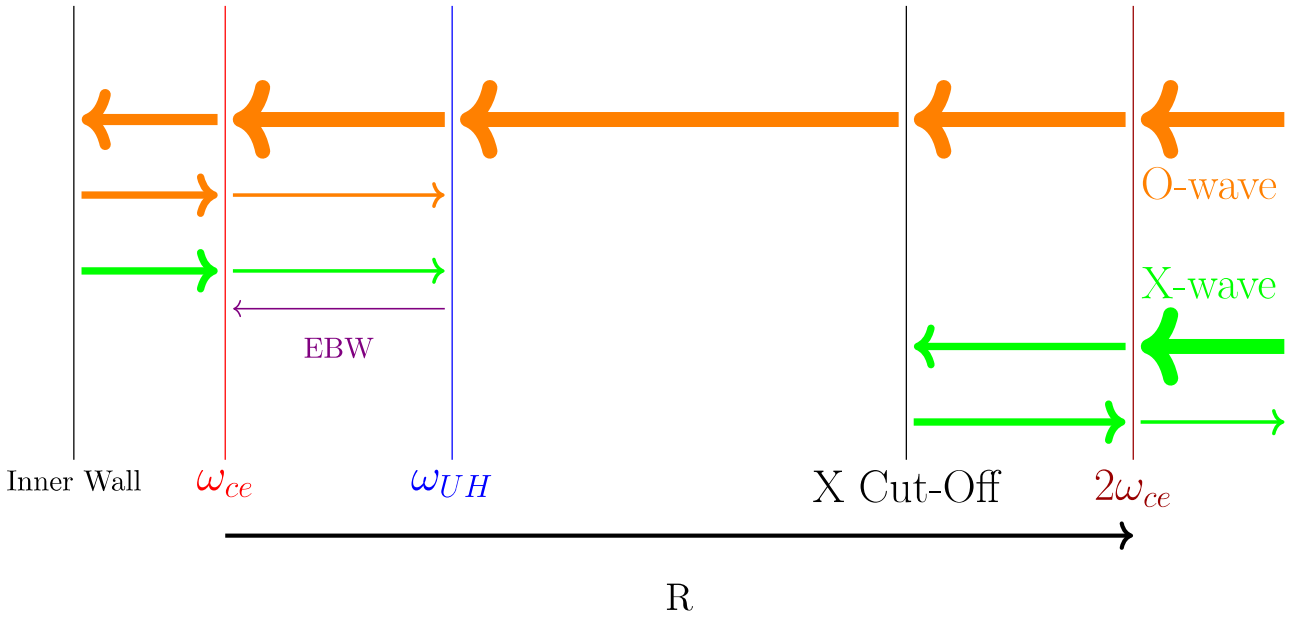

Figure 1.3: 1D Schematic representation of the ECRH heating schemes. The green and orange arrows represent the X and O waves respectively. Injecting from the low field side O waves leads to their partial conversion into X waves and then from X waves into Elecron Berstein Waves (EBW). Alternatively X waves at the 2nd harmonic can be used as they will be absorbed at the resonance before reaching the cutoff.

Parameters	
Major radius (**R**)	0.25 m
Minor radius (**a**)	0.125 m
On-axis field (**B**)	0.4 T
RF heating power	7 kW
Central temperature ($\mathbf{T_e}$)	10-20 eV
Central density ($\mathbf{n_0}$)	0.1 - 1 $\times 10^{17} m^{-3}$

Table 1.1: NORTH parameters

current of up to 5 kA and 6 poloidal field coils, all wound from copper cable. The central solenoid is made up of 128 turns and is operated using an 11 kV power supply. The heating system is composed of two 2.45 GHz magnetrons of 3 kW each. The one mounted on the high field side is operated in X mode while the one mounted on the low field side is operated in O mode to avoid the X mode cutoff. It is this possibility to heat the plasma from the high field side directly in X mode that makes NORTH an optimal environment to study non-linear processes involving this type of waves, such as parametric decay. A picture of the device is shown in Fig. 1.4, while the main parameters are given in Tab. 1.1

1.5 Parametric Decay Instabilities

Parametric decay is a non-linear process consisting of a pump wave decaying into two daughter waves if the amplitude of the initial wave exceeds a certain threshold. This effect can be observed in many instances, for example in mechanical systems [5], in non-linear optical crystals [6] and, as in the case of interest for this work, in plasma physics [7]. An example of parametric instability in mechanics is the simple system of a child on a swing [8]. By tugging on the rope and shortening the effective length of the swing to only the bottom section of the rope twice each period it is possible to transfer energy to the oscillation at the natural frequency of the swing. From this periodic modulation of the system parameter, in this case the swing length, the parametric decay instability takes its name. This type of process does not happen with any frequency but the modulation and the natural frequency

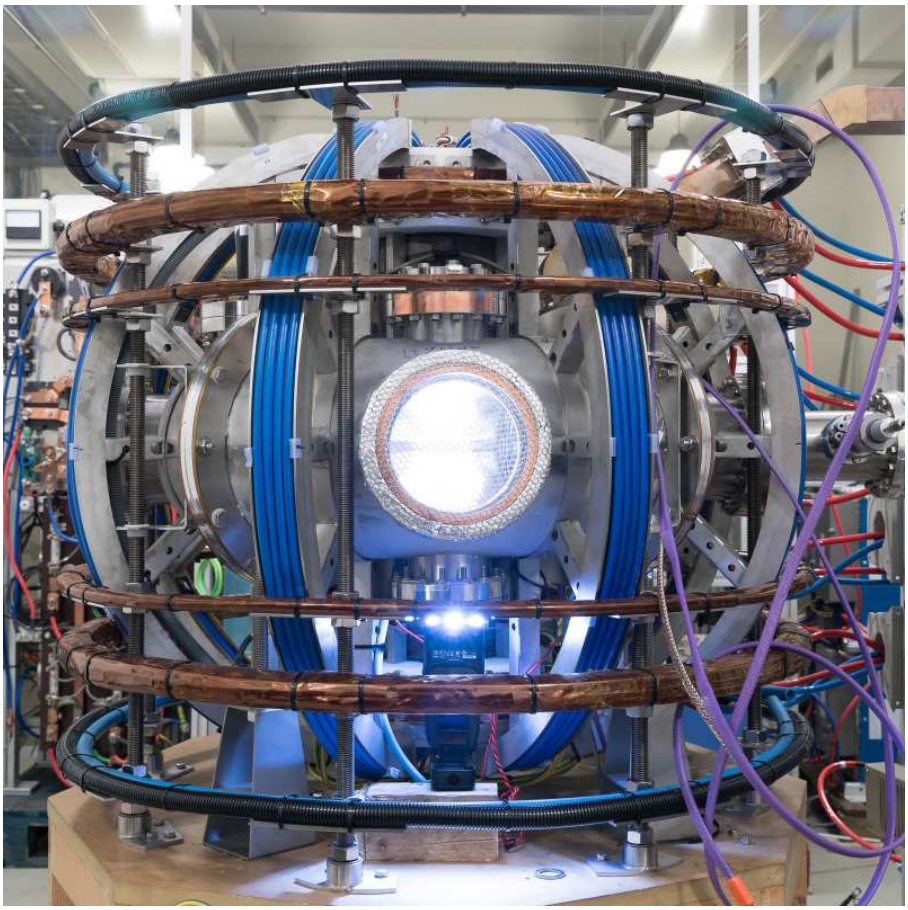

Figure 1.4: The NORTH tokamak [4]

of the system must satisfy a phase-matching condition. These selection rules, which can also be seen as the requirement of conservation of energy and momentum, can be expressed for the decay of an electromagnetic wave as

$$\omega_0 = \omega_1 + \omega_2 \qquad \mathbf{k_0} = \mathbf{k_1} + \mathbf{k_2} \tag{1.5}$$

where the subscript 0 refers to the pump wave and the subscript 1 and 2 to the daughter waves.
The daughter waves will have to be natural frequencies of the system, which in the case of a plasma means that they must correspond to one of the possible types of waves that can propagate inside the plasma and satisfy the related dispersion relations between ω and $\mathbf{k}$. Two related types of decays will be investigated in this work. ECRH microwaves can decay into a low-frequency wave characterized by $(\omega_1, \mathbf{k_1})$ and a down-shifted high-frequency daughter wave characterized by $(\omega_2, \mathbf{k_2})$. The low-frequency wave may then interact non-linearly with the pump wave to create an up-shifted high-frequency wave characterized by $(\omega_3, \mathbf{k_3})$ and in this case, the selection rules become

$$\omega_3 = \omega_0 + \omega_1 \qquad \mathbf{k_3} = \mathbf{k_0} + \mathbf{k_1} \tag{1.6}$$

These types of processes are shown schematically in Fig .1.5.

It is predicted that certain types of parametric decays can lead to effective power losses of the ECRH heating system of up to 10% [9] in the case of second harmonic heating. Furthermore, they can lead to suprathermal ion populations [10] and to damage to the diagnostics that are unshielded from the frequencies of the daughter waves [11] and so it is important to fully understand these types of instabilities. The three waves involved in the process are of three different types: the pump wave is an electromagnetic X wave, the high-frequency daughter wave is an electron Bernstein wave and the low-frequency daughter is a lower hybrid wave. These types of waves and the respective dispersion relations will be discussed in chapter 2.
As previously mentioned parametric decay is a process with an amplitude threshold for the pump

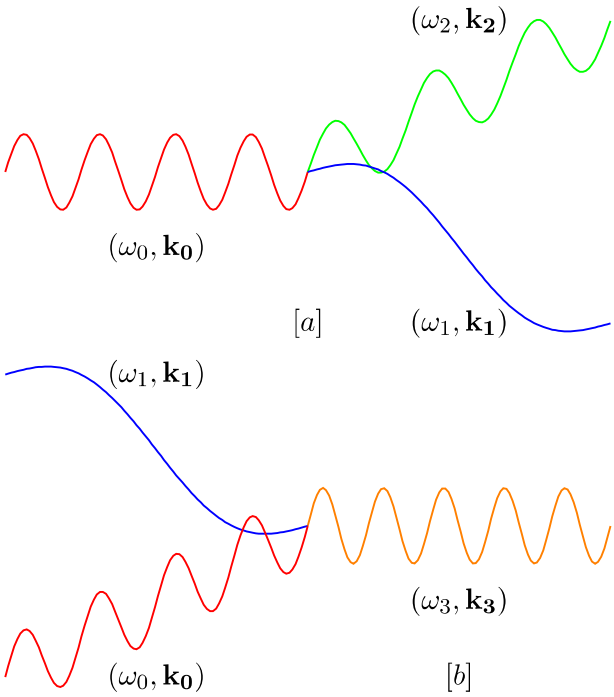

Figure 1.5: Pictorial representation of the two parametric processes. [a] The decay of the pump wave into the two daughter waves. [b] The recombination of the low-frequency daughter wave with the pump wave to form the up-shifted high-frequency daughter wave.

wave. In practice, this threshold is not reached in most of the volume of typical tokamaks but the instability can be triggered when there is a reduction of the threshold, as when the wave is trapped in non-monotonic plasma profiles [12] or when the pump approaches the upper-hybrid layer and the wave amplitude is enhanced. The study of the latter case in the NORTH tokamak is the topic of this work and the specifics regarding the field amplification and the parametric decay threshold are treated in chapter 2. This process has been observed experimentally as a shift of $\approx$ 850MHz of the 105 GHz ECRH microwaves on the ASDEX Upgrade tokamak that was measured by the Collective Thompson Scattering diagnostic. A model to describe this specific process was developed [13] [14] and it will be used to make predictions for the expected results on NORTH in chapter 3. These predictions will then be validated using particle in cell simulations in chapter 4.

1.6 Experimental Set-Up

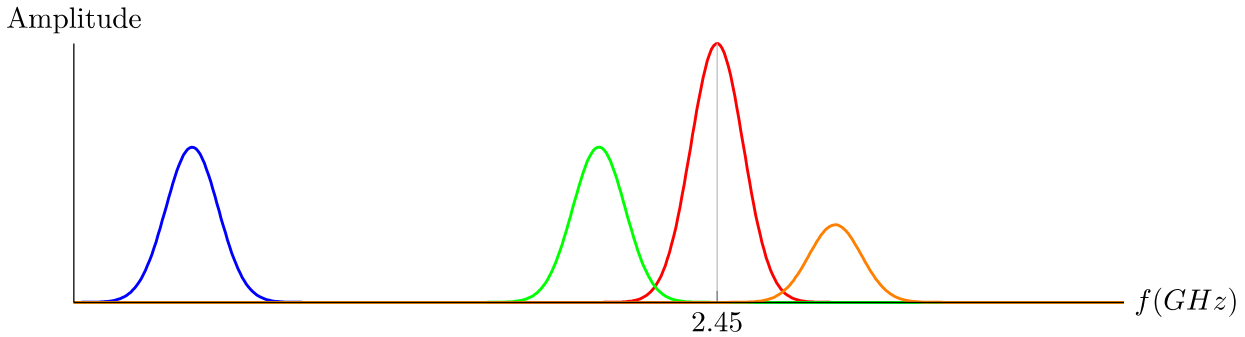

Figure 1.6: Pictorial representation of the spectrum resulting from the parametric decay of the pump wave (red) in the high-frequency daughter (green) and low-frequency daughter (blue) along with the recombination of the low-frequency daughter with the pump wave (orange).

The spectrum of the measured signal after the decay will be composed of the main pump wave,

a low-frequency daughter, a down-shifted high-frequency daughter and an up-shifted high-frequency daughter. A pictorial representation where none of the quantities are to scale is shown in Fig.1.6

It is necessary to measure all of these waves as well as the plasma parameters in order to compare the results with the model. The plasma temperature and density can be measured via Langmuir probes, a standard tool in the field of plasma physics, while the magnetic field can be computed from the current in the toroidal field coils and the Biot-Savart law. To this set of diagnostics, already present on the experiment, a radiometer was added. It was developed to measure the electromagnetic waves coming out of the plasma using a commercial antenna and an analog electronic chain ending up in a Red Pitaya board for the data acquisition. The radiometer design and commissioning will be described in chapter 5 as well as the working principles of the other diagnostics used in the data analysis. The experiments performed during the thesis, that will measure the parametric decay in a variety of experimental conditions, and the related data analysis will be described in chapter 6 and 7.

Chapter 2

Parametric decay at the Upper-Hybrid layer

The large variety of possible waves that can propagate inside a plasma is covered by many standard texts [8] [15]. The process of interest for this work is the parametric decay of X waves into electron Bernstein waves and lower hybrid waves that can happen at the Upper-Hybrid layer. The theory describing these types of waves is outlined in the following sections, where their dispersion relations are derived. In the last section, the electric field threshold needed to trigger the instability is obtained.

2.1 Linear Cold Plasma Theory

The simplest description for the propagation of waves in a plasma is given by the theory of linear waves in a homogeneous cold plasma. In particular, we can define a *cold* plasma as a quasi-neutral collection of charges where the thermal motion of the electrons can be neglected. Considering a non-relativistic system, as appropriate for a tokamak, the response of the charges is to follow the electric field of the driving electromagnetic wave that is propagating inside the plasma.
The system in question will be described by Maxwell's equations coupled to the equation of motion for each species. Considering the motion of the single charges, the equations can be written as

$$\boldsymbol{\nabla} \cdot \mathbf{E}(\mathbf{r}, t) = \sum_j \frac{n(\mathbf{r}, t) q_j}{\epsilon_0} \tag{2.1}$$

$$\boldsymbol{\nabla} \cdot \mathbf{B}(\mathbf{r}, t) = 0 \tag{2.2}$$

$$\boldsymbol{\nabla} \times \mathbf{E}(\mathbf{r}, t) = -\frac{\partial \mathbf{B}(\mathbf{r}, t)}{\partial t} \tag{2.3}$$

$$\boldsymbol{\nabla} \times \mathbf{B}(\mathbf{r}, t) = \mu_0 \left(\mathbf{j}(\mathbf{r}, t) + \epsilon_0 \frac{\partial \mathbf{E}(\mathbf{r}, t)}{\partial t} \right) \tag{2.4}$$

$$m_j \frac{\mathrm{d}\mathbf{v}_j(t)}{\mathrm{d}t} = q_j \left(\mathbf{E}(\mathbf{r}, t) + \mathbf{v}_j(t) \times \mathbf{B}(\mathbf{r}, t) \right) \tag{2.5}$$

where the index j runs over all the species and the current density is given by the motion of the charges, characterized by a mean velocity $\mathbf{u}_j(\mathbf{r}, t)$

$$\mathbf{j}(\mathbf{r}, t) = \sum_j n_j(\mathbf{r}, t) q_j \mathbf{u}_j(\mathbf{r}, t) \tag{2.6}$$

The wave equation can be derived by taking the curl of (2.3) and using (2.4) along with the vector identity $\boldsymbol{\nabla} \times \boldsymbol{\nabla} \times \mathbf{A} = \boldsymbol{\nabla}(\boldsymbol{\nabla} \cdot \mathbf{A}) - \nabla^2(\mathbf{A})$

$$\boldsymbol{\nabla}(\boldsymbol{\nabla} \cdot \mathbf{E}(\mathbf{r}, t)) - \nabla^2(\mathbf{E}(\mathbf{r}, t)) = -\mu_0 \left[\frac{\partial \mathbf{j}(\mathbf{r}, t)}{\partial t} + \epsilon_0 \frac{\partial^2 \mathbf{E}(\mathbf{r}, t)}{\partial t^2} \right] \tag{2.7}$$

By now taking the Fourier transform, or equivalently assuming

$$\mathbf{E}(\mathbf{r},t) = \mathbf{E}_1 e^{i(\mathbf{k}\cdot\mathbf{r}-\omega t)} \tag{2.8}$$
$$\mathbf{B}(\mathbf{r},t) = \mathbf{B}_0 + \mathbf{B}_1 e^{i(\mathbf{k}\cdot\mathbf{r}-\omega t)} \tag{2.9}$$
$$\mathbf{v}(\mathbf{r},t) = \mathbf{v}_1 e^{i(\mathbf{k}\cdot\mathbf{r}-\omega t)} \tag{2.10}$$
$$\tag{2.11}$$

and substituting these expressions in eq. (2.7)

$$-\mathbf{k}\otimes\mathbf{k}\cdot\mathbf{E}(\mathbf{r},t) + k^2\mathbf{E}(\mathbf{r},t) = i\mu_0\omega\mathbf{j}(\mathbf{r},t) + \frac{\omega^2}{c^2}\mathbf{E}(\mathbf{r},t) \tag{2.12}$$

where $\otimes$ denotes the tensor product while $\mathbf{B}_0$ is the static magnetic field and it is conventionally assumed in the z-direction.
An expression for $\mathbf{j}$ in terms of $\mathbf{E}$ can be found by substituting the assumptions (2.80 - 2.10) in the equation of motion for the charges (2.5), which leads, neglecting the second-order terms, to

$$-i\omega m_j \mathbf{v}_{1j} = q_j\left(\mathbf{E}_1 + \mathbf{v}_{1j}\times\mathbf{B}_0\right) \tag{2.13}$$

The solution of this equation can be written in matrix form as

$$\mathbf{v}_j(\mathbf{r},t) = \frac{iq_j}{m_j\left(\omega^2-\omega_{cj}^2\right)}\begin{pmatrix} \omega & i\mathrm{sign}(q_j)\omega_{cj} & 0 \\ -i\mathrm{sign}(q_j)\omega_{cj} & \omega & 0 \\ 0 & 0 & \frac{\left(\omega^2-\omega_{cj}^2\right)}{\omega} \end{pmatrix}\cdot\mathbf{E}(\mathbf{r},t) \tag{2.14}$$

where the cyclotron frequency for species j is defined as $\omega_{cj} = \frac{|q_j|B_0}{m_j}$. By substituting $\mathbf{v}_j(\mathbf{r},t)$ in eq (2.6) the desired expression is found

$$\mathbf{j}(\mathbf{r},t) = \sum_j \frac{iq_j^2 n_j}{m_j\left(\omega^2-\omega_{cj}^2\right)}\begin{pmatrix} \omega & i\mathrm{sign}(q_j)\omega_{cj} & 0 \\ -i\mathrm{sign}(q_j)\omega_{cj} & \omega & 0 \\ 0 & 0 & \frac{\left(\omega^2-\omega_{cj}^2\right)}{\omega} \end{pmatrix}\cdot\mathbf{E}(\mathbf{r},t) \coloneqq \sigma(\mathbf{r},t)\cdot\mathbf{E}(\mathbf{r},t) \tag{2.15}$$

where $\sigma(\mathbf{r},t)$ is the conductivity tensor. Using $\sigma(\mathbf{r},t)$, the wave equation (2.12) can be written

$$\left[\mathbf{k}\otimes\mathbf{k} - k^2\mathbb{I} + i\mu_0\omega\sigma(\mathbf{r},t) + \frac{\omega^2}{c^2}\mathbb{I}\right]\cdot\mathbf{E}(\mathbf{r},t) = 0 \tag{2.16}$$

In order for this equation to have a solution, the determinant of the matrix must be null. Substituting the expression $\mathbf{k} = \frac{\omega\mathbf{n}}{c}$, considering $\mathbf{n}$ to lie in the x-z plane and using the notation adopted by Stix [15] this can be written in the form

$$\det\begin{pmatrix} S-n^2\cos^2\theta & -iD & n^2\cos\theta\sin\theta \\ iD & S-n^2 & 0 \\ n^2\cos(\theta)\sin(\theta) & 0 & P-n^2\sin^2\theta \end{pmatrix} = 0 \tag{2.17}$$

where θ is the angle between k and the magnetic field. Recalling the definition of the plasma frequency for species j, $\omega_{pj} \coloneqq \sqrt{\frac{n_j q_j^2}{m_j\epsilon_0}}$, the relevant terms are defined as

$$S \coloneqq \frac{1}{2}(R+L) = 1 - \sum_j \frac{\omega_{pj}^2}{\omega^2 - \omega_{cj}^2} \tag{2.18}$$

$$D \coloneqq \frac{1}{2}(R-L) = \sum_j \frac{\mathrm{sign}(q_j)\omega_{cj}\omega_{pj}^2}{\omega(\omega^2 - \omega_{cj}^2)} \tag{2.19}$$

$$P \coloneqq 1 - \sum_j \frac{\omega_{pj}^2}{\omega^2} \tag{2.20}$$

$$R \coloneqq 1 - \sum_j \frac{\omega_{pj}^2}{\omega(\omega + \mathrm{sign}(q_j)\omega_{cj})} \tag{2.21}$$

$$L \coloneqq 1 - \sum_j \frac{\omega_{pj}^2}{\omega(\omega - \mathrm{sign}(q_j)\omega_{cj})} \tag{2.22}$$

$$\tag{2.23}$$

to which the labels Sum, Difference, Plasma, Right and Left terms can be given. This leads to the **cold plasma dispersion relation** (CPDR)

$$\left(S\sin^2\theta + P\cos^2\theta\right)n^4 - \left(RL\sin^2\theta + PS\left(1+\cos^2\theta\right)\right)n^2 + PRL = 0 \tag{2.24}$$

with solutions

$$n^2 = \frac{\left(RL\sin^2\theta + PS\left(1+\cos^2\theta\right)\right) \pm \left(\left(RL\sin^2\theta + PS\left(1+\cos^2\theta\right)\right)^2 - 4\left(S\sin^2\theta + P\cos^2\theta\right)PRL\right)^{\frac{1}{2}}}{2\left(S\sin^2\theta + P\cos^2\theta\right)} \tag{2.25}$$

The interesting features of this expression are the cut-offs ($n = 0$) and the resonances ($n \longrightarrow \infty$). Cut-offs indicate the wave is not able to propagate further and is reflected back while resonances can lead to absorption, reflection or mode conversion. Of particular interest for this work is the mode conversion between X mode waves and electron Bernstein waves that is covered in section 2.2. Considering now for simplicity the case of a plasma composed of electrons and a single ion species, some relevant features of this expression can be shown. It is worth mentioning that for $\theta = 0$ the solutions simplify to the so-called Right and Left waves

$$n_R^2 = R = 1 - \frac{\omega_{pe}^2}{\omega(\omega - e\omega_{ce})} - \frac{\omega_{pi}^2}{\omega(\omega + q_i\omega_{ci})} \tag{2.26}$$

$$n_L^2 = L = 1 - \frac{\omega_{pe}^2}{\omega(\omega + e\omega_{ce})} - \frac{\omega_{pi}^2}{\omega(\omega - q_i\omega_{ci})} \tag{2.27}$$

that have resonances respectively for $R \longrightarrow \infty$ and $L \longrightarrow \infty$, corresponding to $\omega = \omega_{ce}$ and $\omega = \omega_{ci}$. These correspond to the electron and ion cyclotron resonances used for heating mentioned in section (1.3). Of more interest for this work is the propagation in the perpendicular direction with respect to the magnetic field ($\theta = \frac{\pi}{2}$) which leads to the so called Ordinary wave and the eXtra-ordinary wave

$$n_O^2 = P = 1 - \frac{\omega_{pe}^2}{\omega^2} - \frac{\omega_{pi}^2}{\omega^2} \tag{2.28}$$

$$n_X^2 = \frac{RL}{S} = \frac{\left[(\omega+\omega_{ci})(\omega-\omega_{ce}) - \omega_{pe}^2 - \omega_{pi}^2\right]\left[(\omega-\omega_{ci})(\omega+\omega_{ce}) - \omega_{pe}^2 - \omega_{pi}^2\right]}{\left(\omega^2-\omega_{ci}^2\right)\left(\omega^2-\omega_{ce}^2\right) + \left(\omega_{pi}^2+\omega_{pe}^2\right)\left(\omega_{ce}\omega_{ci} - \omega^2\right)} \tag{2.29}$$

It can be immediately seen that the O wave has a cut-off at the frequency $\omega = \sqrt{\omega_{pi}^2 + \omega_{pe}^2} \approx \omega_{pe}$, corresponding to P = 0, where the approximation is justified as $\frac{\omega_{pe}}{\omega_{pi}} = \sqrt{\frac{m_i}{m_e}} \approx 42$ for the lightest ion. The resonances for the X mode can be obtained by setting the denominator to zero ($S = 0$), which leads to

$$\omega^2 = \frac{\omega_{pe}^2 + \omega_{ce}^2 + \omega_{pi}^2 + \omega_{ci}^2}{2} \pm \left[\left(\frac{\omega_{pe}^2 + \omega_{ce}^2 - \omega_{pi}^2 - \omega_{ci}^2}{2} \right)^2 + \omega_{pe}^2 \omega_{pi}^2 \right]^{\frac{1}{2}} \tag{2.30}$$

Neglecting terms of the order of $\frac{m_e}{m_i}$ the two solutions are called Upper Hybrid (UH) resonance and Lower Hybrid resonance

$$\omega_{UH}^2 = \omega_{pe}^2 + \omega_{ce}^2 \tag{2.31}$$

$$\omega_{LH}^2 = \omega_{ce}\omega_{ci} \left(\frac{\omega_{pe}^2 + \omega_{ce}\omega_{ci}}{\omega_{pe}^2 + \omega_{ce}^2} \right) \tag{2.32}$$

The Upper Hybrid layer is of particular interest, as the focus of this work is the parametric decay of X waves near the UH resonance. The cut-offs for X mode can be obtained by setting the numerator to zero, that is either $R = 0$ or $L = 0$, resulting in

$$\omega_X = \left[\left(\frac{\omega_{ce} + \omega_{ci}}{2} \right)^2 + \omega_{pe}^2 + \omega_{pi}^2 \right]^{\frac{1}{2}} \pm \frac{\omega_{ce} - \omega_{ci}}{2} \tag{2.33}$$

In particular, expanding the root of the "+" solution in the low-density limit, where $\omega_{pe} \ll \omega_{ce}$, and recalling that $\omega_{ci} \ll \omega_{ce}$ leads to

$$\omega_X \approx \omega_{ce} + \frac{\omega_{pe}^2}{\omega_{ce}} \tag{2.34}$$

while in the high-density limit the "-" solution leads to

$$\omega_X \approx \omega_{pe} - \frac{1}{2}\omega_{ce} \tag{2.35}$$

2.1.1 The CMA Diagram

The different information regarding the cut-offs and resonances can be represented in a convenient graphical way in the Clemmow-Mullaly-Allis (CMA) diagram, shown in figure 2.1.

The quantity $\frac{\omega_{ce}}{\omega}$ is plotted on the Y-axis, which is proportional to the magnetic field and scales inversely with ω while on the X-axis the quantity $\frac{\omega_{pe}^2}{\omega^2}$, proportional to the density, is shown. The path of a wave traveling in an inhomogeneous plasma will be given by a curve in the diagram, characterized by the density profile and magnetic field profile of the plasma and the trajectory of the beam. It is important to notice that the O wave can only propagate on the left side of the diagram, before the O cut-off, and that the X wave cannot propagate in the region between the X cut-off ($R = 0$) and the X resonance ($S = 0$). This means that the Upper hybrid resonance cannot be reached by injecting an X wave from the low-field side and that complicates the study of the parametric decay of interest experimentally. Typically the microwaves used for ECR heating are injected from the low field side, as the inner side is more difficult to reach. In those cases, an O wave, which can cross the region where X waves cannot propagate, is injected from the low field side and the heating happens through the coupling mechanisms that convert it to an X wave through collisions with the vacuum vessel walls on the high field side or when reaching the O cut-off at $X = 1$. NORTH provides the interesting possibility of injecting the microwaves directly from the high field side and so study the parametric decay directly, without the need for conversion mechanisms.

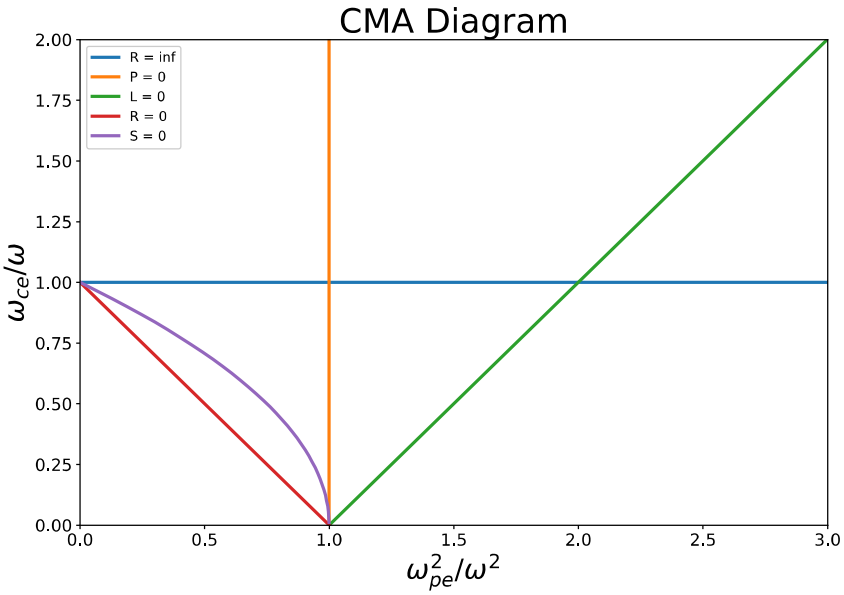

Figure 2.1: The CMA diagram, representing the main resonances and cutoffs in the high frequency region. The blue line represents the electron cyclotron resonance and the purple line the UH resonance. The red line is the X mode cutoff and the orange line the O mode cutoff

2.1.2 X Wave Polarization

Focusing now on the X mode in particular, the behaviour of the polarization and of the group velocity when approaching the UH resonance will be discussed next. Starting from the wave equation (2.16), which can be written in matrix form using the matrix in (2.17), and assuming $\mathbf{k} \perp \mathbf{B}(\theta = \frac{\pi}{2})$, the equation for a general electromagnetic wave can be written as

$$\begin{pmatrix} S & -iD & 0 \\ iD & S - n^2 & 0 \\ 0 & 0 & P - n^2 \end{pmatrix} \cdot \begin{pmatrix} E_x \\ E_y \\ E_z \end{pmatrix} = 0 \tag{2.36}$$

that for an X wave, using (2.29), becomes

$$\begin{pmatrix} S & -iD & 0 \\ iD & \frac{S^2 - RL}{S} & 0 \\ 0 & 0 & \frac{SP - RL}{S} \end{pmatrix} \cdot \begin{pmatrix} E_x \\ E_y \\ E_z \end{pmatrix} = 0 \tag{2.37}$$

and noting that $S^2 - RL = D^2$, this leads to

$$E_x = -\frac{iD}{S} E_y \tag{2.38}$$

$$E_z = 0 \tag{2.39}$$

Thus for X waves, unlike in the case of O waves, the electric field oscillates in the plane perpendicular to the magnetic field. Notice also that the UH layer is defined by the condition $S = 0$, leading to a divergence in the expression and a field completely polarized in the x-direction, which is the direction of propagation of the wave. Near the resonance the X wave behaves as a longitudinal wave and as will be discussed in section 2.2 this is also true for electron Bernstein waves. The polarization plot in Fig. 2.2 shows the ratio of the component along $\mathbf{k}$ and the one perpendicular to both $\mathbf{k}$ and $\mathbf{B}$ for a beam traveling in the radial direction of an inhomogeneous plasma with a Gaussian density profile. The resonance in the expression is visible as the peak in the polarization.

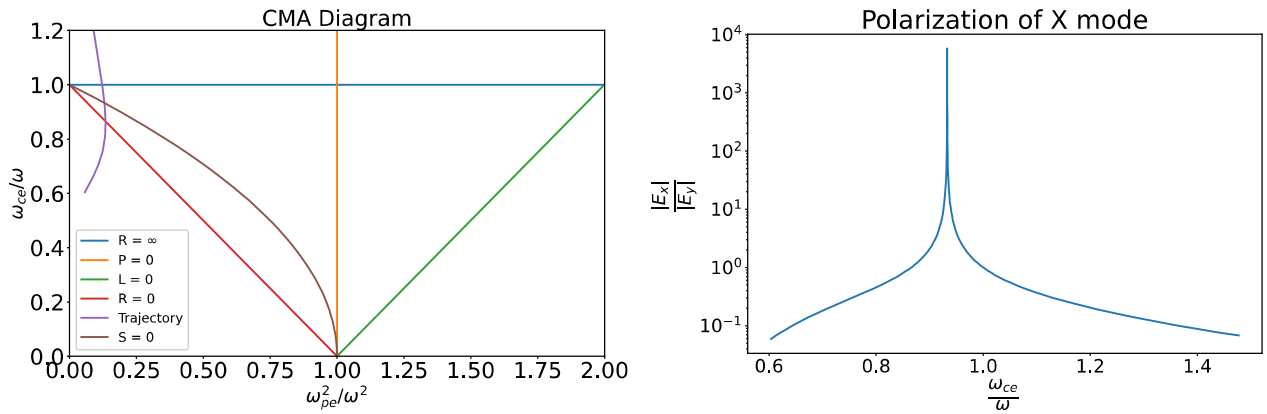

(a) In purple the trajectory in the CMA diagram of the X-waves travelling in an inhomogenous plasma

(b) Polarization of an X wave along the trajectory in the CMA diagram

Figure 2.2: X waves polarization along a trajectory in a homogeneous plasma. The X waves become polarized along **k** near the UH resonance

2.1.3 Field Amplification Near the UH Resonance

Parametric decay is a threshold effect as the electric field needs to be high enough for this non-linear effect to become relevant. To determine the power threshold of the heating system, it is necessary to determine how the electric field varies when traveling through the plasma. For this purpose, assuming the wave enters the plasma with a known intensity profile I(r) and that it remains constant during the propagation, the relation with the electric field is given through the wave energy density $U(\mathbf{r}, t)$ by [13]

$$I(\mathbf{r}) = U(\mathbf{r}, t)|\mathbf{v_g}(\mathbf{r}, \mathbf{k_0}, \omega_0, t)| \tag{2.40}$$

where $\mathbf{v_g}$ is the group velocity, the velocity with which the envelope of a wave packets moves through space, while $\mathbf{k_0}$ is the value of $\mathbf{k}$ where the wave group is centered in $\mathbf{k}$-space with its respective value of ω, ω_0. The group velocity can be obtained in general from

$$\mathbf{v_g} = \frac{\partial \omega}{\partial \mathbf{k}}\Big|_{\mathbf{k_0}} \tag{2.41}$$

A general dispersion relation can be written in the form $\mathcal{D}(\mathbf{k}, \omega) = 0$. Taking the derivative in $\mathbf{k}$ gives

$$\frac{\partial \mathcal{D}(\mathbf{k}, \omega)}{\partial \mathbf{k}} + \frac{\partial \mathcal{D}(\mathbf{k}, \omega)}{\partial \omega}\frac{\partial \omega}{\partial \mathbf{k}} = 0 \tag{2.42}$$

from which

$$\mathbf{v_g} = \frac{\partial \omega}{\partial \mathbf{k}} = -\frac{\partial \mathcal{D}(\mathbf{k}, \omega)}{\partial \mathbf{k}}\left(\frac{\partial \mathcal{D}(\mathbf{k}, \omega)}{\partial \omega}\right)^{-1} \tag{2.43}$$

An expression for $U(\mathbf{r}, t)$ in terms of the electric field can be deduced from the energy continuity equation that can be written, neglecting the dependencies to simplify the notation, as

$$\boldsymbol{\nabla} \cdot \mathbf{P} = -\frac{\partial \mathbf{U}}{\partial t} \tag{2.44}$$

where $\mathbf{P} = (\mathbf{E} \times \mathbf{H})$ is the Poynting vector. Using the vector identity $\boldsymbol{\nabla} \cdot (\mathbf{E} \times \mathbf{H}) = (\boldsymbol{\nabla} \times \mathbf{E}) \cdot \mathbf{H} - \mathbf{E} \cdot (\boldsymbol{\nabla} \times \mathbf{H})$ and Maxwell's equations in a medium

$$\frac{\partial \mathbf{U}}{\partial t} = \left(\mathbf{H} \cdot \frac{\partial \mathbf{B}}{\partial t} + \mathbf{E} \cdot \frac{\partial \mathbf{D}}{\partial t} \right) \tag{2.45}$$

it immediately holds that

$$(\boldsymbol{\nabla} \times \mathbf{E}) \cdot \mathbf{H} - \mathbf{E} \cdot (\boldsymbol{\nabla} \times \mathbf{H}) = - \left(\mathbf{H} \cdot \frac{\partial \mathbf{B}}{\partial t} + \mathbf{E} \cdot \frac{\partial \mathbf{D}}{\partial t} \right) \tag{2.46}$$

Following [8] it is possible to describe the fields in terms of their Fourier amplitudes and allowing ω to have an imaginary part ($\omega = \omega_r + i\omega_i$), a generic field can be written as

$$\mathbf{A}(t) = \mathrm{Re}\left[\hat{\mathbf{A}}\left(\omega\right) e^{-i\int_{\infty}^{t} \omega(t')\mathrm{d}t'} \right] \tag{2.47}$$

and the product between two fields $[\mathbf{A}(t)]\,[\mathbf{B}(t)]$, that may be either a scalar product or a vector product, becomes

$$\begin{aligned}
[\mathbf{A}(t)]\,[\mathbf{B}(t)] =& \mathrm{Re}\left[\hat{\mathbf{A}} e^{-i\int_{-\infty}^{t} \omega(t')\mathrm{d}t'} \right] \mathrm{Re}\left[\hat{\mathbf{B}} e^{-i\int_{-\infty}^{t} \omega(t')\mathrm{d}t'} \right] \\
=& \frac{1}{2}\left[\hat{\mathbf{A}} e^{-i\int_{-\infty}^{t} \omega(t')\mathrm{d}t'} + \hat{\mathbf{A}}^* e^{i\int_{-\infty}^{t} \omega^*(t')\mathrm{d}t'} \right] \frac{1}{2}\left[\hat{\mathbf{B}} e^{-i\int_{-\infty}^{t} \omega(t')\mathrm{d}t'} + \hat{\mathbf{B}}^* e^{i\int_{-\infty}^{t} \omega^*(t')\mathrm{d}t'} \right] \\
=& \frac{1}{4}\left(\left[\hat{\mathbf{A}}\right]\left[\hat{\mathbf{B}}\right] e^{-2i\int_{-\infty}^{t} \omega(t')\mathrm{d}t'} + \left(\left[\hat{\mathbf{A}}^*\right]\left[\hat{\mathbf{B}}\right] + \left[\hat{\mathbf{A}}\right]\left[\hat{\mathbf{B}}^*\right] \right) e^{2\int_{-\infty}^{t} \omega_i(t')\mathrm{d}t'} \right) + \\
& \frac{1}{4}\left(\left[\hat{\mathbf{A}}^*\right]\left[\hat{\mathbf{B}}^*\right] e^{2i\int_{-\infty}^{t} \omega^*(t')\mathrm{d}t'} \right)
\end{aligned} \tag{2.48}$$

where the ω dependencies have been omitted for simplicity.

By integrating over a period $T = \frac{2\pi}{\omega_r}$ and assuming $\omega_i \ll \omega_r$ the first and last term can be neglected, leading to

$$[\mathbf{A}(t)]\,[\mathbf{B}(t)] = \frac{1}{4}\left(\left(\left[\hat{\mathbf{A}}^*\right]\left[\hat{\mathbf{B}}\right] + \left[\hat{\mathbf{A}}\right]\left[\hat{\mathbf{B}}^*\right] \right) e^{2\int_{-\infty}^{t} \omega_i(t')\mathrm{d}t'} \right) \tag{2.49}$$

So (2.45) becomes

$$\frac{\partial \mathbf{U}}{\partial t} = \frac{1}{4}\left[i\omega \hat{\mathbf{H}} \cdot \hat{\mathbf{B}}^* - i\omega \hat{\mathbf{H}}^* \cdot \hat{\mathbf{B}} + i\omega\epsilon_0 \hat{\mathbf{E}} \cdot \left(\mathbf{K} \cdot \hat{\mathbf{E}} \right)^* - i\omega\epsilon_0 \hat{\mathbf{E}}^* \cdot \left(\mathbf{K} \cdot \hat{\mathbf{E}} \right) \right] e^{2\int_{-\infty}^{t} \omega_i(t')\mathrm{d}t'} \tag{2.50}$$

with $\mathbf{K}$ the dielectric tensor defined by

$$\mathbf{j} - i\omega\epsilon_0 \mathbf{E} \coloneqq -i\omega\epsilon_0 \mathbf{K} \cdot \mathbf{E} \tag{2.51}$$

$$\mathbf{K} = \mathbb{I} - \frac{\sigma}{i\omega\epsilon_0} \tag{2.52}$$

Noting that $\hat{\mathbf{E}} \cdot \left(\mathbf{K} \cdot \hat{\mathbf{E}} \right)^* = \hat{\mathbf{E}}^* \cdot \mathbf{K}^\dagger \cdot \hat{\mathbf{E}}$ and defining the Hermitian and anti-Hermitian portions of K

$$\mathbf{K}_h \coloneqq \frac{1}{2}\left(\mathbf{K} + \mathbf{K}^\dagger \right) \qquad\qquad \mathbf{K}_a \coloneqq \frac{1}{2i}\left(\mathbf{K} - \mathbf{K}^\dagger \right) \tag{2.53}$$

eq. (2.50) can be rewritten as

$$\frac{\partial \mathbf{U}}{\partial t} = \frac{1}{4}\left[2\omega_i \mu_0 \hat{\mathbf{H}} \cdot \hat{\mathbf{H}}^* + 2\omega_i \epsilon_0 \hat{\mathbf{E}}^* \cdot \mathbf{K}_h \cdot \hat{\mathbf{E}} + 2\omega_r \epsilon_0 \hat{\mathbf{E}}^* \cdot \mathbf{K}_a \cdot \hat{\mathbf{E}} \right] e^{2\int_{-\infty}^{t} \omega_i(t')\mathrm{d}t'} \tag{2.54}$$

By expanding the dielectric tensor about ω_r to first-order

$$\mathbf{K}(\omega) \approx \mathbf{K}(\omega_r) + \frac{\partial \mathbf{K}}{\partial \omega}\Big|_{\omega_r} i\omega_i \tag{2.55}$$

which leads to

$$\mathbf{K}_a(\omega) = \frac{-i\mathbf{K}(\omega) + i\mathbf{K}^\dagger(\omega^\star)}{2} \approx \mathbf{K}_a(\omega_r) + \omega_i \frac{\partial \mathbf{K}_h}{\partial \omega}\Big|_{\omega_r} \tag{2.56}$$

and substituting this expression in (2.54)

$$\frac{\partial \mathbf{U}}{\partial t} = \frac{1}{4}\left[2\omega_i\left(\mu_0 \hat{\mathbf{H}}\cdot\hat{\mathbf{H}}^* + \epsilon_0 \hat{\mathbf{E}}^*\cdot\frac{\partial}{\partial\omega}\left(\omega\mathbf{K}_h\right)\Big|_{\omega_r}\cdot\hat{\mathbf{E}}\right) + 2\omega_r\epsilon_0\hat{\mathbf{E}}^*\cdot\mathbf{K}_a(\omega_r)\cdot\hat{\mathbf{E}}\right] e^{2\int_{-\infty}^{t}\omega_i(t')\mathrm{d}t'} \tag{2.57}$$

The first term corresponds to the variation of the stored energy, divided between the energy stored in the fields and the kinetic energy of the particles, while the second term is associated to dissipative effects and is related to the anti-Hermitian component of $\mathbf{K}$.

The stored energy can be written as

$$U = \frac{1}{4}\left[\mu_0\hat{\mathbf{H}}\cdot\hat{\mathbf{H}}^* + \epsilon_0\hat{\mathbf{E}}^*\cdot\frac{\partial}{\partial\omega}\left(\omega\mathbf{K}_h\right)\Big|_{\omega_r}\cdot\hat{\mathbf{E}}\right] \tag{2.58}$$

Considering the one-dimensional problem of an X wave propagating with $\mathbf{k}\perp\mathbf{B}$ in a non-absorbing plasma and restricting the problem to a longitudinal wave, as appropriate near the UH layer (Fig. 2.2), (2.16) can be written simply as

$$\mathcal{D}(\mathbf{k},\omega) = K_{11}k^2 = 0 \tag{2.59}$$

Recalling the definition of the conductivity tensor (2.15) and substituting it in the expression for K, this condition becomes

$$\mathcal{D}(\mathbf{k},\omega) = Sk^2 = 0 \tag{2.60}$$

The first term in the energy equation (2.58) is null due to the longitudinal condition ($\mathbf{k}\times\mathbf{E}=0$) and so

$$\begin{aligned} U_X =& \frac{\epsilon_0}{4}\hat{\mathbf{E}}^*\cdot\frac{\partial}{\partial\omega}\left(\omega K\right)\Big|_{\omega_r}\cdot\hat{\mathbf{E}} \\ =& \frac{\epsilon_0}{4}|\mathbf{E}|^2\left(\frac{\omega}{k^2}\frac{\partial\mathcal{D}}{\partial\omega} + \frac{\mathcal{D}}{k^2}\right) \\ =& \frac{\epsilon_0}{4}|\mathbf{E}|^2\frac{\omega}{k^2}\frac{\partial\mathcal{D}}{\partial\omega} \end{aligned} \tag{2.61}$$

where the second term is null from (2.60). Using this result and the expression for the group velocity (2.43), the intensity is given by

$$\begin{aligned} I =& \frac{\partial\mathcal{D}}{\partial k}\left(\frac{\partial\mathcal{D}}{\partial\omega}\right)^{-1}\frac{\epsilon_0}{4}|\mathbf{E}|^2\frac{\omega}{k^2}\frac{\partial\mathcal{D}}{\partial\omega} \\ =& \frac{\epsilon_0}{4}|\mathbf{E}|^2\frac{\omega}{k^2}\frac{\partial\mathcal{D}(\mathbf{k},\omega)}{\partial k} && (2.62) \\ =& \frac{\epsilon_0}{2}|\mathbf{E}|^2\frac{\omega}{k}S && (2.63) \end{aligned}$$

Finally, by inverting the expression, the electric field can be expressed in the cold plasma approximation as

$$|\mathbf{E}|^2 = \frac{2kI}{\epsilon_0\omega S} \tag{2.64}$$

2.2 Hot X Wave and Electron Bernstein Waves

The nonphysical divergences near the UH resonance are removed when taking into account thermal effects. In this framework, the absorption at the electron cyclotron resonances can also be described. The treatment of plasma waves in the kinetic picture is based around using Maxwell's equations coupled to the Boltzmann equation to describe the motion of the particles

$$\frac{\partial f_i\left(\mathbf{r},v,t\right)}{\partial t}+\mathbf{v}\cdot\boldsymbol{\nabla}f_i(\mathbf{r},v,t)+\frac{q_i}{m_i}\left(\mathbf{E}(\mathbf{r},t)+\mathbf{v}\times\mathbf{B}(\mathbf{r},t)\right)\cdot\boldsymbol{\nabla}_{\mathbf{v}}f_i(\mathbf{r},v,t)=\left.\frac{\partial f_i\left(\mathbf{r},v,t\right)}{\partial t}\right|_c \tag{2.65}$$

where $f_i(\mathbf{r},v,t)$ is the distribution function, $\boldsymbol{\nabla}_{\mathbf{v}}$ denotes the derivatives with respect to the velocity and the term on the right-hand side is the collisional operator that accounts for the collisions between particles. The full treatment is lengthy and treated in standard textbooks [8] [15], so only a brief mention of the main points in the derivation is given in the remaining part of the section.

Linear electrostatic waves are in general characterized by a linear dispersion relation

$$\mathrm{Re}[\epsilon(\mathbf{k},\omega_2)]=\mathrm{Re}[1+\chi_i(\mathbf{k},\omega_2)+\chi_e(\mathbf{k},\omega_2)]=0 \tag{2.66}$$

where a single ion species has been assumed and ϵ is the dielectric tensor while χ_e,χ_i are the susceptibility tensors for electrons and ions respectively. For high-frequency waves, the ion response can be neglected, leading to

$$\mathrm{Re}[1+\chi_e(\mathbf{k},\omega)]=0 \tag{2.67}$$

Different assumptions can be made on the distribution function that lead to different expressions for χ_e from (2.65). It has been shown [16] that for a Maxwellian distribution function and particle conserving BGK collision operator the resulting expression is

$$\chi_e(\mathbf{k},\omega)=\frac{2\omega_{pe}^2}{k^2v_{Te}^2}\frac{1+\frac{\omega+i\nu_e}{k_zv_{Te}}\sum_{n=-\infty}^{\infty}I_n(k_\perp^2r_{Le}^2)e^{-k_\perp^2r_{Le}^2}Z\left(\frac{\omega+i\nu_e-n\omega_{ce}}{k_zv_{Te}}\right)}{1+\frac{i\nu_e}{k_zv_{Te}}\sum_{n=-\infty}^{\infty}I_n(k_\perp^2r_{Le}^2)e^{-k_\perp^2r_{Le}^2}Z\left(\frac{\omega+i\nu_e-n\omega_{ce}}{k_zv_{Te}}\right)} \tag{2.68}$$

where ν_e is the electron collision frequency, I_n the modified Bessel function of the first kind of order n and Z the Fried-Conte plasma dispersion function. For the Bernstein waves of interest the propagation is almost perpendicular to $\mathbf{B}$ and so $k_z^2/k_\perp^2\ll1$. Assuming also $\nu_e/\omega\ll1$, $b_e=k_\perp^2r_{Le}^2\ll1$ and $\omega\neq n\omega_{ce}$ the expression can be approximated [13] to first-order in ν_e/ω and $k_z^2/k_\perp^2$ to

$$\chi_e(\mathbf{k},\omega)\approx-\frac{\omega_{pe}}{\omega^2-\omega_{ce}^2}-\frac{3\omega_{pe}^2\omega_{ce}^2b_e}{(\omega^2-\omega_{ce}^2)(\omega^2-4\omega_{ce}^2)}+ \tag{2.69}$$

$$+\frac{\omega_{pe}^2}{\omega^2}\left[\frac{\omega_{ce}^2}{\omega^2-\omega_{ce}^2}+i2\sqrt{\pi}\frac{\omega^3}{k_z^3v_{Te}^3}e^{-\frac{\omega^2}{k_z^2v_{Te}^2}}\right]\frac{k_z^2}{k_\perp^2}+i\frac{\omega_{pe}^2(\omega^2+\omega_{ce}^2)}{(\omega^2-\omega_{ce}^2)^2}\frac{\nu_e}{\omega} \tag{2.70}$$

Thus the dispersion relation can be approximated [17] as

$$\mathcal{D}=l_{Te}^2k_\perp^4+Sk_\perp^2+Pk_z^2-\frac{\omega^2}{c^2}\left(S^2-D^2\right)=0\qquad l_{Te}^2=\frac{3}{2}\frac{v_{Te}^2}{4\omega_{ce}^2-\omega^2}\frac{\omega_{pe}^2}{\omega^2-\omega_{ce}^2} \tag{2.71}$$

That solving for ω leads to [13]

$$\omega_2^2\approx\omega_{UH}^2-\omega_{pe}^2\left[\frac{b_e}{1-\frac{\omega_{pe}^2}{3\omega_{ce}^2}}+\frac{\omega_{ce}^2}{\omega_{UH}^2}\frac{k_z^2}{k_\perp^2}\right] \tag{2.72}$$

Alternatively, it can be shown [8] that electrostatic waves traveling in the perpendicular direction can be described by

$$k^2 = \sum_i 4\frac{\omega_{pi}^2}{v_{ti}^2} e^{-\lambda_i} \sum_{n=1}^{\infty} \frac{I_n(\lambda_i)}{\frac{\omega^2}{n^2\omega_{ci}^2} - 1} \tag{2.73}$$

where I_n is the modified Bessel function of the first kind and $\lambda_i = \frac{k^2\rho_{Li}}{2}$, with ρ_{Li} the Larmor radius of species i. The dispersion relation diverges for every harmonic of the electron and ion cyclotron frequency and in a single ion species plasma, the solutions are usually called either electron Bernstein waves (EBW) or ion Bernstein waves (IBW) depending on the closest resonance. Physically this type of waves is due to the gyration of the charges in a magnetic field as shown in Fig. 2.3. Considering the branch closest to the UH resonance leads to [18]

$$\left(k_\perp^{\pm}\right)^2 = \frac{1}{l_{Te}^2}\frac{S}{2}\left(1 \pm \sqrt{1 - \frac{4Pk_z^2 l_{Te}^2}{S^2} + \frac{4\omega^2}{c^2}\frac{S^2 - D^2}{S^2} l_{Te}^2}\right) \tag{2.74}$$

The two solutions correspond to the "warm" X wave and the electron Bernstein wave and the solutions merge when the argument of the root becomes null. This indicates linear mode conversion between the two types of waves near the upper hybrid layer and as shown in Fig. 2.4, the solutions converge to the cold X wave solution for $T \longrightarrow 0$.

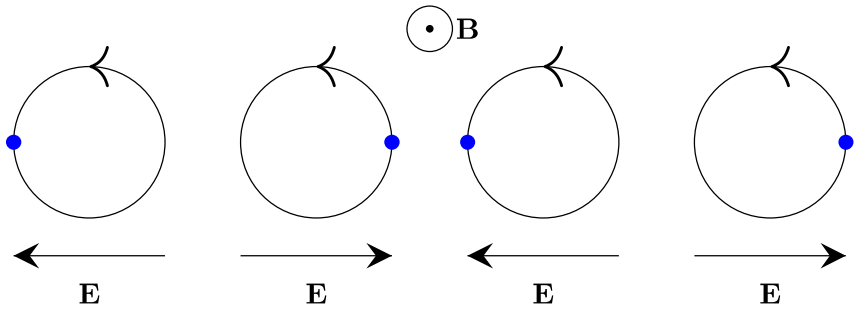

Figure 2.3: Pictorial representation of electron Bernstein waves. Each electron gyrates around a magnetic field line out of phase with the neighbouring electrons, creating an oscillating electric field

2.3 Warm Lower Hybrid Waves

The dispersion relation for the low-frequency daughter wave in the decay can be obtained once again from (2.70) that in this case can be further simplified by neglecting ω_1^2 with respect to ω_{ce}^2.

$$\chi_e(\mathbf{k},\omega_1) \approx \frac{\omega_{pe}^2}{\omega_{ce}^2} - \frac{3\omega_{pe}^2 b_e}{4\omega_{ce}^2} + \frac{\omega_{pe}^2}{\omega_1^2}\left[-1 + i2\sqrt{\pi}\frac{\omega_1^3}{k_z^3 v_{Te}^3} e^{-\frac{\omega_1^2}{k_z^2 v_{Te}^2}}\right]\frac{k_z^2}{k_\perp^2} + i\frac{\omega_{pe}^2}{\omega_{ce}^2}\frac{\nu_e}{\omega_1} \tag{2.75}$$

Due to the low frequency of this daughter wave, the ion response cannot be neglected and an explicit expression for χ_i must be found. By assuming a Maxwellian distribution for the ions, that the collisionality of the ions cannot be neglected ($\nu_i/\omega_1 \geq 1$) and that $\omega_1 \approx \omega_{pi} \gg \omega_{ci}$ so that the ions can be considered as unmagnetized, it can be obtained that [19]

$$\chi_i(\mathbf{k},\omega_1) = \frac{2\omega_{pi}^2}{k^2 v_{Ti}^2}\left[1 + \frac{\omega_1}{kv_{Ti}} Z\left(\frac{\omega_1}{kv_{Ti}}\right)\right] \tag{2.76}$$

Assuming that also in this case it holds $b_e \ll 1$ and that $\omega_1/(kv_{Ti})$ is large enough (≥ 2) to justify an asymptotic expansion in $Z[\omega_1/(kv_{Ti})]$ the resulting expression becomes [13]

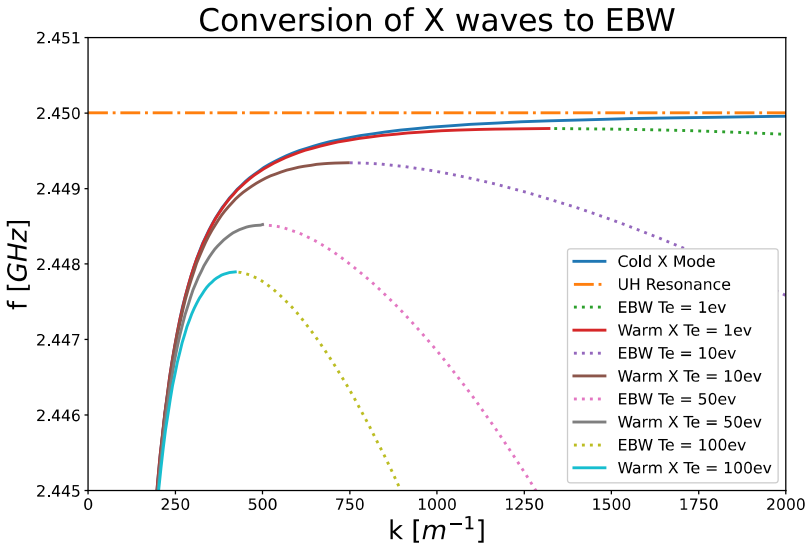

Figure 2.4: Mode conversion between warm X waves and electron Bernstein waves at different temperatures. The full lines represent the X waves dispersion relations while the dotted lines the dispersion relations of the EBW. The two types of dispersion relations join near the UH resonance, the orange line, and one type of wave may convert into the other.

$$\chi_i(\mathbf{k},\omega_1) \approx \frac{\omega_{pi}^2}{\omega_1^2}\left[-1-\frac{3T_i}{Z_iT_e}\frac{\omega_{ci}\omega_{ce}}{\omega_1^2}b_e + i2\sqrt{\pi}\frac{\omega_1^3}{k_\perp^3 v_{Ti}^3}e^{-\frac{\omega_1^2}{k_\perp^2 v_{Ti}^2}}\right] \tag{2.77}$$

with Z_i the charge of the ion. From eq. (2.66) this leads to the dispersion relation

$$1+\frac{\omega_{pe}^2}{\omega_{ce}^2}-\frac{\omega_{pi}^2}{\omega_1^2}-3\left(\frac{\omega_{pe}^2}{4\omega_{ce}^2}+\frac{T_i}{ZT_e}\frac{\omega_{pi}^2\omega_{ci}\omega_{ce}}{\omega_1^4}\right)b_e-\frac{\omega_{pe}^2}{\omega_1^2}\frac{k_z^2}{k_\perp^2}=0 \tag{2.78}$$

That can be written as [13]

$$\omega_1^2 \approx \omega_{LH}^2\left[1+3\left(\frac{\omega_{pe}^2}{4\omega_{UH}^2}+\frac{T_i}{ZT_e}\frac{\omega_{UH}^2}{\omega_{pe}^2}\right)b_e+\frac{m_i}{Z_im_e}\frac{k_z^2}{k_\perp^2}\right] \tag{2.79}$$

2.4 Parametric Decay Instability Threshold

To combine the dispersion relations for the three types of waves involved in the process, an analytic theory of parametric decay is needed. In this section, a more general treatment of the parametric decay of a pump wave is given while in section 2.5 the results are specialized for the decay of interest in this work. A complete derivation is given in [20], leading to analogous results to those previously found by Porkolab [21] [22].

Starting once again from Maxwell's equations and the equation of motion for a particle of species i (2.1) - (2.5), and assuming a harmonic description of the fields, the system can be simplified further using the dipole approximation $\mathbf{k_0} \approx 0$. In the non-relativistic case, the distance traveled by a particle during a wave period is much smaller than the wavelength and the spatial dependencies of the field can be neglected. This is not obvious a priori as it requires that the plane wave can be considered locally constant in the region of interest for the decay but it will be shown later to hold in the case of NORTH. The fields then simplify to

$$\mathbf{E}(\mathbf{r},t) = \mathrm{Re}\left[\mathbf{E_0}e^{i(\mathbf{k_0}\cdot\mathbf{r}-\omega_0 t)}\right] \approx \mathrm{Re}\left[\mathbf{E_0}e^{-i\omega_0 t}\right] \tag{2.80}$$

$$\mathbf{B}(\mathbf{r},t) = \mathrm{Re}\left[\mathbf{B_0}e^{i(\mathbf{k_0}\cdot\mathbf{r}-\omega_0 t)}\right] \approx \mathbf{B_0} \tag{2.81}$$

and the equation of motion can then be written as

$$m_j \frac{\mathrm{d}\mathbf{v_j}(t)}{\mathrm{d}t} = q_j \left(\mathrm{Re}\left[\mathbf{E_0} e^{-i\omega_0 t}\right] + \mathbf{v_j}(t) \times \mathbf{B_0} \right) \tag{2.82}$$

Assuming a harmonic solution for the velocity $\mathbf{v_{j,d}} = \mathrm{Re}\left[\mathbf{v_{j,d0}} e^{-i\omega_0 t}\right]$ and substituting in the equation of motion leads to a particular solution for the inhomogeneous equation

$$\mathbf{v_{j,d0}} = \frac{q_j}{m_j} \begin{pmatrix} \frac{(i\omega_0 E_{0x} - \omega_{j,c} E_{0y})}{(\omega_0^2 - \omega_{j,c}^2)} \\ \\ \frac{(\omega_{j,c} E_{0x} + i\omega_0 E_{0y})}{(\omega_0^2 - \omega_{j,c}^2)} \\ \\ \frac{iE_{0z}}{\omega_0} \end{pmatrix} \qquad \mathbf{r_{j,d}}(t) = \mathrm{Re}\left[\frac{i\mathbf{v_{j,d0}}}{\omega_0} e^{-i\omega_0 t} \right] \tag{2.83}$$

In the kinetic description, assuming the collisions can be neglected and so the right hand side of the Boltzmann equation (2.65) is null, the system is described by the Vlasov equation [22]

$$\frac{\partial f_j(\mathbf{r},\mathbf{v},t)}{\partial t} + \mathbf{v} \cdot \frac{\partial f_j(\mathbf{r},\mathbf{v},t)}{\partial \mathbf{r}} + \frac{q_j}{m_j} \left(\mathbf{E}_{dg} + \mathrm{Re}\left[\mathbf{E_0} e^{-i\omega_0 t}\right] + \mathbf{v} \times \mathbf{B}(\mathbf{r},t) \right) \cdot \frac{\partial f_j(\mathbf{r},\mathbf{v},t)}{\partial \mathbf{v}} = 0 \tag{2.84}$$

where $\mathbf{E}_{dg}$ denotes the electric field of the daughter waves, that are electrostatic and so it holds that

$$\mathbf{E}_{dg}(\mathbf{r},t) = -\frac{\partial \phi}{\partial \mathbf{r}}(\mathbf{r},t) \qquad \frac{\partial}{\partial \mathbf{r}} \cdot \frac{\partial \phi}{\partial \mathbf{r}}(\mathbf{r},t) = -\frac{1}{\epsilon_0} \sum_j q_j n_j(\mathbf{r},t) \tag{2.85}$$

where $\phi(\mathbf{r},t)$ is the potential describing the daughter waves. Substituting in the Vlasov equation leads to

$$\frac{\partial f_j}{\partial t}(\mathbf{r},\mathbf{v},t) + \mathbf{v} \cdot \frac{\partial f_j(\mathbf{r},\mathbf{v},t)}{\partial \mathbf{r}} + \frac{q_j}{m_j} \left(-\frac{\partial \phi}{\partial \mathbf{r}}(\mathbf{r},t) + \mathrm{Re}\left[\mathbf{E_0} e^{-i\omega_0 t}\right] + \mathbf{v} \times \mathbf{B}(\mathbf{r},t) \right) \cdot \frac{\partial f_j(\mathbf{r},\mathbf{v},t)}{\partial \mathbf{v}} = 0 \tag{2.86}$$

Shifting to a frame of reference moving with $\mathbf{r_d}$ and oscillating with velocity $\mathbf{v_d}$ and using the methods of characteristics to solve the corresponding linearised equation leads to the coupled equations [20]

$$\tilde{N}_j^{(1)}(\mathbf{k},\omega) = -\frac{\epsilon_0 k^2}{q_j} \chi_j(\mathbf{k},\omega) \sum_{n=-\infty}^{\infty} J_n(\mu_j) e^{-in\beta_j} \tilde{\phi}(\mathbf{k},\omega + n\omega_0) \tag{2.87}$$

$$\tilde{\phi}(\mathbf{k},\omega) = \sum_j \frac{q_j}{\epsilon_0 k^2} \sum_{n=-\infty}^{\infty} J_n(-\mu_j) e^{-in\beta_j} \tilde{N}_j^{(1)}(\mathbf{k},\omega + n\omega_0) \tag{2.88}$$

$$\beta_j = \arg\left(\frac{\mathbf{k} \cdot \mathbf{v_{j,d0}}}{\omega_0} \right) \tag{2.89}$$

$$\mu_j = \frac{|q_j|}{m_j \omega_0} \left\{ \left[\frac{\omega_0 \,\mathrm{Im}(k_x E_{0x} + k_y E_{0y}) + \omega_{cj} \,\mathrm{Re}(k_x E_{0y} - k_y E_{0x})}{\omega_0^2 - \omega_{cj}^2} + \frac{k_z \,\mathrm{Im}(E_{0z})}{\omega_0} \right]^2 + \left[\frac{\omega_0 \,\mathrm{Re}(k_x E_{0x} + k_y E_{0y}) - \omega_{cj} \,\mathrm{Im}(k_x E_{0y} - k_y E_{0x})}{\omega_0^2 - \omega_{cj}^2} + \frac{k_z \,\mathrm{Re}(E_{0z})}{\omega_0} \right]^2 \right\}^{\frac{1}{2}} \tag{2.90}$$

where $\chi_j(\mathbf{k},\omega)$ is the linear susceptibility for species j, $\tilde{\phi}(\mathbf{k},\omega)$ the Fourier transform of the electrostatic potential, J_n the Bessel function of the first kind of order n and $\tilde{N}^{(1)}(\mathbf{k},\omega)$ the Fourier transform of the density in the new frame of reference. μ_j represents the coupling strength to the Fourier mode indexed by $\mathbf{k}$. It is worth noting that the same expression holds for a weakly collisional plasma if $\chi_j(\mathbf{k},\omega)$ is modified correspondingly [16].
To obtain a more tractable solution some approximations can be made to the previous system of equations. Due to the very different masses of ions and electrons ($\frac{m_i}{m_e} \approx 1836 Z_i$) it generally holds that $\omega_0 \sim \omega_{ce} \gg \omega_{ci}$ and that $\mu_e \gg \mu_i$. Assuming that $\mu_e \leq 1$, this leads to $\mu_i \approx 0$ and by noting that $J_n(\mu_i) \approx J_n(-\mu_i) \approx \delta_{n0}$ the system of equations can be simplified to [20]

$$\left[1 + \sum_i \chi_i(\mathbf{k},\omega)\right] \sum_i Z_i \tilde{N_i}^{(1)}(\mathbf{k},\omega) = \sum_i \chi_i(\mathbf{k},\omega) \sum_{n=-\infty}^{\infty} J_n(-\mu_e) e^{-in\beta_e} \tilde{N_e}^{(1)}(\mathbf{k},\omega + n\omega_0) \tag{2.91}$$

$$\left[1 + \chi_e(\mathbf{k},\omega)\right] \tilde{N_e}^{(1)}(\mathbf{k},\omega) = \chi_e(\mathbf{k},\omega) \sum_{n=-\infty}^{\infty} J_n(\mu_e) e^{-in\beta_e} \sum_i Z_i \tilde{N_i}^{(1)}(\mathbf{k},\omega + n\omega_0) \tag{2.92}$$

A final simplification can be made by noting that $\omega_0 \gg \omega_{pi}$, a condition that it will be seen holds for NORTH, meaning that $|\sum_i \chi_i(\mathbf{k},\omega)| \ll 1$ for $\mathrm{Re}(\omega) \geq \omega_0$ and so the response of the ions to frequencies comparable or higher than the pump wave can be neglected. This means that if ω corresponds to a low-frequency wave, as in the case of lower hybrid waves, all other modes can be neglected ($\sum_i Z_i \tilde{N_i}^{(1)})(\mathbf{k},\omega + n\omega_0) \approx \sum_i Z_i \tilde{N_i}^{(1)}(\mathbf{k},\omega)\delta_{n0}$. By substituting this in the previous expression and expanding $J_n(\mu_e)$ for small μ_e the parametric dispersion relation can be obtained [20]

$$1 + \sum_i \chi_i(\mathbf{k},\omega) + \chi_e(\mathbf{k},\omega) = \frac{\mu_e^2}{4} \sum_i \chi_i(\mathbf{k},\omega) \left[2 - \frac{1 + \chi_e(\mathbf{k},\omega)}{1 + \chi_e(\mathbf{k},\omega - \omega_0)} - \frac{1 + \chi_e(\mathbf{k},\omega)}{1 + \chi_e(\mathbf{k},\omega + \omega_0)}\right] \tag{2.93}$$

Alternatively, this can be expressed in terms $\epsilon(\mathbf{k},\omega)$. Neglecting the 2 on the right-hand side, an assumption that will be justified later, the parametric dispersion relation becomes

$$\epsilon(\mathbf{k},\omega) = -\frac{\mu_e^2}{4} \sum_i \chi_i(\mathbf{k},\omega)[1 + \chi_e(\mathbf{k},\omega)] \left[\frac{1}{\epsilon(\mathbf{k},\omega - \omega_0)} + \frac{1}{\epsilon(\mathbf{k},\omega + \omega_0)}\right] \tag{2.94}$$

in agreement with the results found in previous literature [21] [23]. The physical meaning of this expression is that the lower hybrid wave of frequency ω and $\mathrm{Re}(\omega) = \omega_1$ is coupled to the down-shifted daughter wave of frequency $\omega_2 = -\mathrm{Re}(\omega - \omega_0)$ and the high-shifted daughter wave of frequency $\omega_3 = \mathrm{Re}(\omega + \omega_0)$. For $\mu_e \longrightarrow 0$ the expression tends to the expected linear dispersion relation $\epsilon(\mathbf{k},\omega) = 0$ and the different waves become uncoupled. As previously assumed usually $\mu_e^2 \ll 1$ and so the decay cannot connect any 2 waves, but if the daughter waves correspond to modes of the plasma, their respective dielectric function will tend to zero and the expression can become satisfied. The requirements for small $\epsilon(\mathbf{k},\omega + \omega_0)$ and $\epsilon(\mathbf{k},\omega - \omega_0)$ justifies neglecting the 2 in (2.93).
It is now possible to determine the growth rate of the instability $\gamma = \mathrm{Im}(\omega)$ by Taylor expanding $\epsilon(\mathbf{k},\omega - \omega_0) = \epsilon(\mathbf{k}, -\omega_2 + i\gamma) = \mathrm{Re}[\epsilon(\mathbf{k}, -\omega_2 + i\gamma)] + \mathrm{Im}[\epsilon(\mathbf{k}, -\omega_2 + i\gamma)]$, a reasonable step if the growth is weak so that $\omega_2 \gg |\gamma|$. For the linear mode $\mathrm{Re}[\epsilon(\mathbf{k}, -\omega_2)] = 0$ and as $\mathrm{Re}[\epsilon(\mathbf{k},\omega)]$ is an even function of ω while $\mathrm{Im}[\epsilon(\mathbf{k},\omega)]$ and $\frac{\partial\,\mathrm{Re}[\epsilon(\mathbf{k},\omega)]}{\partial\omega}$ are odd functions of ω, this leads to

$$\epsilon(\mathbf{k}, -\omega_2 + i\gamma) \approx i\gamma \frac{\partial\,\mathrm{Re}[\epsilon(\mathbf{k},\omega)]}{\partial\omega}\bigg|_{-\omega_2} + i\,\mathrm{Im}[\epsilon(\mathbf{k}, -\omega_2)] = -i\left[\gamma + \Gamma(\mathbf{k},\omega_2)\right] \frac{\partial\,\mathrm{Re}[\epsilon(\mathbf{k},\omega)]}{\partial\omega}\Big|_{\omega_2} \tag{2.95}$$

with $\Gamma(\mathbf{k},\omega_2) = \mathrm{Im}[\epsilon(\mathbf{k},\omega_2)] \left(\frac{\partial\,\mathrm{Re}[\epsilon(\mathbf{k},\omega)]}{\partial\omega}\Big|_{\omega_2}\right)^{-1}$. Plugging this expression in (2.94) and assuming that only the down-shifted high frequency wave is on-resonance and so that the term $\epsilon(\mathbf{k},\omega + \omega_0)^{-1}$

can be neglected, two expressions for the growth rate can be obtained. If the low-frequency wave does not correspond to an exact linear plasma mode, for example in the presence of significant Landau damping, the parametric decay is said to be non-resonant and it holds that [20]

$$\gamma = \frac{\mu_e^2}{4} \frac{\left|\sum_i \chi_i(\mathbf{k},\omega_1)\right|^2 \mathrm{Im}[\chi_e(\mathbf{k},\omega_1)] + \left|1+\chi_e(\mathbf{k},\omega_1)\right|^2 \sum_i \mathrm{Im}[\chi_i(\mathbf{k},\omega_1)]}{\left|\epsilon(\mathbf{k},\omega_1)\right|^2 \left(\frac{\partial\,\mathrm{Re}[\epsilon(\mathbf{k},\omega)]}{\partial\omega}\right)\Big|_{\omega_2}} - \Gamma(\mathbf{k},\omega_2) \tag{2.96}$$

In order for the instability to grow γ must be positive and so the threshold of the non-resonant parametric decay instability in a homogeneous plasma is given by

$$\frac{\mu_e^2}{4} \frac{\left|\sum_i \chi_i(\mathbf{k},\omega_1)\right|^2 \mathrm{Im}[\chi_e(\mathbf{k},\omega_1)] + \left|1+\chi_e(\mathbf{k},\omega_1)\right|^2 \sum_i \mathrm{Im}[\chi_i(\mathbf{k},\omega_1)]}{\left|\epsilon(\mathbf{k},\omega_1)\right|^2 \left(\frac{\partial\,\mathrm{Re}[\epsilon(\mathbf{k},\omega)]}{\partial\omega}\right)\Big|_{\omega_2}} > \Gamma(\mathbf{k},\omega_2) \tag{2.97}$$

A more physical picture of the process can be obtained by noting that the instability vanishes with $\mathrm{Im}[\chi_e(\mathbf{k},\omega_1)], \mathrm{Im}[\chi_i(\mathbf{k},\omega_1)] \longrightarrow 0$ and so it can only happen in the presence of damping of the lower frequency mode. As suggested in [24] this can be interpreted as the low-frequency daughter acting to couple the pump wave and the high-frequency daughter through interactions with the plasma and so transferring energy from the pump wave to the other daughter while being Landau damped in the process.

If instead, the low-frequency mode corresponds to an exact linear plasma mode the parametric decay is said to be resonant and $\epsilon(\mathbf{k},\omega_1 + i\gamma)$ can also be expanded and after some algebra the resulting expression becomes [20]

$$\gamma = \frac{1}{2}\left[(\Gamma(\mathbf{k},\omega_1)-\Gamma(\mathbf{k},\omega_2))^2 - \frac{\mu_e^2\,\mathrm{Re}[\sum_i \chi_i(\mathbf{k},\omega_1)(1+\chi_e(\mathbf{k},\omega_1))]}{(\partial\,\mathrm{Re}[\epsilon(\mathbf{k},\omega)]/\partial\omega)\big|_{\omega_1}(\partial\,\mathrm{Re}[\epsilon(\mathbf{k},\omega)]/\partial\omega)\big|_{\omega_2}}\right]^{\frac{1}{2}} - \frac{1}{2}(\Gamma(\mathbf{k},\omega_1)+\Gamma(\mathbf{k},\omega_2)) \tag{2.98}$$

leading to the threshold for the resonant parametric decay in a homogeneous plasma

$$-\frac{\mu_e^2}{4} \frac{\mathrm{Re}[\sum_i \chi_i(\mathbf{k},\omega_1)(1+\chi_e(\mathbf{k},\omega_1))]}{(\partial\,\mathrm{Re}[\epsilon(\mathbf{k},\omega)]/\partial\omega)\big|_{\omega_1}(\partial\,\mathrm{Re}[\epsilon(\mathbf{k},\omega)]/\partial\omega)\big|_{\omega_2}} > \Gamma(\mathbf{k},\omega_1)\Gamma(\mathbf{k},\omega_2) \tag{2.99}$$

Which of the two expressions to use depends on if Landau damping is significant or not, which depends both on plasma conditions and the type of waves under study. In the next section, the discussion is specialized for the case of X waves decaying into lower hybrid waves and electron Bernstein waves using the results from the previous sections.

2.5 Instability Thresholds at the Upper Hybrid Layer

It is now possible to determine the instability thresholds for the specific case of electron Bernstein waves and lower hybrid waves, starting from their respective dispersion relations (2.71) and (2.78). The damping rates can be determined by plugging the dispersion relations in the definition $\Gamma(\mathbf{k},\bar{\omega}) = \mathrm{Im}[\epsilon(\mathbf{k},\bar{\omega})]\left(\frac{\partial\,\mathrm{Re}([\epsilon(\mathbf{k},\omega))}{\partial\omega}\Big|_{\bar{\omega}}\right)^{-1}$, which leads to [20]

$$\Gamma(\mathbf{k},\omega_2) \approx \frac{\omega_2^2+\omega_{ce}^2}{2\omega_2^2}\nu_e \tag{2.100}$$

$$\Gamma(\mathbf{k},\omega_1) \approx \frac{\sqrt{\pi}\omega_1^2}{k_\perp^2 v_{Ti}^2}\left[\frac{\omega_1}{k_\perp v_{Ti}} e^{-\frac{\omega_1^2}{k_\perp^2 v_{Ti}^2}} + \frac{T_i}{Z_i T_e}\frac{\omega_1}{k_z v_{Te}} e^{-\frac{\omega_1^2}{k_z^2 v_{Te}^2}}\right]\omega_1 + \frac{\omega_{pe^2}}{2\omega_{ce}^2}\frac{\omega_1^2}{\omega_{pi}^2}\nu_e \tag{2.101}$$

It is then clear that for the lower hybrid waves Landau damping is significant if $\sqrt{\pi}\frac{\omega_1^3}{k_\perp^3 v_{Ti}^3}e^{-\frac{\omega_1^2}{k_\perp^2 v_{Ti}^2}}$ is large and to determine if this is the case an expression for $\frac{\omega_1^2}{k_\perp^2 v_{Ti}^2}$ is needed in terms of the parameters of the system.
Using the known expression for ω_1 (2.78) and recalling that $b_e = k_\perp^2 r_{Le}^2$

$$\frac{\omega_1^2}{k_\perp^2 v_{Ti}^2} = \frac{Z_i T_e}{2T_i}\frac{\omega_{LH}^2}{\omega_{ci}|\omega_{ce}|}\left[\frac{1}{b_e} + 3\left(\frac{\omega_{pe}^2}{4\omega_{UH}^2} + \frac{T_i}{ZT_e}\frac{\omega_{UH}^2}{\omega_{pe}^2}\right) + \frac{m_i}{Z_i m_e b_e}\frac{k_z^2}{k_\perp^2}\right] \tag{2.102}$$

An expression for b_e can be found by recalling the selection rule (1.5), meaning that it must hold $\omega_2 = \omega_0 - \omega_1$. Plugging in the expression for ω_1 (2.78) and for ω_2 (2.72) and isolating b_e in the assumption of small b_e, small $\frac{k_z^2}{k_\perp^2}$ and $\omega_0 \gg \omega_{LH}$ leads to [20]

$$\frac{1}{b_e} \approx \frac{A_2\omega_{pe}^2 - A_1(\omega_0 - \omega_{LH})\omega_{LH}}{\omega_{UH}^2 - (\omega_0 - \omega_{LH})^2}\left[1 - \frac{(\omega_0 - 2\omega_{LH})\omega_{LH}}{\omega_{UH}^2 - (\omega_0 - \omega_{LH})^2}\frac{m_i}{Z_i m_e}\frac{k_z^2}{k_\perp^2}\right] \tag{2.103}$$

where to simplify the notation A_1 and A_2 have been introduced

$$A_1 = 3\left(\frac{\omega_{pe}^2}{4\omega_{UH}^2} + \frac{T_i}{Z_i T_e}\frac{\omega_{UH}^2}{\omega_{pe}^2}\right) \qquad A_2 = \frac{1}{1 - \frac{\omega_{pe}^2}{3\omega_{ce}^2}} \tag{2.104}$$

By plugging this in (2.102) and noting that near the upper hybrid layer $\omega_0 \approx \omega_{UH}$ it can be shown that [20]

$$\frac{\omega_1}{k_\perp^2 v_{Ti}^2} \approx \frac{Z_i T_e}{4T_i}\frac{\omega_{pe}^3}{\omega_{ce}^3}\frac{1}{1 + \frac{\omega_{pe}^2}{\omega_{ce}^2}}\left(\sqrt{\frac{m_i}{Z_i m_e}}\frac{1 + \frac{m_i}{2Z_i m_e}\frac{k_z^2}{k_\perp^2}}{1 - \frac{\omega_{pe}^2}{3\omega_{ce}^2}} + \frac{3\omega_{pe}}{4\omega_{ce}}\frac{1 - \frac{m_i}{2Z_i m_e}\frac{k_z^2}{k_\perp^2}}{1 + \frac{\omega_{pe}^2}{\omega_{ce}^2}}\right) + \frac{3}{4}\left(1 - \frac{m_i}{2Z_i m_e}\frac{k_z^2}{k_\perp^2}\right) \tag{2.105}$$

As mentioned in section 2.3, the expansion of $Z[\omega_1/(kv_{Ti})]$ used to obtain the ω_2 expression requires $\omega_1/(kv_{Ti}) \geq 2$. This requirement for the validity of the model can be checked using (2.105) and it will be discussed for the case of NORTH in chapter 3. Using this expression is possible to determine if the decay is resonant or not depending on the growth rate (2.101).

The general expressions for γ in the resonant(2.98) and non-resonant (2.96) cases can now be specialized by using the known expressions for χ_e (2.75) and χ_i (2.77). A further simplification can be made considering $\mathbf{E_0}$ to be parallel to $\mathbf{k_0}$, as appropriate near the UH layer, considering once again the case $\frac{k_z}{k_\perp} \ll 1$ and orienting the system so that $\mathbf{k} = [k_\perp, 0, k_z]$. The simplified expression for μ_e (2.90) becomes [13]

$$\mu_e^2 \approx \frac{e^2 k_\perp^2 |E_{0x}|^2}{m_e^2(\omega_0^2 - \omega_{ce}^2)^2}\left(1 + \frac{\omega_{ce}^2}{\omega_0^2}\frac{|E_{0y}|^2}{|E_{0x}|^2}\right) \approx b_e\frac{\omega_{ce}^2|E_{0x}|^2}{\omega_{pe}^2}\frac{\epsilon_0}{N_e^{(0)}T_e}\left(1 + \frac{\omega_{ce}^2}{\omega_{UH}^2}\frac{|E_{0y}^2|}{|E_{0x}|^2}\right) \tag{2.106}$$

To determine the electric field threshold required to trigger the instability it is necessary to find the fastest-growing mode, which can be obtained by maximizing γ. The maximum of μ_e is clearly reached for $E_{0x} = E_{0\perp}, E_{0y} = 0$ leading to

$$\mu_{e,max}^2 \approx b_e\frac{\omega_{ce}^2|E_{0\perp}|^2}{\omega_{pe}^2}\frac{\epsilon_0}{N_e^{(0)}T_e} \tag{2.107}$$

With this expression the growth rate for the non-resonant parametric decay near the upper hybrid layer of an X wave in a lower hybrid wave and an electron Bernstein wave can be expressed as [13]

$$\gamma_{NR,hom} \approx \frac{b_e}{8L_i}\frac{\epsilon_0|E_{0\perp}|^2}{N_e^{(0)}T_e}\omega_{UH} - \frac{\omega_{UH}^2+\omega_{ce}^2}{2\omega_{UH}^2}\nu_e \tag{2.108}$$

where $L_i = 2\sqrt{\pi}\frac{\omega_1^3}{k_\perp^3 v_{Ti}^3}e^{-\frac{\omega_1^2}{k_\perp^2 v_{Ti}^2}}$ is the factor determining the ion Landau damping of the lower hybrid wave. Inverting this expression the non-resonant threshold in a homogeneous plasma can be found

$$|E_{0\perp}|^2_{NR,hom} = \frac{4L_i}{b_e}\frac{(\omega_{UH}^2+\omega_{ce}^2)\nu_e}{\omega_{UH}^3}\frac{N_e^{(0)}T_e}{\epsilon_0} \tag{2.109}$$

Analogously, the growth rate for the resonant parametric decay of an X wave in a lower hybrid wave and an electron Bernstein wave in a homogeneous plasma is given by

$$\gamma_{R,hom} = \frac{1}{2}\left[\left(\frac{L_i}{2}\omega_{LH} - \frac{\omega_{ce}^2}{\omega_{UH}^2}\nu_e\right)^2 + \frac{b_e}{4}\frac{\epsilon_0|E_{0\perp}|^2}{N_e^{(0)}T_e}\omega_{UH}\omega_{LH}\right]^{\frac{1}{2}} - \frac{L_i}{4}\omega_{LH} - \nu_e \tag{2.110}$$

with the corresponding threshold

$$|E_{0\perp}|^2_{R,hom} = \frac{4(L_i + \frac{\omega_{pe}^2}{\omega_{UH}^2}\frac{\nu_e}{\omega_{LH}})}{b_e}\frac{(\omega_{UH}^2+\omega_{ce}^2)\nu_e}{\omega_{UH}^3}\frac{N_e^0 T_e}{\epsilon_0} \tag{2.111}$$

2.5.1 Parametric Decay Instability in Inhomogenous Plasmas

Thresholds in homogeneous plasmas tend to be much smaller than ones in inhomogeneous plasmas as the selection rules are satisfied only in a thin region in a typical tokamak. If the ECRH beam is small enough it can be considered in the context of geometrical optics as concentrated in the center of the actual Gaussian beam and the temporal growth rate in a homogeneous plasma γ can be converted into a spatial one as $\frac{\gamma}{v_g(\mathbf{k},\omega)}$. The power gain $G = \ln\left(\frac{P_{out}}{P_{in}}\right)$ can then be shown to be [25]

$$G = \int_{ray}\frac{2\gamma(\mathbf{r}(s),\mathbf{k}(s),\omega_1,\omega_2)}{v_g(\mathbf{r}(s),-\mathbf{k}(s),\omega_2)}\,\mathrm{d}s \tag{2.112}$$

where the integral is over the ray and s parameterizes the beam trajectory. If the amplification is only significant in a narrow region around $s = s_r$

$$G \approx \frac{2\gamma(\mathbf{r}(s_r),\mathbf{k}(s_r),\omega_1,\omega_2)\mathsf{l}(s_r)}{v_g(\mathbf{r}(s_r),-\mathbf{k}(s_r),\omega_2)} \tag{2.113}$$

with $\mathsf{l}(s_r)$ the typical width where the growth is significant. To trigger the instability the gain must be large enough and this can be conventionally set to $G > 2\pi$ [26].
For a resonant parametric decay in a plasma slab with parameters varying monotonically in the x-direction, it has been shown that in the WKB approximation [13]

$$G_R = \frac{2\pi\gamma(x_r,\mathbf{k_x}(x_r),\omega_1,\omega_2)l^2(x_r,\omega_1,\omega_2)}{v_g(x_r,\mathbf{k_x}(x_r),\omega_1)v_g(x_r,-\mathbf{k_x}(x_r),\omega_2)} \tag{2.114}$$

where $l^2(x_r,\omega_1,\omega_2) = \left|\frac{\partial k_x}{\partial x}(x,\omega_1)\Big|_{x_r} - \frac{\partial k_x}{\partial x}(x,\omega_2)\Big|_{x_r}\right|^{-1}$ is the length scale over which the selection rule for k is satisfied and x_r is the x value for which the selection rules are exactly satisfied. A similar result can be obtained for the non-resonant case by setting $\mathsf{l}(s_r) = l(x_r,\omega_1,\omega_2)$

$$G_{NR} \approx \frac{2\gamma(x_r, \mathbf{k_x}(x_r), \omega_1, \omega_2) l(x_r, \omega_1, \omega_2)}{v_g(x_r, -\mathbf{k_x}(x_r), \omega_2)} \tag{2.115}$$

By plugging in the expressions for the corresponding γ's in the resonant and non-resonant case, recalling the definition for $v_g(\mathbf{k}, \omega)$(2.43) and neglecting the ion damping in the resonant expression it can be obtained [13]

$$G_R \approx \frac{\pi}{8A_1A_2} \frac{\omega_{UH}^2}{\omega_{pe}^2} \frac{l^2}{r_{Le}} \frac{\epsilon_0 |E_{0\perp}|^2}{N_e^{(0)} T_e} \tag{2.116}$$

$$G_{NR} \approx \frac{k_\perp l}{4A_2L_i} \frac{\omega_{UH}^2}{\omega_{pe}^2} \frac{\epsilon_0 |E_{0\perp}|^2}{N_e^{(0)} T_e} \tag{2.117}$$

with the same A_1 and A_2 previously defined (2.5). By now noting that $k_x = k_\perp = \frac{\sqrt{b_e}}{r_{Le}}$, an explicit expression for l in terms of the plasma parameters can be obtained from the known expression for b_e leading to

$$\frac{1}{l^2} \approx \frac{1}{b_e} \left| \left(\frac{\omega_{ce}^2}{A_1\omega_{UH}^2} + \frac{1}{A_2} \right) \frac{1}{2r_{Le}L_N} + \left(\frac{\omega_{pe}^2}{A_1\omega_{UH}^2} + \frac{\omega_{ce}^2}{A_2\omega_{pe}^2} \right) \frac{1}{r_{Le}L_B} \right| \tag{2.118}$$

where L_N and L_B are the gradient scale lengths for the density and the field

$$L_N = \frac{N_e^0(x)}{\frac{\mathrm{d}N_e^{(0)}(x)}{\mathrm{d}x}} \qquad\qquad L_B = \frac{B(x)}{\frac{\mathrm{d}B(x)}{\mathrm{d}x}} \tag{2.119}$$

By now requiring that $G > 2\pi$, the expression for the electric field thresholds for resonant and non-resonant parametric decay in an inhomogeneous plasma are obtained

$$\left|E_{0\perp}^R\right|^2 > \frac{8}{\sqrt{b_e}} \frac{\omega_{pe}^2}{\omega_{UH}^2} \left| \left(\frac{A_2\omega_{ce}^2}{\omega_{UH}^2} + A_1 \right) \frac{r_{Le}}{L_N} + \left(\frac{A_2\omega_{pe}^2}{\omega_{UH}^2} + \frac{A_1\omega_{ce}^2}{\omega_{pe}^2} \right) \frac{2r_{Le}}{L_B} \right| \frac{N_e^0 T_e}{\epsilon_0} \tag{2.120}$$

$$\left|E_{0\perp}^{NR}\right|^2 > \frac{8\pi L_i}{b_e^{\frac{3}{4}}} \frac{\omega_{pe}^2}{\omega_{UH}^2} \sqrt{A_2 \left| \left(\frac{A_2\omega_{ce}^2}{A_1\omega_{UH}^2} + 1 \right) \frac{r_{Le}}{2L_N} + \left(\frac{A_2\omega_{pe}^2}{A_1\omega_{UH}^2} + \frac{\omega_{ce}^2}{\omega_{pe}^2} \right) \frac{r_{Le}}{L_B} \right|} \frac{N_e^0 T_e}{\epsilon_0} \tag{2.121}$$

2.5.2 Power Threshold Determination

The final step consists now in passing from a threshold value for the electric field to a threshold value of the ECRH cyclotron power. Towards this end, it is possible to obtain an order of magnitude estimate by considering the problem of a Gaussian beam closing in to the upper hybrid layer. A Gaussian beam is characterized by an electric field

$$|E_0(\rho, s)| = |E_0(0, s)| e^{-\frac{\rho^2}{W(s)^2}} \tag{2.122}$$

where ρ is the distance from the center of the beam and $W(s)$ is the half-width of the beam. A beam can be considered to be completely contained in a distance of 2-3 times its half-width, which is given by

$$W(s) = W(0)\sqrt{1 + \frac{4c(s-s_0)^2}{\omega_0^2 W_0^4}} \tag{2.123}$$

The beam is then characterized by its trajectory, parameterized by s, the parameter s_0 which is the point of minimum width along the trajectory and W_0, the minimum half-width or waist of the beam.
The power of a beam can be obtained by integrating the intensity over its surface

$$P(s) = 2\pi \int_0^\infty I(\rho, s)\mathrm{d}\rho \tag{2.124}$$

which leads for a Gaussian beam in free space to

$$P(s) = \frac{\pi}{4} c\epsilon_0 |E_0(0,s)|^2 W(s)^2 \tag{2.125}$$

In this case, however, the beam is not traveling in free space and the amplification of the field near the upper hybrid layer described in section 2.1.3 is vital in lowering the threshold to low enough levels to make the decay measurable. From (2.62) it is clear that the electric field is amplified by a factor $\left(\frac{\omega}{k^2}\frac{\partial \mathcal{D}(\mathbf{k},\omega)}{\partial k}\right)^{-\frac{1}{2}}$, that can be obtained in the warm approximation by (2.71) and that makes the power required to reach the threshold electric field

$$P_{th} = \frac{\pi}{4}\epsilon_0 |E_{th}|^2 \frac{\omega}{2k^2}\frac{\partial \mathcal{D}(\mathbf{k},\omega)}{\partial k} W_{UH}^2 = \frac{\pi}{4}\epsilon_0 |E_{th}|^2 \frac{\omega}{2k^2}(4l_{Te}^2 k_\perp^3 + 2k_\perp S + 2Pk_z) W_{UH}^2 \tag{2.126}$$

where W_{UH} is the half-width at the upper hybrid layer and E_{th} is the electric field threshold of the case of interest: resonant or non-resonant, homogeneous or inhomogeneous. The power threshold obtained only refers to the required amount of beam power at the upper hybrid layer, while to obtain a more accurate estimation of the input heating power the absorption of the wave inside the plasma should be taken into account. In the experiments performed at ASDEX this was a necessary step as the wave was initially created as an O wave and only a fraction of the initial power was transformed into an X wave after the collision with the inner wall. In the case of NORTH, where the plasma can be heated from the high field side, this transformation is not required and the waves can enter the plasma already polarized as X waves. To obtained an order of magnitude estimate of the required power (2.126) is considered a good enough approximation for this work but a more accurate estimation could be obtained by relating the required power at the upper hybrid layer to the required input power via

$$P_{UH} = P_{IN} e^{-\tau_{UH}} \tag{2.127}$$

where τ_{UH} is the total optical thickness of the plasma at the upper hybrid layer.

Chapter 3

Parametric decay predictions in NORTH

NORTH can be operated in a variety of operating conditions useful for studying the non-linear effects of interest, ranging from a glow discharge with a flat density profile up to the tokamak configuration with a bell-shaped density profile. This freedom of possible configurations requires a study specific to the NORTH parameters to determine the parametric decay threshold in various operating conditions. Starting from the general theoretical model described in chapter 2, it is now possible to determine the power threshold from (2.126). In the rest of the chapter, it will be instructive to start with a realistic case and to show a step-by-step determination of the respective power threshold and then moving on to a parameter sweep of the most relevant parameters to study the related trends.

3.1 Power Threshold in NORTH: A Case Study

Some reasonable parameters that describe standard operating conditions for NORTH are given in Tab. 3.1.

The magnetic field profile will be given by the standard $\frac{1}{R}$ dependency of a toroidal solenoid while for the density a Gaussian profile can be assumed with a standard deviation of $\sigma = 0.03$ m. The specific density profile used is not too relevant in the determination of the threshold as only the region near the upper hybrid layer is involved in the process and so any profile with the same parameters and gradients near the resonance will result in the same threshold. The field and density profiles for this example are shown in Fig. 3.1 along with the corresponding trajectory in the CMA diagram. In this case, the upper hybrid layer is met where the line describing the beam trajectory in NORTH meets the resonance at S = 0 and so for $\frac{\omega_{ce}}{\omega} = 0.9705$. In the rest of the section, the quantity $Y = \frac{\omega_{ce}}{\omega}$ will often be used to parameterize the curve and so the beam will be considered to be approaching the resonance at $Y = 0.97$ from a high Y value.

The same trajectory can be used to represent the injection of an O wave either from the inner or outer side by just reversing the direction of motion along the curve as no cut-offs for this type of wave are encountered. If the injected wave is of the X type, the wave cannot propagate between the R=0 cut-off and the S=0 resonance. In this instance, only the injection from the high field side is a viable way to reach the resonance and so only the upper part of the trajectory has physical meaning. After

Paramaeters	
On-axis field (**B**)	0.075 T
Electron temperature (T_e)	10 eV
Ion temperature (T_i)	1 eV
Central density (n_0)	0.7 $\times 10^{16}$ m^{-3}
Operating gas	H_2

Table 3.1: NORTH parameters in case study

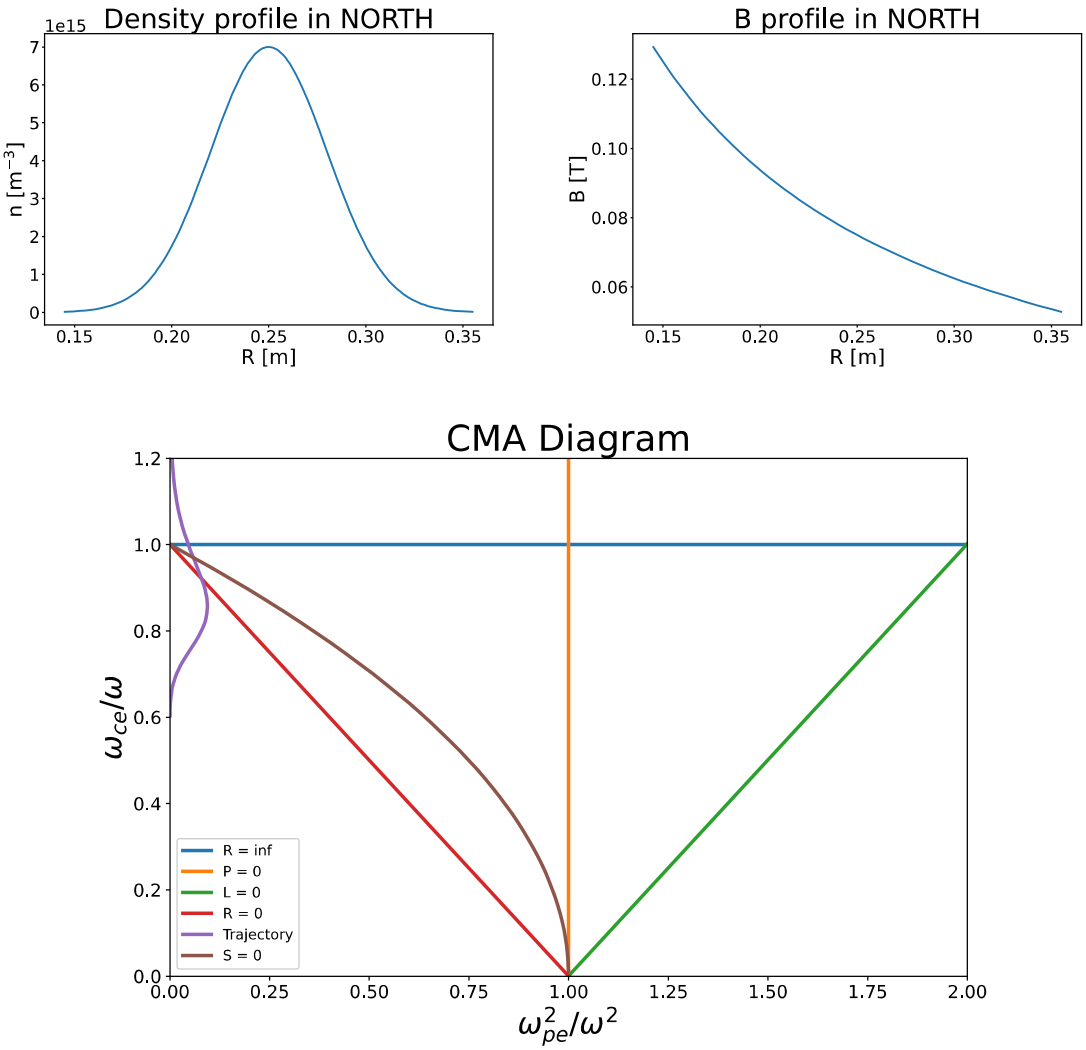

Figure 3.1: Density and field profile with corresponding trajectory in the CMA diagram. The purple line represents the trajectory in the CMA diagram of an X wave injected radially in a plasma with the reported density and magnetic field profiles, representative of the ones in NORTH.

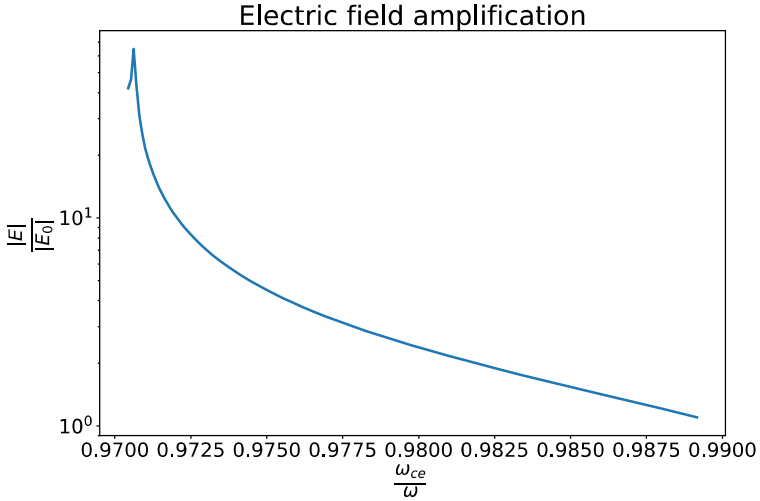

Figure 3.2: Amplification of the electric field of an X wave while traveling towards the UH resonance along the trajectory shown in Fig. 3.1. The wave is assumed injected from the high field side and so from the right of the graph.

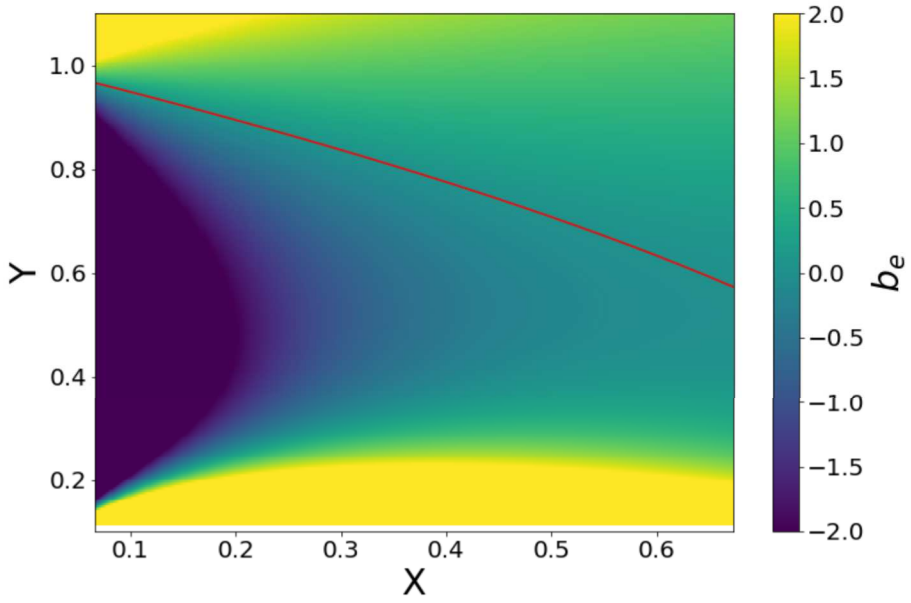

Figure 3.3: Value of b_e in the relevant CMA diagram area with $T_e = 10$ eV and $T_i = 1$ eV. The red line represents the UH resonance. The values of the 2D plot have been capped in the region [-2 : 2] to aid visualization

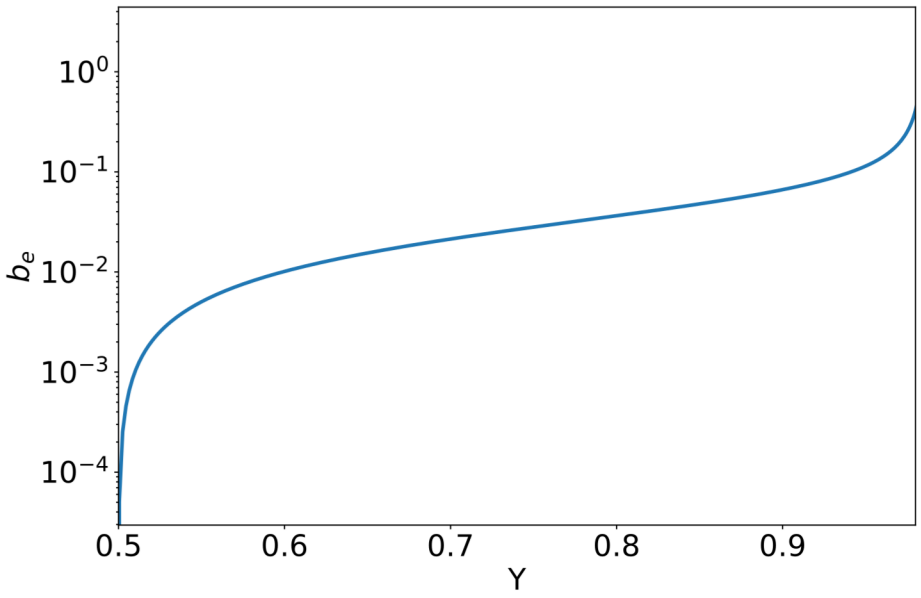

Figure 3.4: Value of b_e along the upper hybrid layer, shown in Fig. 3.3 as a red line

encountering the resonance, as explained in section 2.2, the X wave will be converted in an electron Bernstein wave and reflected in the incoming direction.

Using (2.62) it is possible to determine the amplification of the field along its trajectory in the CMA diagram. Using the dispersion relation for the warm X wave the result is shown in Fig. 3.2, where the trajectory is parameterized by Y.

The electric field is expected to be amplified up to ≈ 65 times its original value and recalling that the power is proportional to the field squared this will lead to a power threshold ≈ 4000 times smaller. Before applying the model to find the power threshold it is necessary to check that the related approximations hold. Starting from $0 < b_e \ll 1$, Fig. 3.3 shows the value of b_e in the relevant area

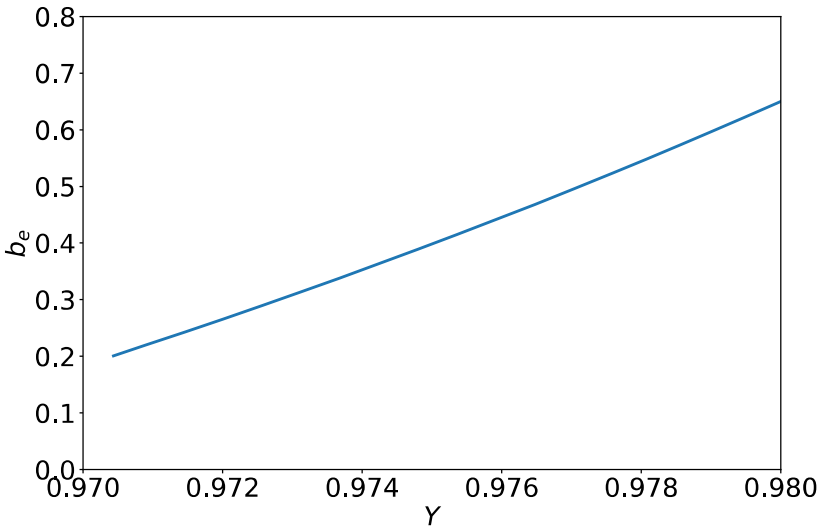

Figure 3.5: Value of b_e along the example beam trajectory in Fig. 3.1 with $T_e = 10$ eV and $T_i = 1$ eV.

Pump Frequency (f_0)	2.450 GHz
Electron Cyclotron Frequency (f_{ce})	2.377 GHz
Ion Cyclotron Frequency (f_{ci})	1.294 MHz
Plasma Frequency (f_{pe})	0.593 GHz
Upper Hybrid Frequency (f_{UH})	2.450 GHz
Lower Hybrid Frequency (f_{LH})	9.488 MHz
EBW daughter Frequency (f_2)	2.436 GHz
LH daughter Frequency (f_1)	13.47 MHz

Table 3.2: Relevant frequencies in the NORTH case study at the UH layer

of the CMA diagram while Fig. 3.4 the value of b_e exactly at the upper hybrid layer, which is also plotted as a red line in the 2D plot.

The approximation can be considered to be valid for all the range of interest and it only breaks down for $Y \longrightarrow 1$ which should be avoided regardless to avoid an overlap of the upper hybrid resonance with the plasma cyclotron resonance. It could be tempting to only show the values of b_e along the upper hybrid layer but in practice the parametric decay does not happen exactly *at* the upper hybrid layer but it can start happening at the first point along the trajectory of the beam where the threshold is met, supposing that the required approximations made in the model hold. To show explicitly this point, in Fig.3.5 the value of b_e when nearing the upper hybrid layer along the trajectory is shown and it is clear that values smaller than one can be reached at a significant distance from the resonance.

By applying the definitions for the cyclotron frequencies, the plasma frequency and the upper and lower hybrid frequencies, along with the equations for the frequencies of the daughter waves (2.79) (2.72), the values of the frequencies involved in the system at the resonance are reported in Tab. 3.2

It is then clear that the approximations depending on $\omega_{ce} \gg \omega_{ci}$ hold very well as expected and $\omega_2 \approx \omega_0, \omega_1 \ll \omega_0$ are reasonable for an order of magnitude estimate. By summing the frequencies for the two daughter waves the pump frequency is obtained once again, proving that the model conserves the energy as expected. Moving on to the requirement mentioned in section 2.3 that $\frac{\omega_1}{kv_{Ti}} \geq 2$, needed to expand $Z(\frac{\omega_1}{kv_{Ti}})$ and obtain the final expression for ω_1. In Fig. 3.6 its value is shown as a function of the frequency ratio $\frac{\omega_{pe}}{\omega_{ce}}$ and the parameter that is assumed small in the derivation $\frac{m_i}{Z_i m_e}\frac{k_{||}^2}{k_z^2}$. The green line in the plot shows the threshold values where $\frac{\omega_1}{kv_{Ti}} = 2$ is satisfied. The area to the right of the threshold line satisfies the condition and as shown this is true for the parameters in NORTH, represented as a red line. The dependence on $\frac{k_{||}^2}{k_z^2}$ is quite weak and the requirement for the condition

to hold can be summarized in $\frac{\omega_{pe}}{\omega_{ce}} > 0.2$.

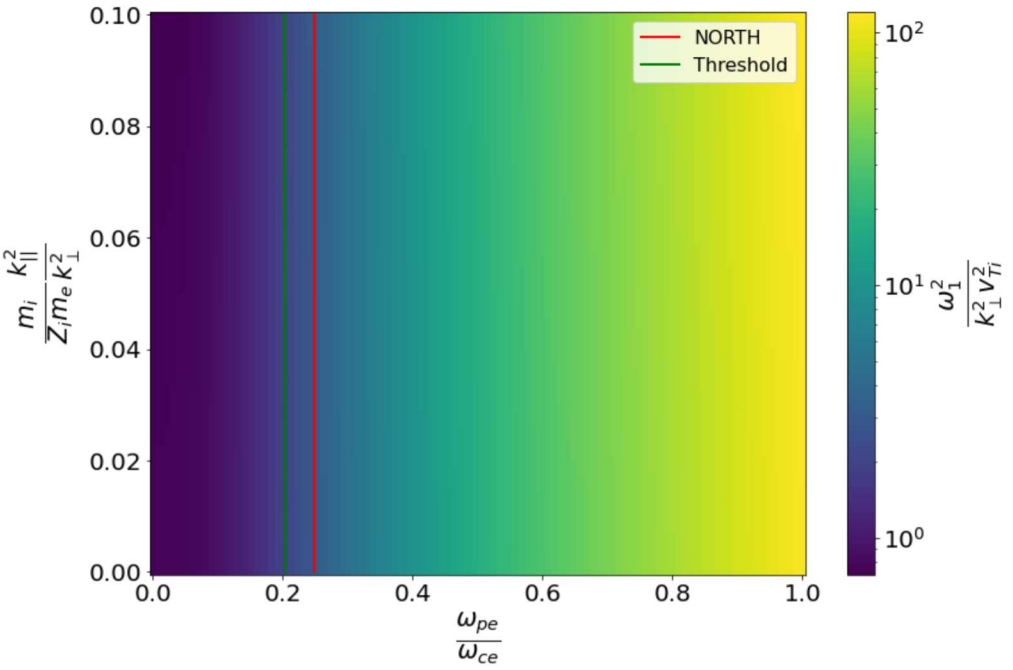

Figure 3.6: Value of $\frac{\omega_1}{kv_{Ti}}$ for the relevant values of its dependencies. If $\frac{\omega_1}{kv_{Ti}} > 2$ the expansion of $Z(\frac{\omega_1}{kv_{Ti}})$ in the model can be considered valid. The green line represents the threshold value $\frac{\omega_1}{kv_{Ti}} = 2$

To choose the appropriate analytical expression for the decay it is necessary to determine if the decay is resonant or not. To do this, following [13], it is enough to study the behaviour of the parameter $2\sqrt{\pi}\frac{\omega_1^3}{k_\perp^3 v_{Ti}^3}\exp\left(\frac{\omega_1^2}{k_\perp^2 v_{Ti}^2}\right)$ that is shown in Fig. 3.7.

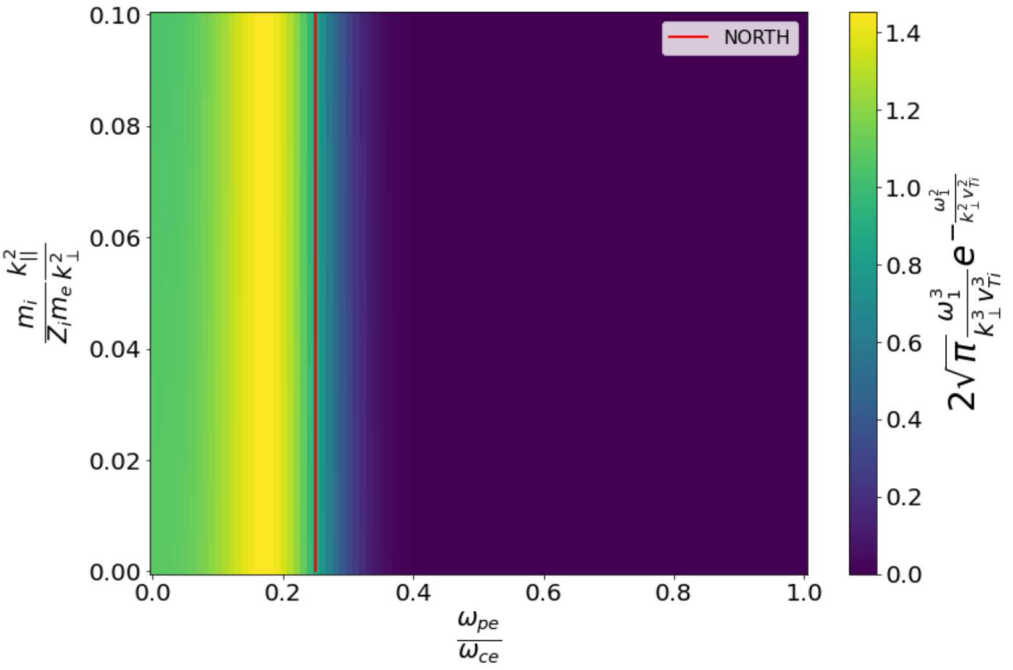

Figure 3.7: The parameter indicates the strength of the Landau damping of the low-frequency daughter wave.

This parameter basically determines the imaginary part of χ_i, as it is as clear from (2.77), and the Landau damping from (2.101). For the case of interest, the value is ≈ 0.55, making Landau damping of the low-frequency daughter wave relevant and so the decay non-resonant. In Fig. 3.8 the same parameter is computed along the upper hybrid layer, as done in Fig. 3.3 for b_e. It is clear that the

decay can be considered non-resonant only near the value of $Y \approx 0.95$ while for the rest of the CMA diagram the damping can be considered negligible and the decay resonant.

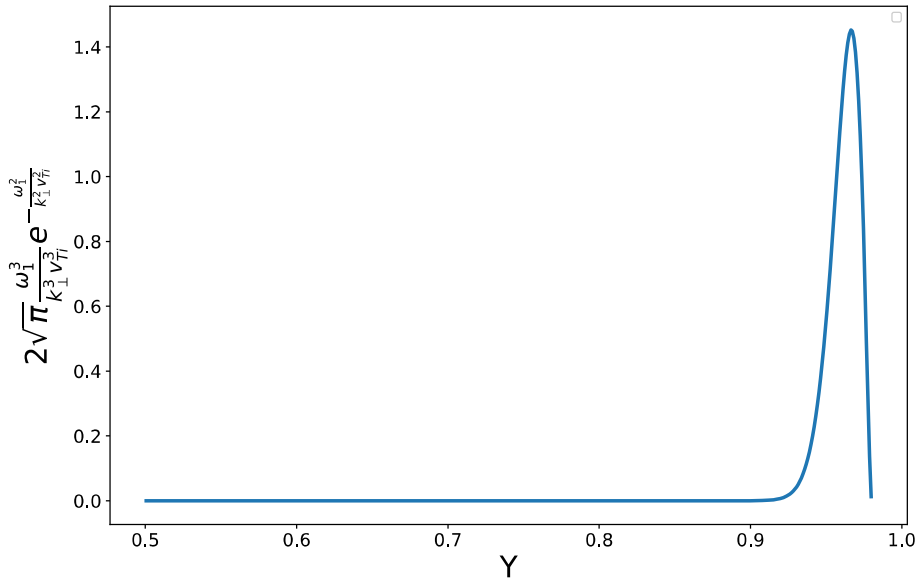

Figure 3.8: Landau damping factor along the UH layer parameterized by Y. Depending on where the trajectory of the beam meets the UH layer in the CMA diagram, the decay can be resonant or not depending on the strength of the damping factor. For the trajectory in Fig. 3.1 the UH layer is met at Y $\approx$ 0.95 and so the decay is non-resonant

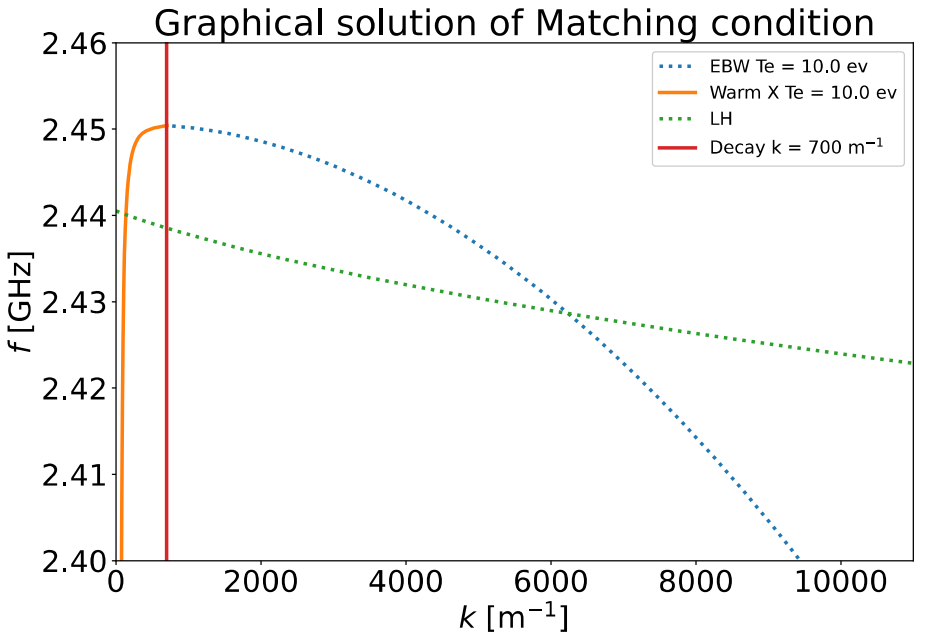

Figure 3.9: The dispersion relation of the X waves meets the EBW one at $k_0 \approx 700$ where the decay is supposed to happen. The green dotted line, denoted "LH" represents the frequency difference between the pump wave and one given by the dispersion relation of the LH daughter waves $f_0 - f_1$. The difference of frequencies is equal to the EBW frequency for $k \approx 6000$, making the dipole approximation reasonable.

The last approximation to verify is the validity of the dipole approximation $k_0 \approx 0$. To do this in Fig. 3.9 the dispersion relation for the pump warm X wave transforming into an electron Berstein

wave is plotted as a dispersion relation $f_2(k_2)$ along with the lower hybrid daughter as a dispersion relation $f_0 - f_1(k_1)$.

The two lines will meet where the matching conditions in the dipole approximation are met. To the pump wave at $f_0 = 2.45$ GHz corresponds the value $k_0 \approx 700$ m^{-1} which is less than a tenth of the value of $|k_1| = |k_2|$, making the dipole approximation very reasonable.

As previously mentioned, however, the decay does not in general happen at the resonance but when coming closer to it as long as the threshold is met and the matching conditions are satisfied. This can actually lead to the strongest frequency measured in the experiment being the one for which these conditions are first met instead of the decay frequencies at the resonance. This was indeed the case in the measurements performed in ASDEX [13]. To highlight this point in Fig.3.10 the matching condition without the dipole approximation for both the down-shifted high-frequency wave $f_2 = f_0 - f_1$ and the up-shifted high-frequency daughter $f_3 = f_2 + f_1$ are shown along the beam axis.

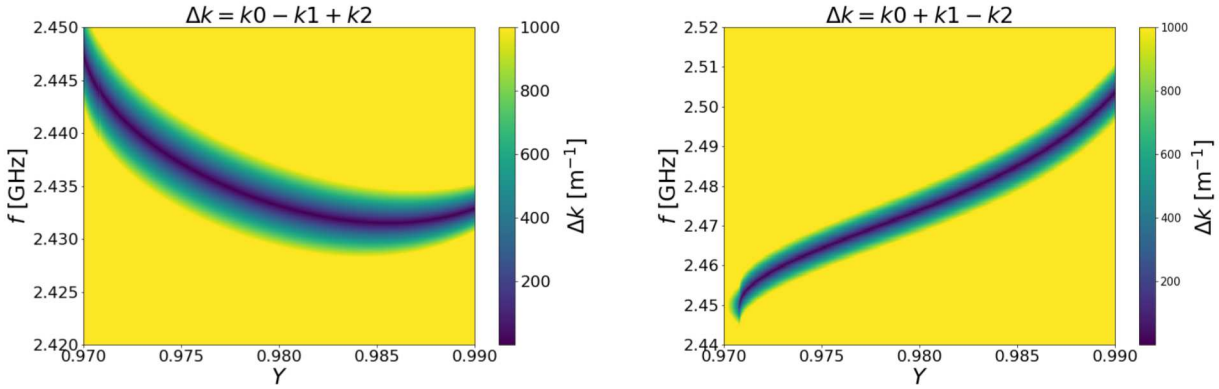

Figure 3.10: Graphical solution of the k matching conditions along the beam for the down-shifted and up-shifted high-frequency daughter waves. The values are capped at 10^3 to aid visualization

The areas where the Δk, representing the mismatch from the condition, tends to zero could all lead to the decay if the threshold is met and so the range of frequencies separating the electron Bernstein daughter from the pump wave can be of a few tens of MHz.

After having checked the related approximations in the model, it is now possible to use (2.109) and (2.121) to determine the electric field threshold for the homogeneous and inhomogeneous cases respectively. The thresholds along the beam path when nearing the upper hybrid layer are shown in Fig. 3.11.

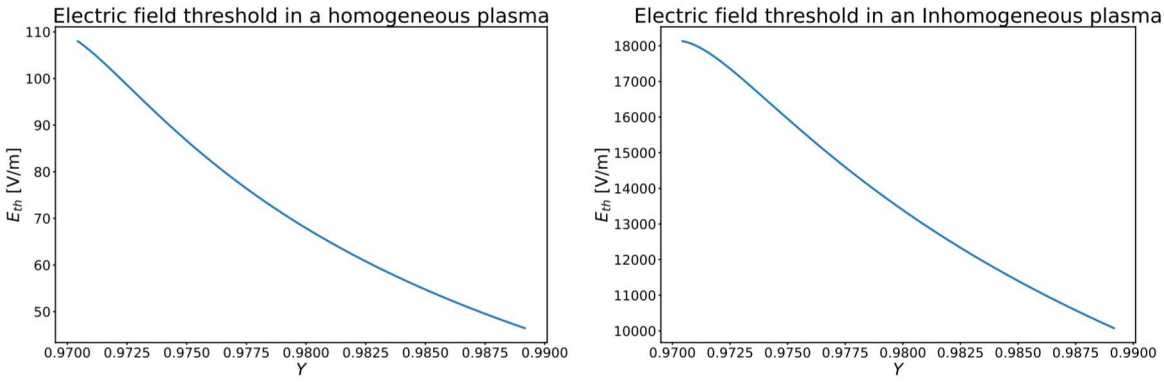

Figure 3.11: Electric field threshold for the parametric decay along the beam trajectory in a homogeneous plasma (left) and an inhomogeneous plasma (right)

Finally, by applying (2.126), the power threshold in an homogeneous and inhomogeneous plasma can be obtained and it is plotted in Fig. 3.12 using a half-width for the beam of 5 cm.

As expected the power threshold drops significantly when nearing the resonance in both cases. The power thresholds for the homogeneous case is about a factor of 10^4 larger making the decay

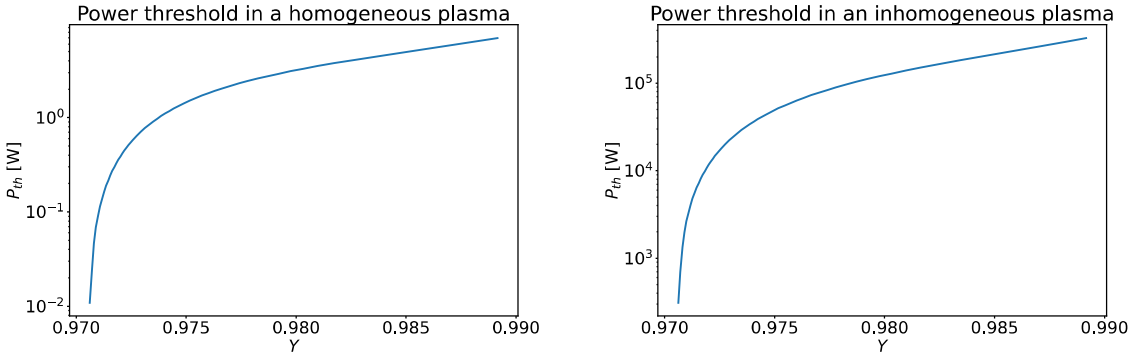

Figure 3.12: Power threshold for the parametric decay along the beam in a homogeneous plasma (left) and an inhomogeneous plasma (right)

in the inhomogeneous case much more difficult to achieve. In practice the value of threshold in the homogeneous case is very low, just a few tens of mW, that compared to the NORTH heating power of the order of the kW would lead to the decay happening anywhere the matching conditions are satisfied. The power threshold in the inhomogeneous case seems much more reasonable, becoming lower than a few kW only near the upper hybrid layer and reaching a minimum of $\approx$ 300 W at the resonance. The difference between the two cases is very large and it is natural to question if by changing density profile in NORTH it is actually possible to explore this large range of parameters. To this end in the next section, a scan over the density profiles will be discussed, keeping into account that the magnetic profile is instead fixed.

3.2 Density Profile Influence Over the Power Threshold

The simplest parameter scan is over the beam half-width at the upper hybrid layer. In the previous example, the value $W_{UH} = 5$ cm was assumed while in Fig. 3.13 a scan of the power threshold at the resonance in both the homogeneous and inhomogeneous cases is shown.

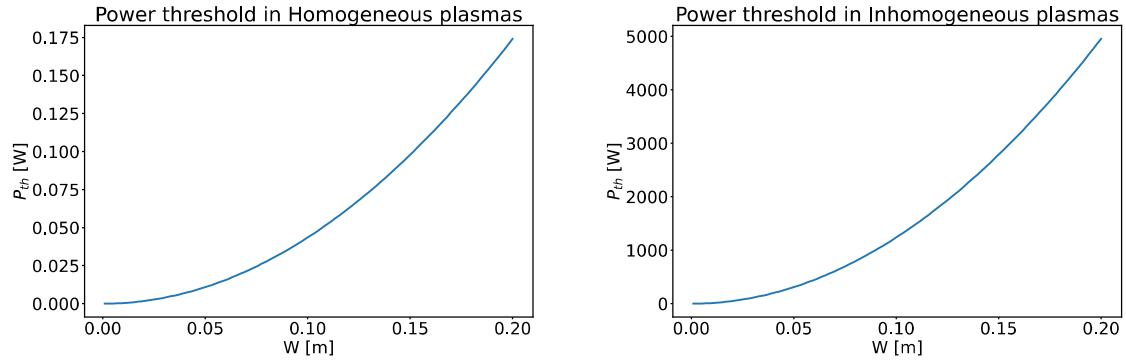

Figure 3.13: Power threshold scan over the half-width of the beam in a homogeneous plasma (left) and an inhomogeneous plasma (right)

The quadratic dependence on W_{UH} from (2.126) leads to a dependence that is overall weak when compared to the exponential scaling near the resonance. This allows obtaining a good estimate for the power threshold without requiring sophisticated codes to determine the propagation of the shape inside the plasma when traveling towards the upper hybrid layer, simplifying significantly the problem. The scan of the density profile can be performed in terms of the two parameters n_0 and σ that characterize it

$$n(x) = n_0 e^{-\frac{(x-R)^2}{2\sigma^2}} \tag{3.1}$$

where R is the major radius of the torus, equal to 0.25 m in the case of NORTH. Keeping one of the parameters as in the case study ($n_0 = 0.7 \cdot 10^{16}\text{m}^{-3}, \sigma = 0.03$ m) and scanning over a reasonable range the other one, in Fig.3.14 the position where the beam meets the resonance is shown.

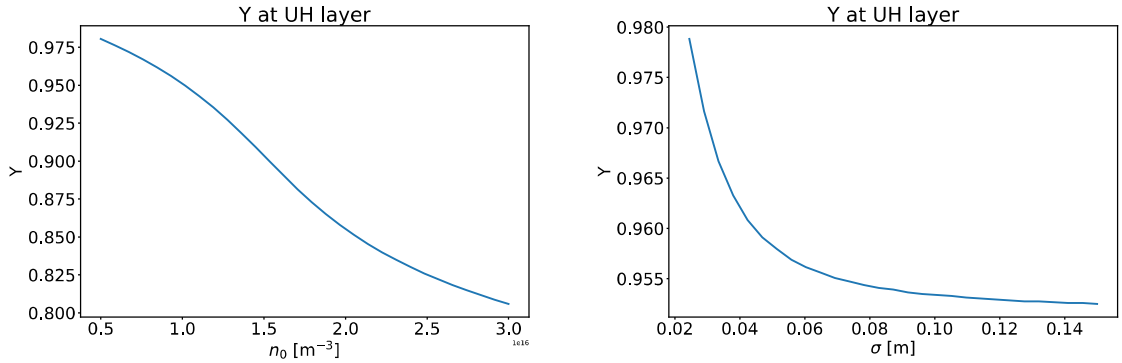

Figure 3.14: Position of the resonance along the beam path when scanning over the density profile parameters with the magnetic profile in Fig. 3.1, $T_e = 10$ eV and $T_i = 1$ eV.

As it could be expected, when σ becomes large with respect to the dimension of the system the density profile becomes approximately flat and the corresponding Y value of the UH layer saturates. In Fig. 3.15 the power thresholds and the frequency of the LH daughter waves during the n_0 scan are shown.

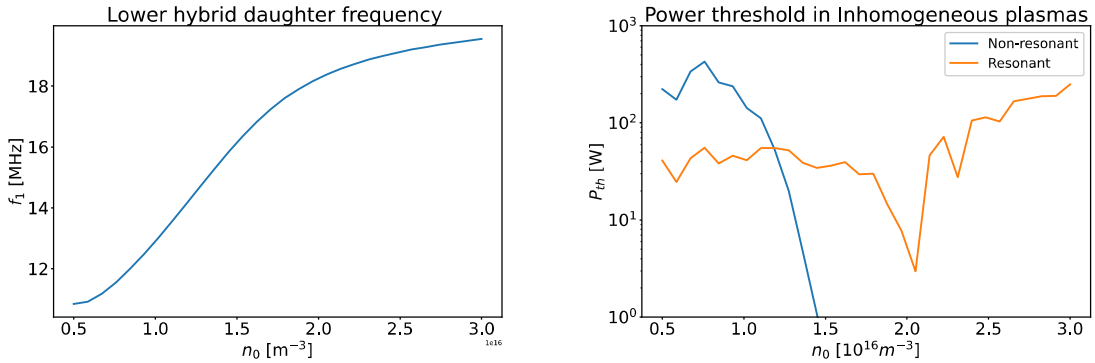

Figure 3.15: LH frequency (left) and power threshold (right) scan over the maximum density parameter while keeping the magnetic profile fixed, $T_e = 10$ eV and $T_i = 1$ eV. Both the resonant and non-resonant expressions are plotted but only one is valid at each point. The rapid decrease of the non-resonant threshold at higher density is due to its lack of validity in that region.

The frequency of the daughter waves shows a minimum in the region $n_0 = 0.75 \cdot 10^{16}$ m^{-3} and in general frequencies in the range of 13-20 MHz that increase with the density. The behaviour of the threshold for the value $n_0 = 2.0 \cdot 10^{16}$ m^{-3} is due to the intersection of the beam path with the upper hybrid layer happening near the maximum of the density profile which decreases the density gradient and so also the power threshold. Increasing n_0 further leads to shifting the resonance towards a point with lower density and so to an increase in the power threshold. The threshold in the homogeneous case varies significantly in the range considered but in practice it remains always very small and it is easily reached in experiments, reaching a maximum of ≈ 10 W which is too low to be measured by the heating system in NORTH. In the inhomogeneous case, the decays start as non-resonant with a threshold of a few 100's W, then it switches to a resonant decay and the threshold appears about constant until $n_0 \approx 2.0 \cdot 10^{16}$ with values of the order of some 10's of W and after this critical value there is a rapid increase in the threshold. While both the resonant and non-resonant curves have been plotted to highlight their difference, only one of the two values can have physical meaning. The area preceding the critical value at $n_0 \approx 2.0 \cdot 10^{16}$ features a fast drop in the non-resonant threshold and it is due to the Landau damping term tending to zero while it is assumed to be dominant in

the determination of the non-resonant expression. Taking from Fig. 3.8 the Landau damping, and so the non-resonant expression, to be relevant until $Y \approx 0.93$ and comparing this with Fig.3.14, an approximate division between the two regimes is

$$\text{Non - Resonant Expression} \qquad n_0 < 1.4 \cdot 10^{16} \text{m}^{-3} \tag{3.2}$$

$$\text{Resonant Expression} \qquad n_0 > 1.4 \cdot 10^{16} \text{m}^{-3} \tag{3.3}$$

In Fig.3.16, instead, the scan over the σ parameter is shown.

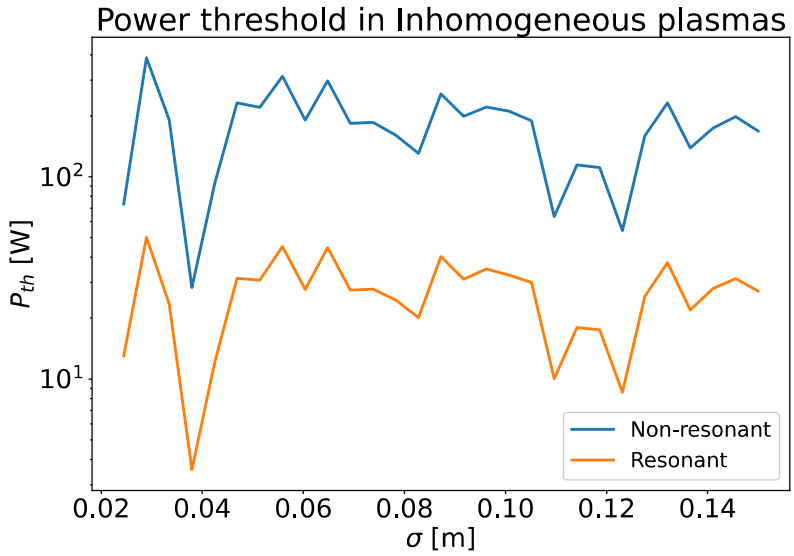

Figure 3.16: Power threshold scan over the σ parameter while keeping the magnetic profile fixed, $T_e = 10$ eV and $T_i = 1$ eV. In this case, the decay is always non-resonant.

The resonant and non-resonant lines are completely disjointed but when comparing the $Y \approx 0.93$ limit with Fig.3.14 it is clear that in this case the decay is always non-resonant and so of the order of ≈ 100 W. It could be expected that increasing σ would lead to a convergence with the homogeneous case, as the density profile becomes more and more flat but this does not appear to be the case when looking at Fig. 3.16. The reason lies in the fact that the expression for the power threshold in the inhomogeneous case is composed of two terms, one related to the variation of the density profile and one related to the magnetic field profile.

$$N_{IN} = \left(\frac{A_2 \omega_{ce}^2}{A_1 \omega_{UH}^2} + 1 \right) \frac{r_{Le}}{2L_N} \qquad B_{IN} = \left(\frac{A_2 \omega_{pe}^2}{A_1 \omega_{UH}^2} + \frac{\omega_{ce}^2}{\omega_{pe}^2} \right) \frac{r_{Le}}{L_B} \tag{3.4}$$

In Fig. 3.17 the ratio of the density term over the field term is shown and it is clear that when moving to flatter profiles the field term becomes relevant, keeping the final threshold value on the order of 100 W.

3.3 Temperature and Elemental Dependence

Moving on to study the effects of the remaining parameters of the system, in this section the effect of T_e and T_i, as well as the choice of the operating gas, on f_1 and P_{th} will be explored.
In the previous example, a value for the ion temperature of $T_i \approx 1$ eV has been assumed. While this assumption is reasonable, at the time of this work there is no diagnostic operating on NORTH to measure this quantity and such a measurement is complicated by the low temperatures involved. It then becomes important to make sure that variations in T_i do not significantly affect the model

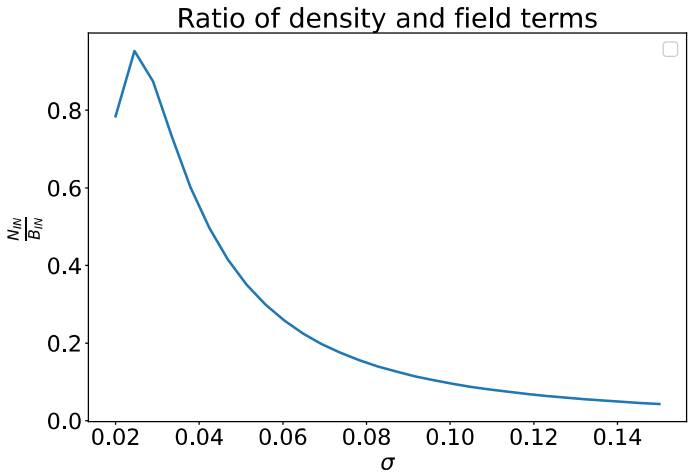

Figure 3.17: Ratio of the density and field term in the power threshold expression for an inhomogeneous plasma

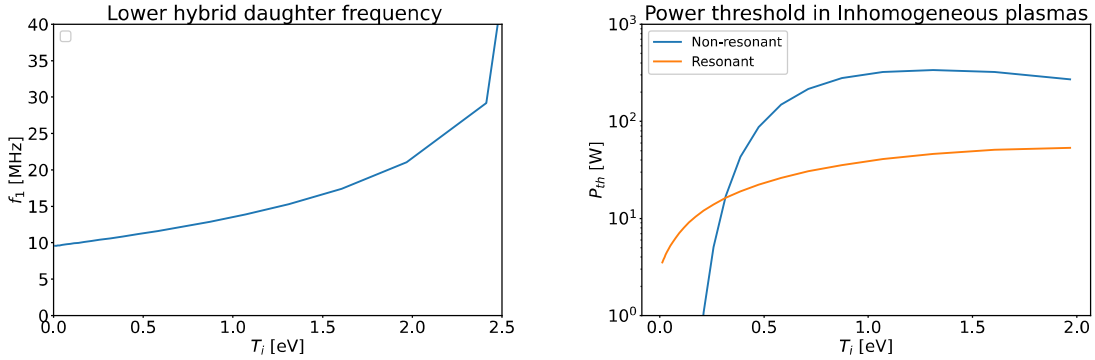

Figure 3.18: Power threshold and LH daughter frequency scan over T_i while keeping all the other parameters as in the case study.

estimates. In Fig. 3.18 a scan of the inhomogeneous power threshold and the LH daughter frequency over T_i is shown.

Considering that a lower value of T_i than the assumed 1 eV is more likely than a higher value, it is clear that the dependence of f_1 on T_i is weak and only variations of a few MHz are expected even when going down to low temperatures, making the lack of a precise measurement of this quantity a secondary concern for this first analysis.
Note that the upper hybrid frequency does not depend on either T_e or T_i but the Landau damping term is dependent on the temperature and so it is not correct to use

$$Y \approx 0.93$$

as a boundary between the resonant and non-resonant regime. It appears that the power threshold has a strong dependence on T_i but as a lower T_i than expected is much more likely than a higher one and the threshold decreases with lower temperatures, the parametric decay should still be measurable. Moving on to the effect of T_e, shown in Fig. 3.19, only a small effect on the LH daughter frequency is present. Furthermore, T_e can be measured directly during the experiments, making it much easier to account for than T_i.

The power threshold is near a maximum at 10 eV and so it can only become smaller when varying the temperature. It is worth mentioning that the temperature scans have been performed by keeping one of the temperature constant but quite often the dependencies of the model are on $\frac{T_e}{T_i}$, making the two scans strongly related. For example, the drop for $T_i \approx 0.5$ eV is likely to be related to the one at $T_e \approx 20$ eV.

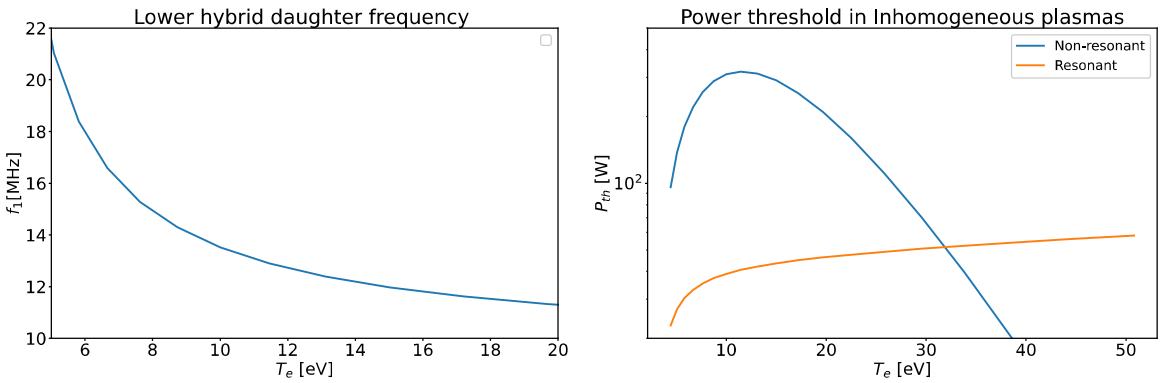

Figure 3.19: Power threshold and LH daughter frequency scan over T_e while keeping all the other parameters as in the case study.

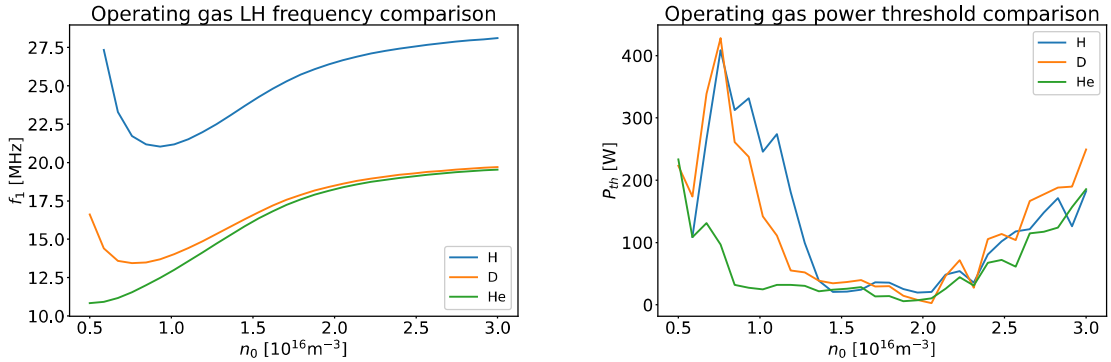

Figure 3.20: Power threshold and LH daughter frequency using H,D and He as operating gas. Choosing H as gas leads to higher LH frequencies and so to an effect that is easier to measure.

Finally, a similar scan over the peak Gaussian density has been performed over the three working gases currently operable on NORTH: H, D and He. In Fig. 3.20 the values of the frequencies f_1 and inhomogeneous power thresholds P_{th} for the three are compared. To simplify the visualization only the maximum between the resonant and non-resonant power threshold has been plotted at each point. The power threshold does not appear significantly affected when switching between D and H but a significant reduction can be seen when using He in the density region near the case study. The effect should then be observable with all the gases. A more interesting effect is instead present in the frequency of the LH daughter wave. f_1 scales with $\frac{m_i}{Z}$ and to lower masses corresponds a daughter more distant from the pump wave and so more easily measured. This makes H the most suited gas to detect the parametric decay but even then a shift of ≈ 25 MHz on a pump wave of 2.45 GHz will still prove a complex measurement.

Chapter 4

PIC simulations of PDI in NORTH

To validate the predictions of the analytical model some Particle In Cell (PIC) simulations have been performed using the EPOCH code for NORTH relevant scenarios. EPOCH has already been successfully used to perform PDI studies on ASDEX [14], which are taken of sufficient proof of the trustworthiness of the code. After a brief description of the EPOCH code in section 4.1, a description of the characteristics of the simulations is presented in section 4.2. The results of the simulations are reported for different scenarios in section 4.3.

4.1 The EPOCH Code

A plasma is a quasi-neutral system composed of a large[1] number of charged particles [7]. Ideally, the behaviour of such a system could be simulated by starting from an initial distribution of positions and velocities for the entire set of particles and then follow their evolution in time through the coupling of Newton's laws of mechanics and Maxwell's equations. In practice this is not feasible due to the very large number of particles involved, which would require analogously large computational resources. PIC codes are a commonly used tool in plasma physics that groups together many particles of a single species into "super-particles" that represent a cloud of particles moving together and that behaves like a single particle. The higher the number of super-particles, the more the simulation will resemble the original system but also the higher the computational requirements. EPOCH [27] is a code developed by the University of Warwick to perform these kinds of simulations. It has the ability to simulate systems with different species, electromagnetic waves and background fields. Additional features such as collisions, ionization and QED effects can also be included in the simulation. The time evolution of the system is performed by the coupling of a solver for the particles' positions that also computes the currents generated by the particles and a field solver to compute the fields on a spatial grid. The electric and magnetic fields are computed on a staggered grid, called the Yee grid, as shown in Fig. 4.1 in a 2D projection.

The derivatives are computed using the finite-difference time-domain method (FDTF), that for example for E_y is given by

$$\frac{\partial E_y}{\partial x}\Big|_{(i,j,k)} \approx \frac{E_{y_{i+1,j,k}} - E_{y_{i,j,k}}}{\Delta x} \tag{4.1}$$

where Δx is the grid discretization and (i, j, k) the site on the grid where the derivative is computed $E_{y,ijk} = E_y(i\Delta x, j\Delta y, k\Delta z)$. The full derivation of the equations for updating the system can be found in [18] but the final equations are reported next. The fields are updated from time n to time $n + \frac{1}{2}$ using

[1] The number of particles in a sphere of radius $\lambda_D = \sqrt{\frac{\epsilon_0 k T_e}{n e^2}}$ must be much greater than 1 in order for the plasma to exhibit collective behaviour

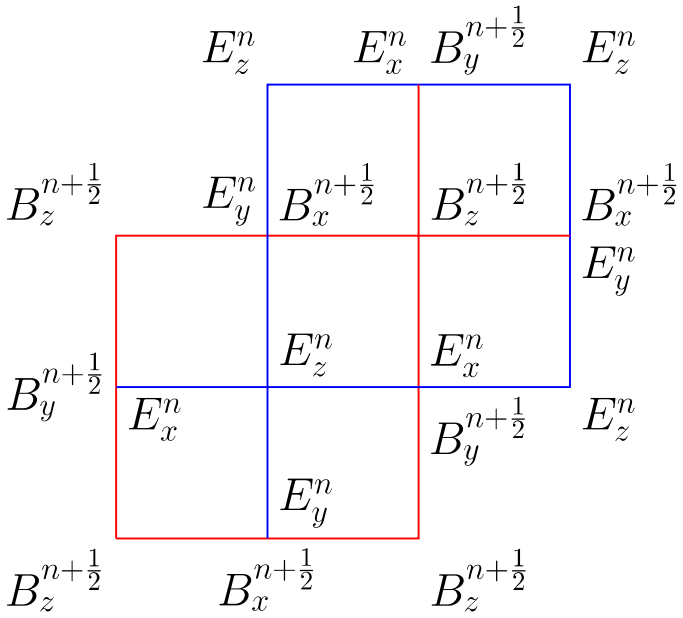

Figure 4.1: 2D projection of the Yee grid. In blue the grid related to the electric field while in red the one related to the magnetic field. The index n refers to the time step. The grids are shifted by half a step $n + \frac{1}{2}$ in time while also being staggered in space.

$$\mathbf{E}^{n+\frac{1}{2}} = \mathbf{E}^n + \frac{\Delta t}{2}\left(c^2\boldsymbol{\nabla}\times\mathbf{B}^n - \frac{\mathbf{J}^n}{\epsilon_0}\right) \tag{4.2}$$

$$\mathbf{B}^{n+\frac{1}{2}} = \mathbf{B}^n - \frac{\Delta t}{2}\left(\boldsymbol{\nabla}\times\mathbf{E}^{n+\frac{1}{2}}\right) \tag{4.3}$$

Then the particles are moved according to the discretized Vlasov equation

$$\mathbf{p}_\alpha^{n+1} = \mathbf{p}_\alpha^n + q_\alpha\Delta t\left[\mathbf{E}^{n+\frac{1}{2}}\left(\mathbf{x}_\alpha^{n+\frac{1}{2}}\right) + \nu_\alpha^{n+\frac{1}{2}}\times\mathbf{B}^{n+\frac{1}{2}}\left(\mathbf{x}_\alpha^{n+\frac{1}{2}}\right)\right] \tag{4.4}$$

$$\mathbf{x}_\alpha^{n+1} = \mathbf{x}_\alpha^{n+\frac{1}{2}} + \frac{\Delta t}{2}\nu_\alpha^{n+1} \tag{4.5}$$

$$\mathbf{x}_\alpha^{n+\frac{3}{2}} = \mathbf{x}_\alpha^{n+1} + \frac{\Delta t}{2}\nu_\alpha^{n+1} \tag{4.6}$$

where $\mathbf{p}_\alpha, q_\alpha, \mathbf{x}_\alpha$ and ν_α are the particle momentum, charge, position and velocity respectively for a particle of species α and $p_\alpha = \gamma_\alpha m_\alpha \nu_\alpha$. The reason why the evolution from $n + \frac{1}{2}$ to $n + \frac{3}{2}$ is split into two steps (4.5 - 4.6) is to have the particle positions at time n and compute the currents required for the evolution of the field. Finally, the evolution of the field is completed via

$$\mathbf{B}^{n+1} = \mathbf{B}^{n+\frac{1}{2}} - \frac{\Delta t}{2}\left(\boldsymbol{\nabla}\times\mathbf{E}^{n+\frac{1}{2}}\right) \tag{4.7}$$

$$\mathbf{E}^{n+1} = \mathbf{E}^{n+\frac{1}{2}} + \frac{\Delta t}{2}\left(c^2\boldsymbol{\nabla}\times\mathbf{B}^{n+1} - \frac{\mathbf{J}^{n+1}}{\epsilon_0}\right) \tag{4.8}$$

Additional information on the code is in [27].

4.2 Simulations Setup

The code supports simulations of systems in 1D, 2D or 3D. To represent accurately non-linear effects such as parametric decay a large number of super-particles is required. This leads to large computational requirements and so the only possibility consistent with the duration and computational

resources of this work was to simulate the system in 1D. The injection of the X-waves into NORTH is performed radially and so is a problem well suited to be described by a 1D code. Unfortunately, however, Maxwell's equations are incompatible with an inhomogeneous magnetic field in 1D and so a homogeneous magnetic field had to be used. Recalling from the discussion on Fig. 3.17 that the magnetic field inhomogeneity is expected to dominate the power threshold and that the power thresholds for homogeneous plasmas are orders of magnitude lower than the corresponding values for inhomogeneous plasmas, 1D simulations are clearly unsuitable for determining the power thresholds of the process. The frequencies of the daughter waves are instead independent on the density and magnetic field gradients at the UH layer and so they are taken as the main metric to be compared with the analytical model. Using 2D simulations, an inhomogeneous field can be included in the system and the power threshold can be determined in more realistic conditions but given how the maximum heating power is significantly higher than the threshold estimates made in chapter 3, this has not been deemed a priority and is left as future work. The 1D simulation covers a length of 10 cm, corresponding to roughly 10 wavelengths of an X-wave and 100 wavelengths of an EBW and LH daughter waves at the UH layer. The grid is discretized in 1000 steps so as to have 10 points for each wavelength of the shorter waves. The system is composed of only two species: electrons and ions. This corresponds to neglecting the effects of impurities and considering a fully ionized plasma, as done in the analytical model. The electrons and ions are both initialized with a Gaussian distribution for the velocities, characterized by the assumptions of the case study $T_e = 10$ eV and $T_i = 1$ eV. The density is ramped linearly between two values, n_L and n_H, along the length of the grid and a constant magnetic field is present with a value chosen as to have the Upper Hybrid layer roughly in the center of the grid. A pump wave at 2.45 GHz is injected from the left side of the grid with a maximum amplitude I_{max} that is time modulated by a factor

$$A_{pump} = \frac{2}{\pi} \arctan\left(\frac{t}{t^\star}\right) \tag{4.9}$$

with $t^\star = 5$ ns, a time long enough to be correctly sampled but short enough with respect to the duration of the full simulation. EPOCH does not allow to have longitudinal waves as boundary conditions, so the X waves are polarized initially with the electric field perpendicular to both k and B and the field solver makes the wave longitudinal near the resonance, as is expected near the UH layer (Fig. 2.2). The boundary conditions for the EM waves are of the type *simple_laser* and *simple_outflow* on the left and right boundary respectively. Impinging EM waves are transmitted as much as possible and removed from the system. The boundary conditions for the particles are of the *thermal* type on both limits of the grid: when a particle impinges on the boundary it is removed from the system and is substituted with a particle with velocity taken from the initial Gaussian distribution used to initialize the system. This avoids an unbounded heating of the system given the lack of any other dissipation mechanism. The code saves the simulation data for the fields, the number densities of the species and their temperature with a frequency of $5f_0 = 12.25$ GHz, which marks the temporal resolution of the system. Using 5×10^5 super-particles and 48 cores on the DTU cluster the typical simulation times are of 6 hours.

4.3 NORTH PDI PIC Simulations

Once again it is possible to start from reasonable values, such as a wave with an intensity of 40 $\frac{W}{cm^2}$, corresponding to 1 kW over a surface of 25 cm^2, and 5 $\times 10^5$ super-particles and then study how the outcomes change when varying the characteristic values. For the density values of $n_L = 0.5 \times 10^{16} m^{-3}, n_H = 0.75 \times 10^{16} m^{-3}$, and a field of $|B| = 0.084$ T, the upper hybrid frequency is met for $n_{UH} = 0.58 \times 10^{16} m^{-3}$. The spectrogram of E_x, the electric field component along the direction of motion, is shown in Fig. 4.2

In this case, the pump wave at 2.45 GHz seems to fade with time while additional peaks can be noticed at high frequencies and gain strength with time, possibly due to decay effects. Their frequency difference is equal to the lower hybrid daughter frequency. In the analytical model the

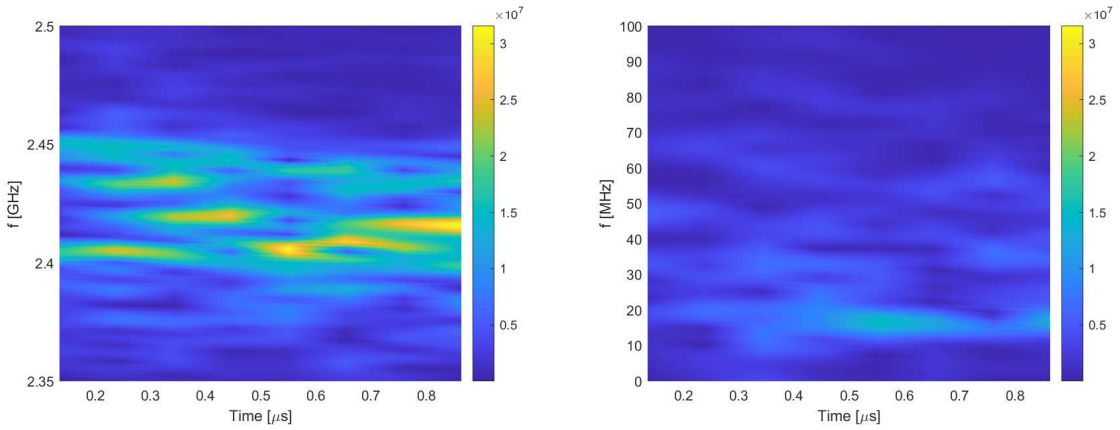

Figure 4.2: E_x spectrogram at the UH resonance. Focus on the high-frequency region (left) and low-frequency region(right). Simulation with $n_L = 0.5\times10^{16}\mathrm{m}^{-3}, n_H = 0.75\times10^{16}\mathrm{m}^{-3},$, $|B| = 0.084$ T, 5×10^5 super-particles and 1kW X wave at 2.45 GHz

discussion has always focused on the presence of one daughter wave per type, but recalling that due to the homogeneity of the field, the 1 kW case is much over the PDI threshold, the possibility of creating additional waves at multiples of the LH frequency also becomes relevant. This multitude of peaks is not expected during the actual experiments as the heating power is much closer to the threshold. It can also be noticed how these types of parametric effects can drain the power of the pump wave significantly but the fraction of converted power cannot be determined easily as part of the X-wave is absorbed at the UH resonance. In Fig. 4.3 the time average of the spectrogram is shown and the different peaks are clearly distinguishable.

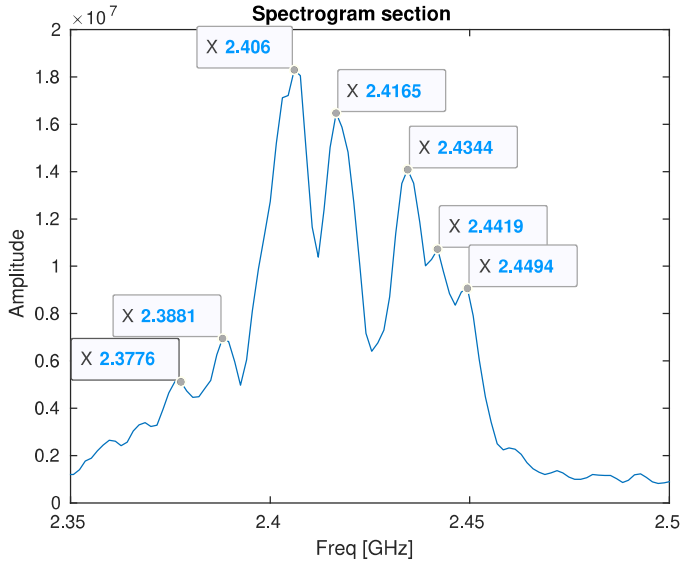

Figure 4.3: Time average of E_x spectrogram in Fig. 4.2 at the UH resonance for the entire duration of the simulation

In particular, the peaks at 2.434 and 2.416 GHz can be attributed to the parametric decay of the 2.45 GHz pump, as they are consistent with the LH daughter frequency shown in Fig. 4.2 of ≈ 17 MHz. Some peaks with a frequency difference of ≈ 8 MHz from the other ones can also be noticed, for example at 2.442 and 2.406 GHz. The origin of these peaks is not known with certainty but it is possible they are due to the parametric decay of the pump wave into a pair of an EBW and an Ion Bernstein Wave (IBW). IBWs are physically similar to EBWs but due to the oscillation of ions instead of electrons and so with much lower frequencies. Many different branches of IBWs exist and the excitation of one of these low-frequency branches could explain the additional peaks. Such an explaination was also proposed for additional peaks seen on PDI experiments in ASDEX [28]. The

frequency differences of the PDI peaks are not exact multiples of each other, but this could be due to the fact that they are obtained through a time average of a system with a time-varying temperature, which affects the frequency of the LH waves even if only slightly or to different branches being dominant in subsequent decays. This can be seen by looking at the T_e and T_i plots in Fig. 4.4

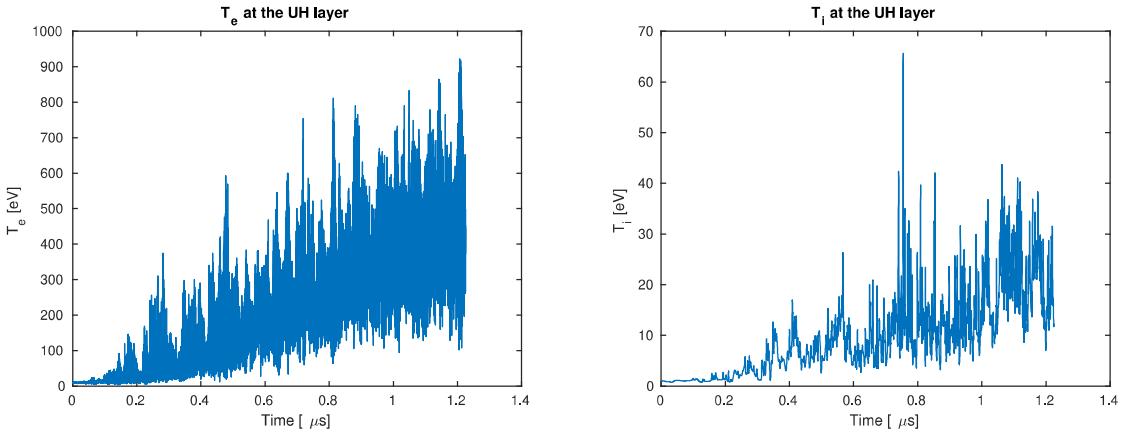

Figure 4.4: Temperature spectra during the simulation. The strong increase in temperature is due to the presence of a homogeneous magnetic field.

Of course, such an increase in temperature is not realistic and is an artifact of having a constant magnetic field, but this does not invalidate the results on the parametric decay as the daughter frequencies are only weakly dependent on the temperature ratio. Increasing the density of the system leads to more defined and well-separated peaks, as the frequency of the LH daughter wave is increased. Considering for example a case with $n_L = 3.5 \times 10^{16}\mathrm{m}^{-3}, n_H = 5 \times 10^{16}\mathrm{m}^{-3}$ and $|B| = 0.06$ T shown in Fig. 4.5

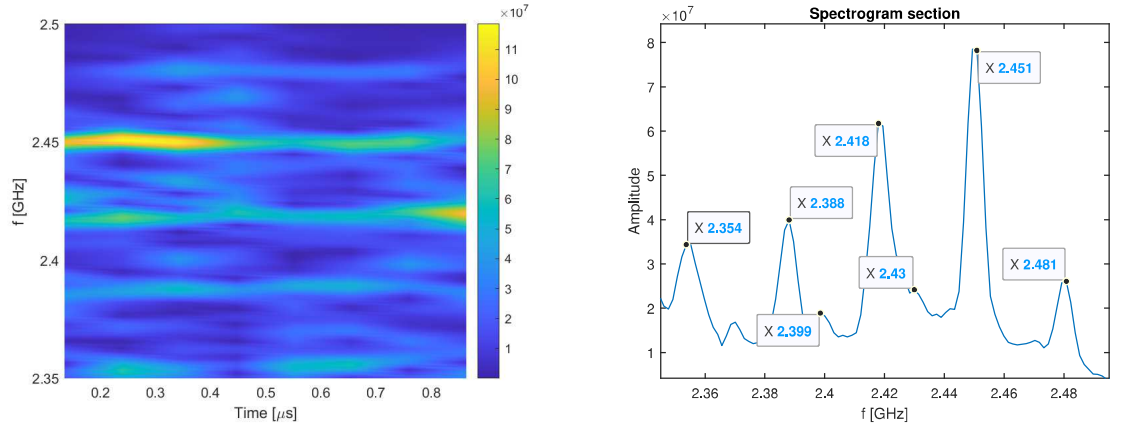

Figure 4.5: E_x spectrogram at the UH resonance (left) and time-integrated spectrum over the full simulation time (right). Simulation with $n_L = 3.5 \times 10^{16}\mathrm{m}^{-3}, n_H = 5 \times 10^{16}\mathrm{m}^{-3},$, $|B| = 0.06$ T, 5×10^5 super-particles and 1kW X wave at 2.45 GHz. The daughter EBW's from successive decays are visible

The frequency of the LH daughter wave is significantly higher than in the low-density case and it is much closer to the estimate obtained using the analytical model, with a value of ≈ 30 MHz. The peaks with frequency differences from the pump wave equal to multiples of the LH frequency are much more visible and the up-shifted high-frequency wave has become visible, unlike in the low-density case. The additional peaks shifted by 8 MHz are not clearly visible but some small peaks shifted by ≈ 20 MHz from the pump wave and the EBW coming from the first decay are present instead. To check if these additional peaks are related to the process of interest, a simulation at the "wrong" magnetic field was performed. In this way, the upper hybrid layer is not present in the simulation and no decay processes are expected. The resulting spectrogram is shown in Fig. 4.6. As expected the spectrograms are free from significant additional peaks, indicating that all the peaks are related to the amplification of the electric field at the UH layer. It could be argued that it is an artifact of the simulation due to the

low number of super-particles, but even a simulation performed with the same parameters as Fig. 4.5 but with $5 \cdot 10^6$ super-particles, shown in Fig. 4.7, still presented these peaks as well as peaks at ≈ 10 MHz. This might suggest that at higher density the possible IBW waves are present at the higher frequency of 10 MHz and its multiples but the results are not conclusive and not the main topic of this work, so their exploration is left to future work.

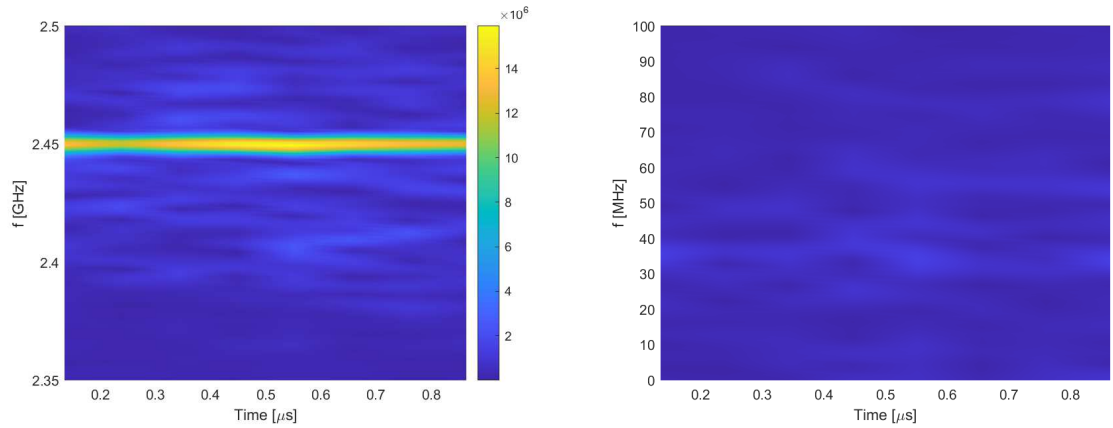

Figure 4.6: E_x spectrogram in a plasma with no UH resonance. Focus on the high-frequency region (left) and low-frequency region(right). Simulation with $n_L = 3.5 \times 10^{16}\mathrm{m}^{-3}, n_H = 5 \times 10^{16}\mathrm{m}^{-3},$, $|B| = 0.084$ T, 50×10^3 super-particles and 1kW X wave at 2.45 GHz. As expected no PDI is visible.

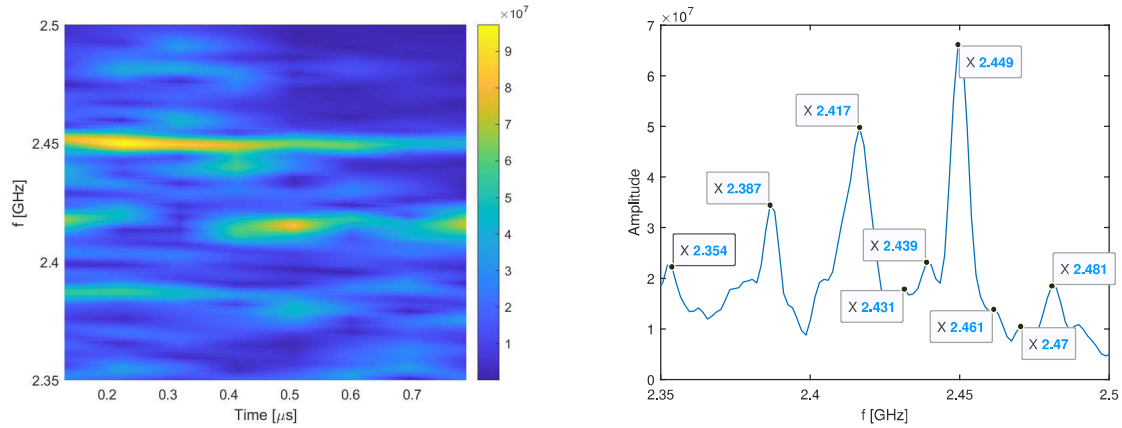

Figure 4.7: E_x spectrogram at the UH resonance (left) and time-integrated spectrum over the full simulation time (right). Simulation with $n_L = 3.5 \times 10^{16}\mathrm{m}^{-3}, n_H = 5 \times 10^{16}\mathrm{m}^{-3},$, $|B| = 0.06$ T, 5×10^5 super-particles and 1kW X wave at 2.45 GHz. The additional peaks are present even with a higher number of super-particles.

The frequencies of the lower hybrid daughter waves are also the same as in the case with fewer super-particles, justifying the use of the lower number in the following studies. It is also important to note that these frequencies also appear in the spectrogram of the electron density, shown in Fig. 4.8 and not only of the electric field.

No corresponding oscillation at the frequency difference between the additional peaks and the pump wave (≈ 10 MHz) can be found in either the electron or ion densities, while instead the frequency of the LH daughter wave and its harmonic can be clearly seen in Fig. 4.9.

The presence of the density oscillations at low frequencies suggests that it should be possible to measure the low-frequency waves as density oscillations on a Langmuir probe.
It is now interesting to study the variation of the response of the system with the power of the injected wave.

Considering a shot with 3 kW of power and the same parameters as the low-density case in Fig. 4.2, shown in Fig. 4.10, a higher number of peaks can be seen. Once again the system is composed by peaks shifted of $\approx$ 13MHz from the pump wave, which can be attributed to parametric decay, and a peak at a frequency ≈ 10 MHz smaller than the pump wave that in this case is actually the

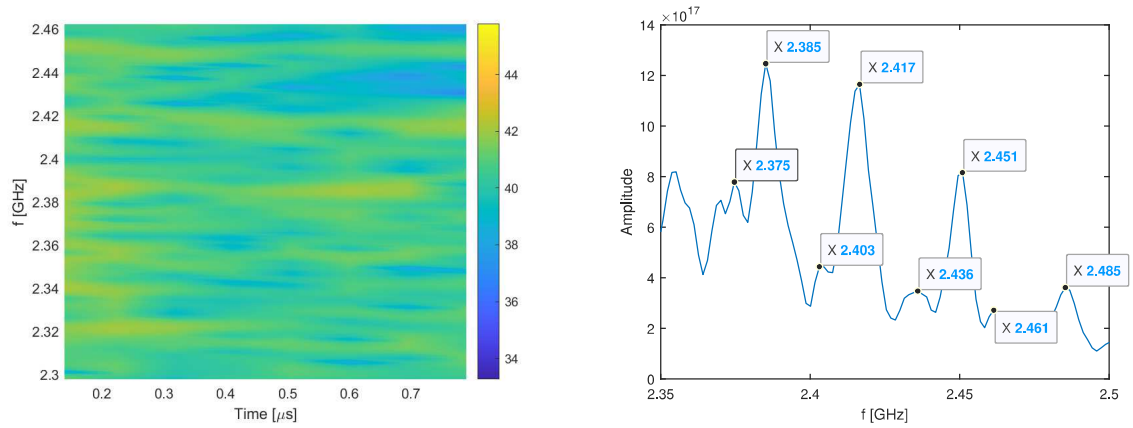

Figure 4.8: n_e spectrogram at the UH resonance (left) and time-integrated spectrum over the full simulation time (right). Simulation with $n_L = 3.5 \times 10^{16}\mathrm{m}^{-3}, n_H = 5 \times 10^{16}\mathrm{m}^{-3},$, $|B| = 0.06$ T, 5×10^5 super-particles and 1kW X wave at 2.45 GHz

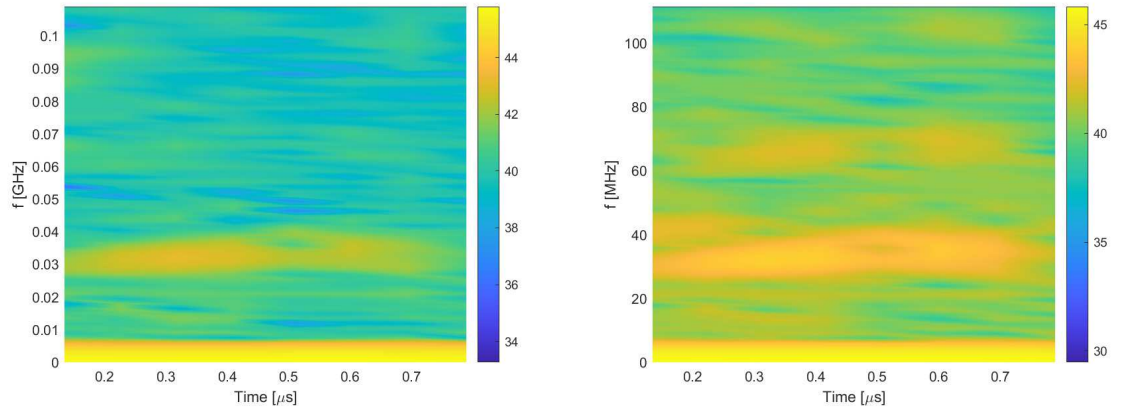

Figure 4.9: n_e (left) and n_i (right) low-frequency spectrograms at the UH resonance. Simulation with $n_L = 3.5 \times 10^{16}\mathrm{m}^{-3}, n_H = 5 \times 10^{16}\mathrm{m}^{-3},$, $|B| = 0.06$ T, 5×10^5 super-particles and 1 kW X wave at 2.45 GHz

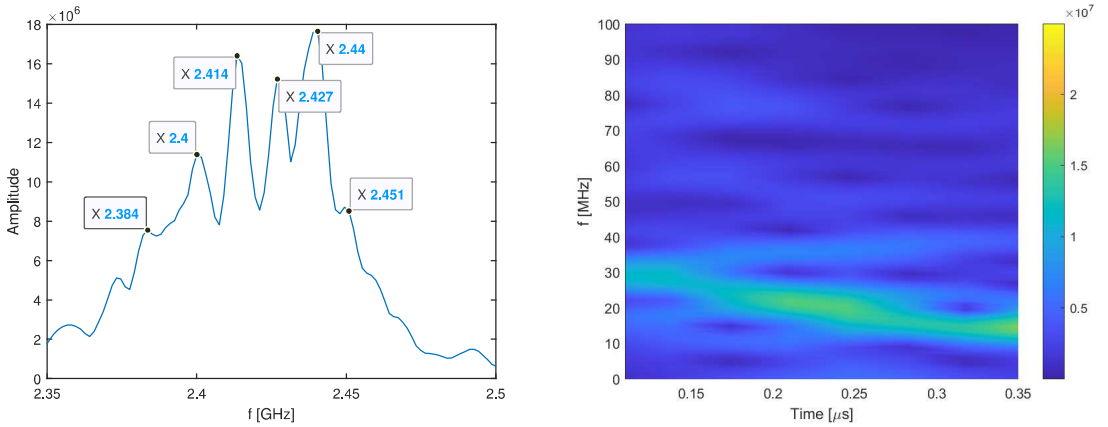

Figure 4.10: E_x spectrogram at the UH resonance. Time-integrated spectrogram of the high-frequency region (left) and low-frequency region(right). Simulation with $n_L = 0.5 \times 10^{16}\mathrm{m}^{-3}, n_H = 0.75 \times 10^{16}\mathrm{m}^{-3},$, $|B| = 0.084$ T, 5×10^5 super-particles and 3 kW X wave at 2.45 GHz. Additional peaks can be seen using more power.

strongest signal. From the low-frequency spectrogram, it is evident in this case how with increasing temperatures the LH daughter wave frequency is shifted from the expected value of $\approx$ 30MHz to $\approx$ 10MHz. As in NORTH these higher temperatures are not reached, some additional simulations have been performed at lower powers until the typical temperatures of the system remained consistent with expectations. A simulation with a beam power of 10 mW is shown in Fig. 4.11.

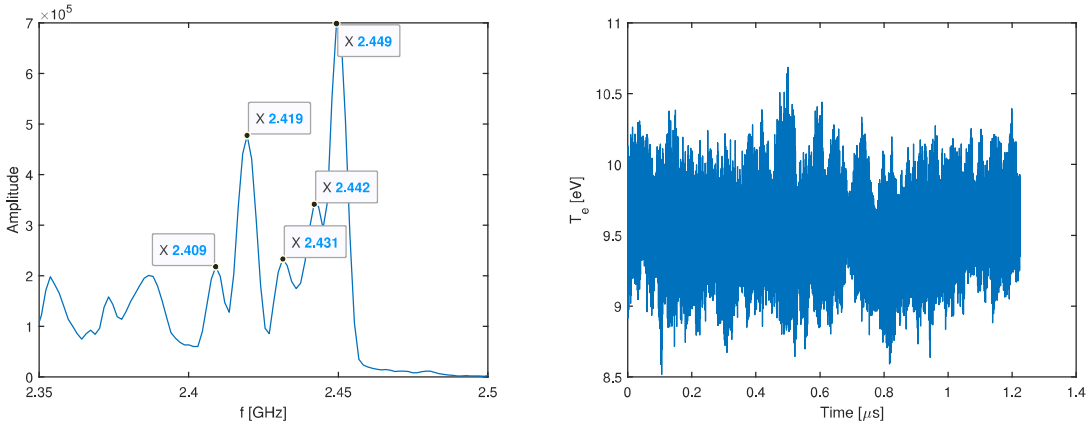

Figure 4.11: Time integrated E_x spectrogram of the high-frequency region (left) and T_e (right) at the UH resonance. Simulation with $n_L = 3.5 \times 10^{16}\mathrm{m}^{-3}, n_H = 5 \times 10^{16}\mathrm{m}^{-3}$,, $|B| = 0.006$ T, 5×10^5 super-particles and 10 mW X wave at 2.45 GHz. The increased absorption caused by the constant magnetic field is offset by the lower heating power as to reach a system consistent with the expected temperature

In this case, it can be seen that the temperature stays around 10 eV for the duration of the simulation while simulations at 100 mW showed a visible temperature increase. From this simulation, a frequency of $\approx$ 30 MHz for the LH daughter wave is confirmed and it is in line with predictions. Furthermore, using a more appropriate intensity for the case with a constant magnetic field, it can be seen how the first high-frequency daughter wave can be clearly distinguished from the background and has a height comparable with the pump wave while subsequent peaks at multiples of the 30 MHz frequency become much less relevant. It must be recalled, however, that the amplitude of the electric field oscillations at the UH layer do not correlate easily with the value measured outside the plasma as most of the EBW will be absorbed. The additional peaks at $\approx$ 8 MHz from the main peaks are still present even at these powers.
Even though it has been shown that the preferred operating gas would be hydrogen, it is still interesting to check if the predictions are validated for helium. A simulation with 1 kW of power and the same characteristics as Fig. 4.5 but using helium is shown in Fig. 4.12

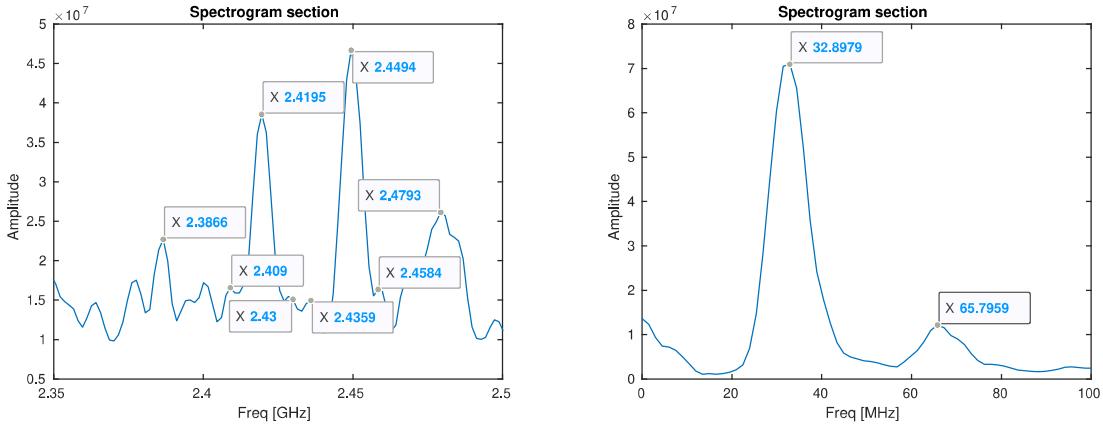

Figure 4.12: Time-integrated E_x spectrogram with the same parameters as Fig. 4.5 but using Helium. Focus on the high frequencies (left) and the low frequencies (right)

From the analytical model, the expected frequency for the LH daughter frequency is lower for helium than for hydrogen and is of $\approx$ 20 MHz. The value from the PIC simulation is of $\approx$ 30 MHz and comparable with the value obtained in hydrogen. This can be attributed to the ion and electron temperature being different in the two cases, while they were assumed to be the same in the analytical model, and is a useful reminder that even when using the same power and neutral pressure the characteristics of the decay may change due to the different responses to the heating beam of the two gases.

It is also interesting to plot the 2 dimensional Fourier transform of E_x, corresponding to a $k - f$ plot, where the different types of waves can be distinguished according to their dispersion relation $k(f)$. In Fig. 4.13 such a plot is shown for a simulation without pump wave. In this case, there are still some low-amplitude waves in the system, which are self-excited natural modes of the system. In particular, at high frequency, the dispersion relation of the warm X-waves and EBW waves is clearly visible and closely resembles the analytical dispersion relation shown in Fig. 2.4. The "thickness" of the dispersion relation is due to the non-homogeneous density of the plasma, which allows for a band of allowed k's at fixed f. In the low-frequency region, the lower hybrid oscillation can be noticed with a frequency close to the one of the daughter waves of the parametric decay but much smaller amplitude.

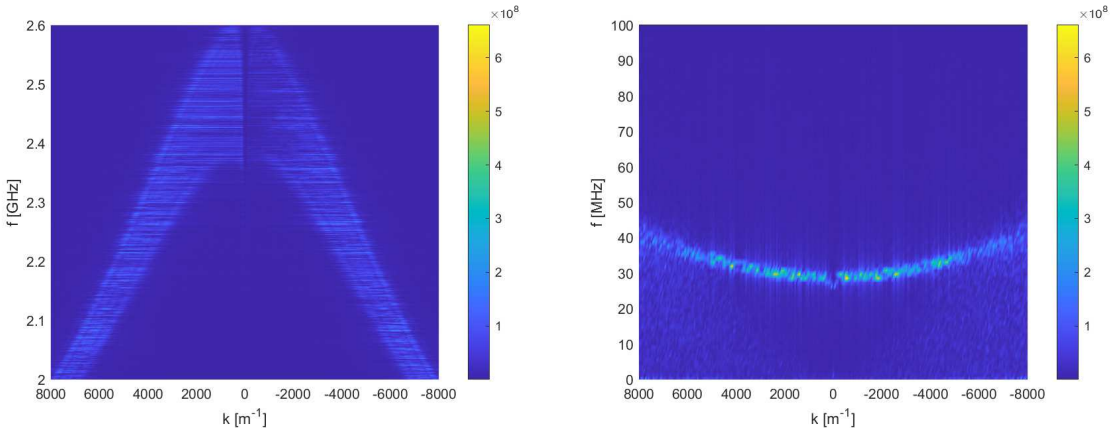

Figure 4.13: Dispersion relations for X-waves, EBW (right) and LH (left) waves in a shot with no pump wave and same parameters as Fig. 4.5 obtained as 2 dimensional FFT of E_x over the full simulation duration and length.

In Fig. 4.14, instead, a similar plot but with a 1 kW pump wave is shown.

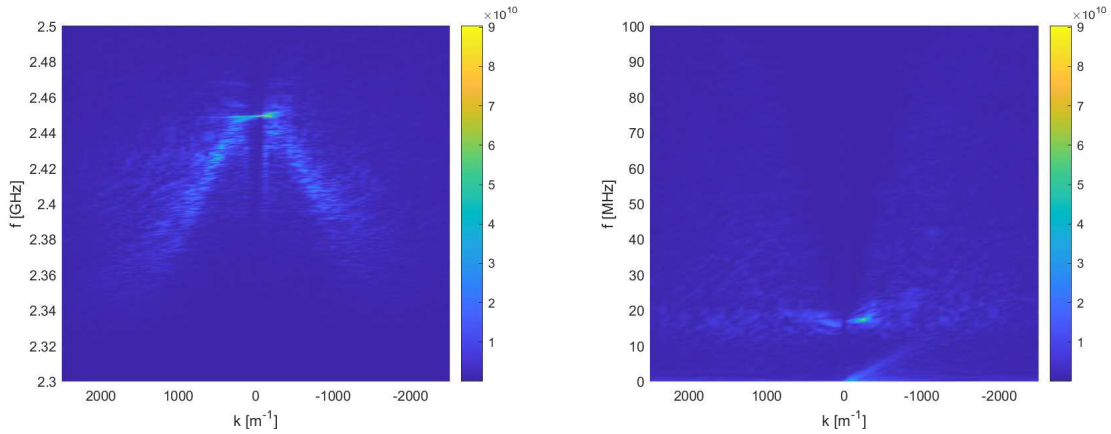

Figure 4.14: Dispersion relations for X-waves, EBW (right) and LH (left) waves in a shot with the same parameters as Fig. 4.5 obtained as 2 dimensional FFT of E_x over the full simulation duration and length.

In this case, some brighter "dots" can be seen on specific points of the dispersion relation corresponding to the k and ω values at the UH layer, where the field is amplified. The brightest dot at high frequency is given by the pump wave at a frequency of 2.45 GHz and on low $|k|$ branch of the warm X wave-EBW dispersion relation. For the conventions chosen in this representation, both the pump wave and the linearly converted EBW have a positive k. At the same frequency but on the high $|k|$ branch of the dispersion relation, another brighter area is present, which corresponds to the linear conversion at the UH layer. On the same branch but at the lower frequency of ≈ 2.42 GHz, the EBW from parametric decay can also be seen at negative k. In the low-frequency region, a brighter region corresponding to the LH parametric decay is also visible. As expected the k_1 value is positive as per the selection rules and given the negative value of k_2.

Having a consistent prediction for the daughter wave frequency from the analytical model and the PIC simulations that indicate the effect is present of non-negligible magnitude, it is now possible to try to measure it directly.

Chapter 5

Experimental Set-up and Radiometer Developement

In a typical tokamak experiment, a variety of diagnostics are usually mounted on the vacuum vessel through different access ports to measure the large number of experimental parameters that characterize a discharge. The most common diagnostics measure the fundamental parameters of the system: density, temperature and magnetic field. Often there is more than one type of diagnostic measuring the same quantity, for example, the temperature in the core and at the edge of large scale experiments are usually measured using different diagnostics due to the large difference in temperatures and the inaccessibility of the core plasma. A large variety of diagnostics has also been developed to study different effects happening during a discharge such as the fluctuations of the fundamental parameters and their relation to turbulence, the transport of fuel and ashes to and from the core plasma, the presence of instabilities and the dynamics and effects of impurities. These diagnostics cover a wide variety of physics fields ranging from the electrodynamics governing the Langmuir probes to active and passive spectroscopy in the infrared to gamma frequency range, the use of diagnostic neutral beams and calorimetry. An introduction to the most commonly used diagnostics can be found in standard textbooks [29]. NORTH is a small tokamak recently put into operation and while the development of new diagnostics is in progress, the main parameters of the plasma can be measured via a static Langmuir probe mounted on a manipulator and an amperometer for the current running through the coils. Additionally, the vacuum system includes a pressure gauge and the heating system includes a measurement of the injected and reflected power coming from the system. Finally, a photodiode is mounted outside the window to measure the light from the plasma and act as a quick and simple method to detect when the plasma is formed. As part of this work, a radiometer has been developed and added to the list of diagnostics operating in the tokamak. A schematic representation of the system with the diagnostics used in the PDI experiments is shown in Fig. 5.1 while Fig. 5.2 is a picture of the actual experiment with the relevant components highlighted.

In section 1 the vacuum vessel and pumping system are described. In section 2 an introduction to the functioning of the Langmuir probe is given. The development of the radiometer and its commissioning is covered in section 3 while in section 4 a description of the control system for the experiment is presented.

5.1 Vacuum and Heating Systems

The vacuum system is composed of a HiScroll-6 Scroll pump and a TPU-170 turbomolecular pump. The typical vacuum levels reached before the injection of the operating gas are of $\approx 10^{-7}$ mbar. The neutral gas pressure is measured by a ITR 90 pressure gauge that includes a Pirani gauge and a hot ion gauge that is switched on at lower pressures and its the one relevant during NORTH experiments. Hot cathode gauges give gas-dependent pressure measurements and so the pressure values saved by the control system must be corrected for using correction values. The control system described in section 5.5 was initially developed for helium plasmas and when switching to hydrogen the Labview program was updated to enable the possibility to select the operating gas and correcting the pressure

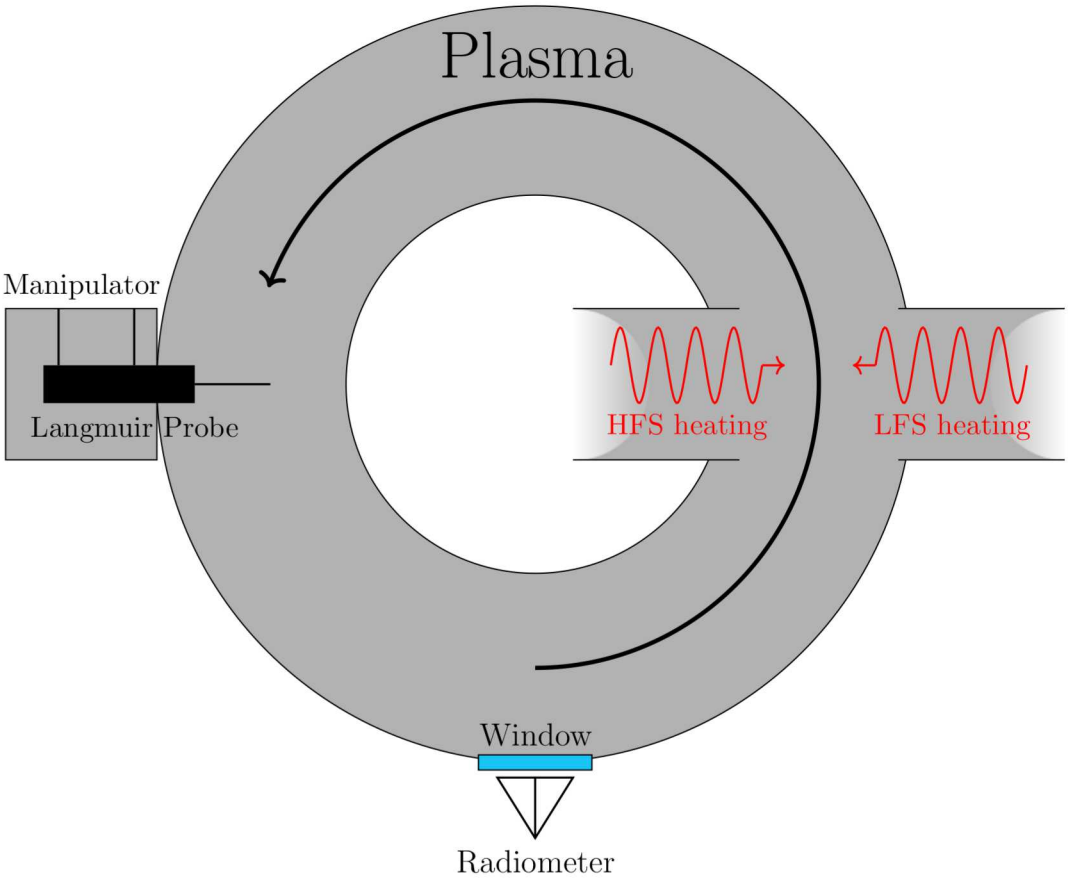

Figure 5.1: Schematic representation of the experimental setup

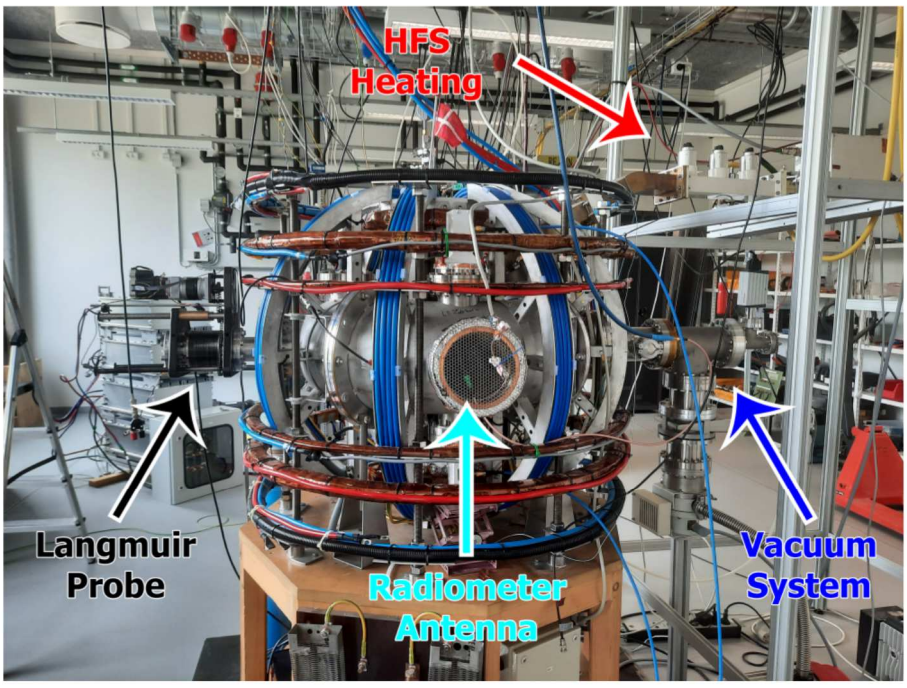

Figure 5.2: Picture of the experimental setup

Table 5.1: Pressure gauge correction factors

Operating gas	Ar	He	H
Correction factor	0.8	5.9	2.4

displayed accordingly. The correct background pressure can be obtained by multiplying the measured value by a gas-dependent correction factor, which for typical operating gases are shown in Tab. 5.1

A valve enables to puff the operating gas once a suitable vacuum is reached and a feedback system allows to increase the pressure until the requested value of pressure for the shot is reached. It is possible to shut down the valve during a shot or to keep the feedback system working. In the first case, the neutral pressure falls continuously during the shot while in the second case the pressure can start rising after a gas puff.

The heating system is composed of two SAIREM GMP 30 magnetrons operating with a maximum power of 3 kW at the nominal frequency of 2.45 GHz. A magnetron allows the generation of high-power microwaves at a specific frequency by accelerating electrons in a cavity whose geometry is designed to resonate with the specific frequency of interest. The spectrum generated by the magnetron tends to be cleaner at higher powers and the specifications given by the manufacturer are of (2.45 ± 0.025) GHz down to 300 W. Operating at very low powers results in a spectrum with significant contributions at other frequencies and so for the purposes of this work they have always been operated at powers greater than 200 W. The microwave generators can be controlled using a control panel mounted in the experimental room, inaccessible during experiments, an analogue port or an SR232 port. The control system described in section 5.5 uses the analog port to control the magnetrons remotely. One of the magnetrons allows the injection of O-waves radially from the LFS while the other magnetron is used for X waves injection from the HFS. The magnetrons are currently used only for heating but studies on current drive are possible. A further magnetron operating at 5.8 GHz is currently being commissioned and it will be used for 2nd harmonic X wave heating and parametric decay studies at the 2nd harmonic.

5.2 Langmuir Probe

A Langmuir probe is a metallic probe inserted into a plasma to measure its density and temperature at the tip of the probe. The physical principle is based on the difference in velocities between the electrons and ions that make up the plasma, due to their difference in mass $m_i \approx 1840\ m_e$. The larger speed of the electrons will lead to the accumulation of negative charge on the surface of the probe that will repel additional electrons and attract plasma ions until the ion and electron fluxes balance out and a steady state is reached. By applying an external voltage to the probe (**biasing**) it is possible to modify the equilibrium leading to an excess of one flux over the other and so to a measurable current. Scrape Off Layer (SOL) physics, describing the interaction of a plasma with the surrounding materials, is covered in most standard plasma physics textbooks [7] [29] [30] [2] and so it will not be repeated here. The main result is that the current measured by the probe is related to the externally applied voltage, for values smaller than the floating potential V_f[1], by

$$I = j_i A \left(1 - \exp\left\{\frac{e(V - V_f)}{T_e}\right\}\right) \tag{5.1}$$

where j_i is the ion current density and A is the projection of the surface area of the probe perpendicular to the magnetic field line. A plot of the current-voltage characteristic curve is given in Fig. 5.3.

The saturation behaviour in the left-most part of the plot is due to the probe already gathering all the ions available in the flux tube. A measure of this **ion saturation current**

$$I_{s,i} = j_i A = \frac{1}{2} e A n_0 v_i \tag{5.2}$$

[1]The potential reached by an electrically isolated object floating in the plasma

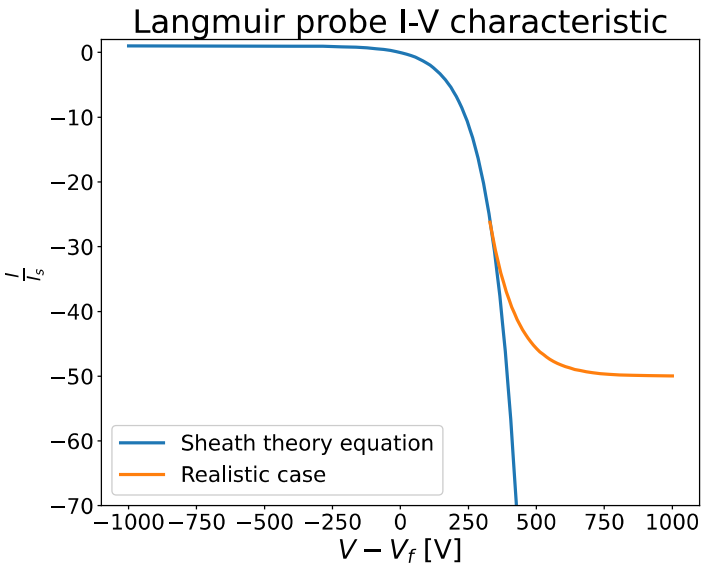

Figure 5.3: Langmuir probe I-V characteristic given by Sheath theory and an experimentally realistic case. The current saturates at low and high voltages as all the ions or electrons in the flux tube are collected.

allows extracting the ion density in real-time. While a complete saturation is only a first approximation, as when varying the voltage there is also a slight variation of the probe collection area and so of the number of ions collected, it grants a sufficient precision for the experiments of interest. The divergence at high V's is nonphysical and in practice when moving to very high voltages the opposite situation can be encountered, where all the ions are repelled and all the electrons of the flux tubes are collected. In this case, an electron saturation current will be measured

$$I_{s,e} = \frac{1}{4} e A n_0 v_{Te} \tag{5.3}$$

with $\frac{I_{s,e}}{I_{s,i}} \approx \left(\frac{m_i}{m_e}\right)^{\frac{1}{2}}$ however this portion of the characteristic curve is rarely used. In the central region of the plot, a temperature-dependent exponential rise in current is present and by fitting measurements at different applied voltages, the value of the electron temperature T_e can be obtained. The requirement of having different measurements to perform a fit poses a limit on the time resolution of the temperature measurements, as the scan over the voltages cannot be too fast. This makes the standard Langmuir probe unsuitable for the measure of high-frequency temperature fluctuations but a cheap and robust diagnostic for the background temperature in low-temperature plasmas. In NORTH there is a single Langmuir probe currently operating and completely integrated in the diagnostic framework but a high-frequency probe was added during the final set of measurements and an array of quickly moving probes is currently under development. The current probe is mounted on a manipulator that can be controlled remotely from the control room with a precision of ≈ 1 mm. The movement speed of the manipulator is low and the time required to move the probe is currently longer than typical discharge times. To obtain a profile for the characteristic quantities in the experiment, measurements during different discharges in the same experimental conditions need to be taken. Assuming the shapes of the profiles do not vary significantly during different discharges, the profile for a particular discharge can be obtained by normalizing the general profile to the measurement in a single position performed during the discharge of interest. In the future, the entire profile will be measured for each discharge using the fast moving probe array currently in development.

5.3 Radiometer Design

To measure the characteristics of the parametric decay process of interest, it is possible to measure the waves coming out of the plasma using an antenna and look for the high-frequency daughter waves involved. As mentioned in chapter 2, the high-frequency daughter waves are Electron Bernstein waves and so they cannot propagate outside of the plasma, as there are no free electrons to oscillate coherently. However, these same waves can be converted to X-waves near the Upper Hybrid layer (section 2.2), allowing their indirect measurement outside of the plasma as electromagnetic waves.
When sampling a signal with a discrete number of points the sampling rate must be high enough to correctly determine the frequencies that compose the signal. This is due to the fact that for a fixed sampling rate f_s a sinusoidal wave oscillating at either frequency f_0 or $f_s - f_0$ will result in the same sampled points, making them indistinguishable. This phenomenon is called aliasing and typical reconstruction algorithms always assume the lower frequency to be correct. To sample correctly a signal with frequencies up to a value $f^\star$, the minimum sampling frequency required will then be $f_s^\star = 2f^\star$. For the case of interest in this work, this would require a digitizer sampling at ≈ 5 GS/s. Such a fast digitizer was not available during the measurement campaign and instead, a mixer has been used to lower the frequency of the incoming signal in the MHz range, a more manageable value. A mixer is a non-linear electronic circuit that outputs a signal given by the product of an incoming signal (RF) with a reference signal called "local oscillator" (LO). Considering as an input a sinusoidal wave with frequency f_{RF} and a local oscillator with frequency f_{LO}, the output (IF) will be given by the sum of two sinusoidal waves: one oscillating at frequency $f_{RF} + f_{LO}$ and one at $|f_{RF} - f_{LO}|$. By using a voltage-controlled oscillator (VCO) to generate a LO signal at 2.4 GHz it is possible to "mix-down" the original 2.45 GHz wave to measurable levels. An ideal mixer will only output the $f_{RF} - f_{LO}$ frequency of interest but in practice, higher harmonics can also be present as well as feed-through of the original signal. To limit the bandwidth of the instrument and avoid picking up unrelated signals a high pass filter and a low pass filter have been included in the design. In particular, a high pass filter with nominal band 950 - 3200 MHz has been added at the start of the analog chain for an initial filtering of the signal, removing the low-frequency noise, while a low pass filter with nominal band DC - 58 MHz has been added after the mixer to filter out the high-frequency noise and the harmonics coming from the mixer itself. The signal coming for the plasma could yield powers of up to $\approx 2W$, too high of a value for many electronic components. To avoid damaging the equipment various attenuators, as well as a limiter, have been added to the design. The attenuators act as the opposite of an amplifier, reducing a signal instead of amplifying it. While this was necessary to protect the apparatus, it also comes with the added difficulty of suppressing the daughter waves of interest, already expected to be some orders of magnitude weaker than the pump signal. As conventional in microwave system design, the signal attenuation will always be reported in dB and the signal in dBm, where

$$0\text{dBm} = 1\text{mW} \qquad 10\text{dBm} = 10\text{mW} \qquad 30\text{dBm} = 1\text{W} \tag{5.4}$$

The nominal attenuation in the system given by actual attenuators is 16 dB but in general, to every component corresponds a certain degree of signal loss. This is usually negligible with respect to the attenuators with the notable exception of the mixer, with a conversion loss of $\approx 6 - 7$ dB when converting from the RF signal to the IF one. A limiter, a type of circuit that clips the signal if it grows past a fixed threshold, has also been added to ensure that the power reaching the mixer always stayed inside the technical specifications of the model. The schematic of the radiometer designed to account for the mentioned factors is shown in Fig.5.4 while the specific models involved are reported in Tab.5.2

The LMX2572EVM board by Texas Instruments has been used as local oscillator. It is a programmable board that requires a power source and USB connection to a PC. The oscillation frequency can be set using the GUI of the Tics PRO software provided by the manufacturer. While this requirement of a constant connection to a PC grants the flexibility to easily change the controlled frequency, it also complicates the setup. To minimize the space occupied by the radiometer, a mini-pc has been used as a permanent part of the design. By connecting it temporarily to a screen it has been set

Component	Model
10 dB Attenuator	6606-SMA-50-1/199$_N$
High pass filter	VHF-880
Limiter	ZFLM-43-5W+
Mixer	ZFM-15-S
VCO	LMX2572EVM
Low pass filter	BLP-70

Table 5.2: Components list used in the radiometer

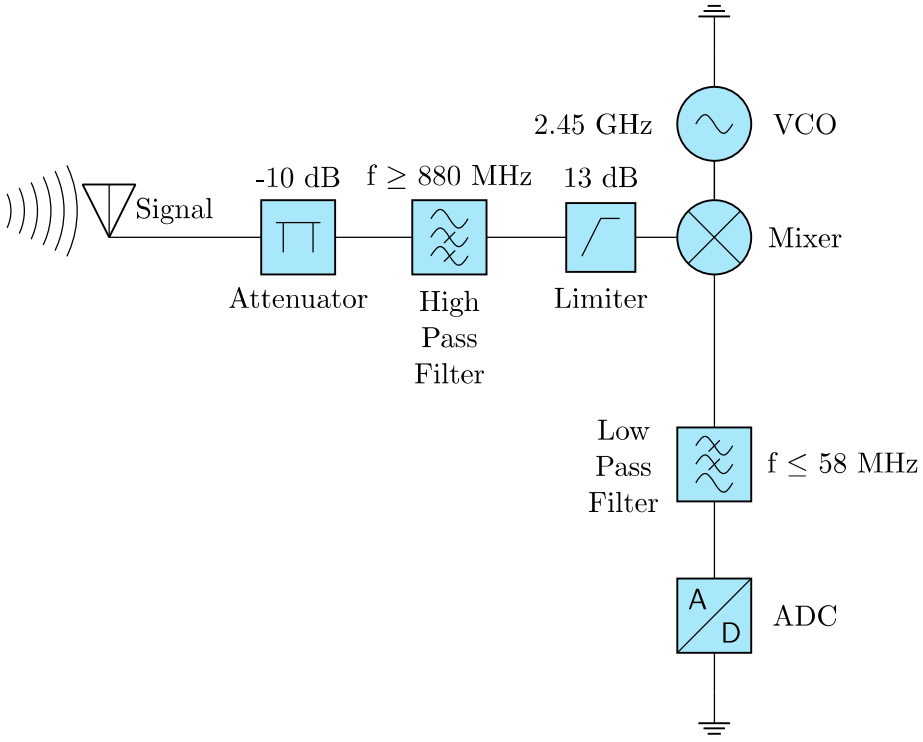

Figure 5.4: Schematic representation of the radiometer

up with the Tics PRO software and a VNC program to control the computer remotely. In this way, it is possible to connect remotely to the mini-pc situated in the experimental room from the control room to change the VCO frequency. This has two advantages compared to a traditional PC: it keeps the space requirements for the radiometer small while also making it accessible without entering the experimental room, which is inaccessible during the experiments for security reasons. For the ADC two possibilities have been used: the tektronix DPO-7104 oscilloscope and a Red Pitaya board. The oscilloscope has a bandwidth of 1 GHz and can sample up to 2 GS/s. It also has access to a large memory disk, allowing it to sample for very long times. The DPO-7104 model has a Windows XP operating system and so the Remote Desktop feature available for Windows XP has been used to control the acquisition remotely and save the data on the control room memory disk automatically. This was necessary as for security reasons the experimental room in inaccessible during the discharges. The large bandwidth is really useful for the first measurements as it allows a bird's-eye view of the spectrum but it is not really suitable to be a long-term part of the setup due to its large cost and dimension. In its place, the use of a Red Pitaya board has been considered to work as ADC in the final setup. A Red Pitaya can nominally sample up to 125 MS/s and is simultaneously very compact and cheap. The main drawback of this acquisition system is the limited memory of the buffer, which can only store 16 thousand samples. This means that for a given sampling frequency the measurement time is limited and for the frequencies of interest it is generally too low. Considering for example the maximum sampling frequency, 125 MS/s, the maximum duration of the measurement would be of 128 μs. To measure for longer times a streaming feature was enabled on the acquisition board. This feature enables continuous measurements that are streamed directly via ethernet to the control room. Once this feature is enabled via the Red Pitaya GUI from the control room, the continuous acquisition starts but the data is not actually saved unless a cmd command is sent by the control PC. The passage from a passive streaming mode to actually saving the data is not performed via the trigger system that drives the other diagnostics (section 5.5), so the acquisition is usually started before the discharge and the traces are time-aligned during the data analysis. While the sampling rate for the direct acquisition can go up to 125 MS/s, this is nominally reduced to 62.5 MS/s when operating in streaming mode. This would lead to an acquisition bandwidth of $\approx$ 30 MHz that, while narrow, would still be just enough to measure the decay at the expected frequencies if the VCO was set exactly at the frequency of the pump wave. In practice, as it will be described in the next section, when sampling at such a high frequency the board is unable to transfer the data out of the buffer fast enough and some losses occur. This leads to a further reduction of the effective bandwidth and distortion of the measured frequency that was characterized experimentally. In Fig.5.5 a picture of the radiometer setup is shown, where the final signal is split between the oscilloscope and the Red Pitaya.

5.4 Radiometer Characterization

The three main components in the design with unknown behaviour that need to be studied in more detail are the VCO, the mixer and the Red Pitaya. In section 5.4.1 the performance and characteristics of the VCO and the mixer will be studied while in section 5.4.2 the functioning of the Red Pitaya in streaming mode will be described.

5.4.1 VCO and Mixer Signals

The quality of the spectrum generated by the LMX2572EVM board was checked using a spectrum analyzer. The spectrum shown in Fig. 5.6 is for a nominal signal of 2 GHz. The presence of harmonics of the requested signal is evident as is the small reduction in amplitude between the main signal and its harmonics.

Fortunately, the mixing of the RF signal with higher harmonics leads to frequencies significantly higher than the ones measured by the oscilloscope or the Red Pitaya. A low pass filter is present between the VCO and the mixer to cut low frequency at frequencies lower than 880 MHz. While a high-pass filter could also be added to the system to select only the 2 GHz frequency this would lead to a reduction of the signal power driving the mixer. The maximum amount of signal that can be driven

Figure 5.5: Picture of the radiometer setup.

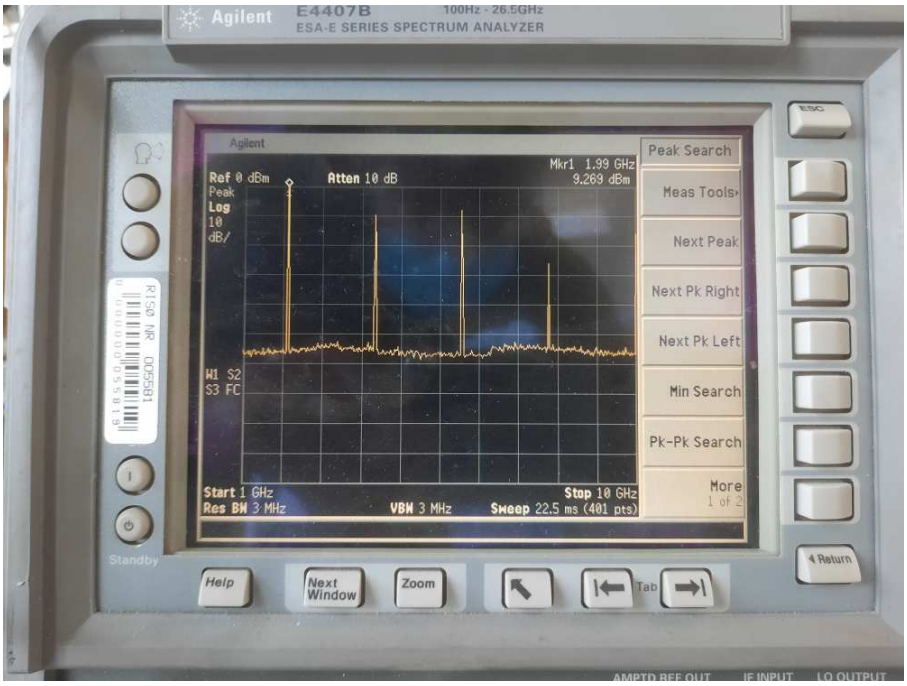

Figure 5.6: Spectrum measured by the spectrum analyzer for a nominal signal of 2 GHz. Harmonics at multiples of the nominal frequency are also present.

using the VCO is 8 dbm, close to the lower limit of 7 dbm necessary to drive the mixer. This would mean that in addition to the filter an amplifier would also be required, along with the corresponding power supply. To favor a compact design it was elected to connect the VCO to the mixer using only the low pass filter but a high pass filter and an amplifier could be added to the radiometer in the future to increase the range of applicability of the diagnostic. To simulate an incoming RF signal, a second LMX2572EVM board was used and while keeping the frequency of the local oscillator fixed at 2 GHz, the frequency of the RF signal was scanned and the resulting signal was measured by the oscilloscope. In Fig. 5.7 the spectrogram of the signal along with its section in the middle point of the x-axis is shown. In both plots, the measured frequency has been shifted by the LO frequency to reconstruct the original value.

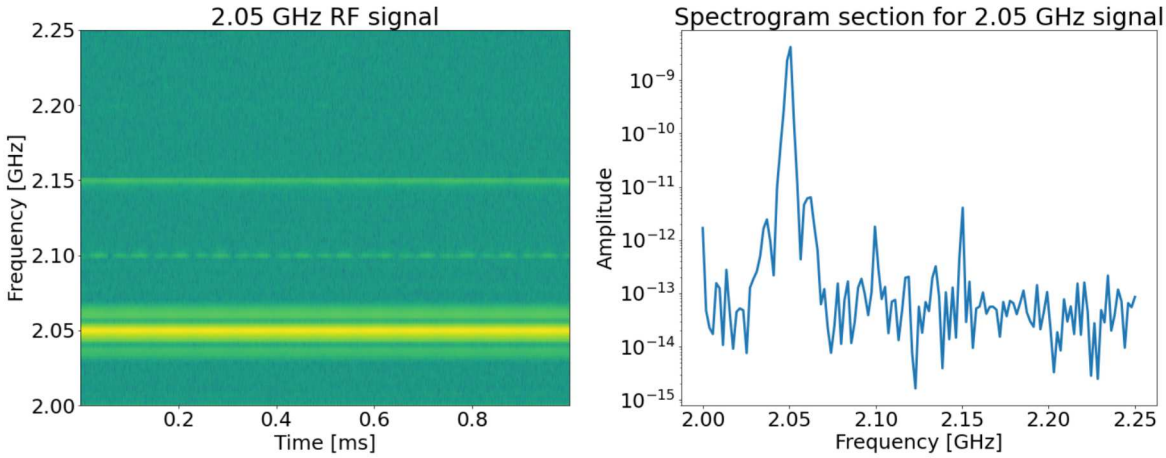

Figure 5.7: Spectrum measured by the oscilloscope for a nominal signal of 2.05 GHz and a LO frequency of 2 GHz.

The first thing that can be noticed is the main peak at the nominal signal of 2.05 GHz, as would be expected. Then, recalling that the signal measured by the oscilloscope is actually at 50 MHz, the harmonics of the mixer signals are also visible. These peaks are a factor of ≈ 1000 times smaller and should be significantly distant from the main peak to be distinguished clearly. Finally, two additional peaks can be noticed next to the main peaks, shifted by $\approx \pm 10 - 15 MHz$. These peaks cover the positions where the daughter waves from the parametric decay are expected and so it becomes a priority to minimize their amplitude. To this end, it is important to understand their origin. In this case, as was verified using the spectrum analyzer, the peaks do not come from physical signals but are an artifact of the Discrete Fourier Transform performed on the signal to create the spectrometer. This effect is due to performing a Fourier transform on a signal that does not extend infinitely in time and is instead performed on a "window" of the signal. To improve the results of the transform it is possible to perform a convolution of the signal with specific filters that avoid the sudden discontinuity at the edges of the interval over which the transform is performed. Many types of filters or "windows" are present in the literature, often having little difference in the result of their application. The default window used by scipy is the Tukey window, while to suppress the peaks a Blackman window was applied instead. Both windows are shown in Fig. 5.8

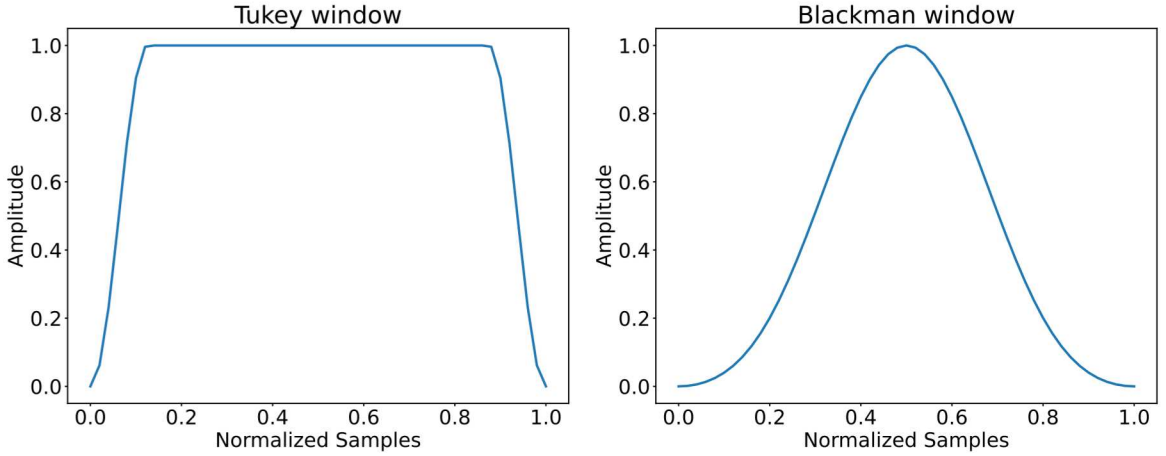

Figure 5.8: Tukey and Blackman windows used in the Fourier transform of the signals

A comparison of the same signal as in Fig. 5.7 with both types of windows is shown in Fig. 5.9 and the improvement is evident. Using the Blackman window, the height of the two phantom peaks surrounding the RF signal drop significantly to rumor-like levels.

It is now possible to determine the error in the reconstruction of the known RF frequency by scanning the nominal frequency requested by the second VCO and comparing it to the maximum

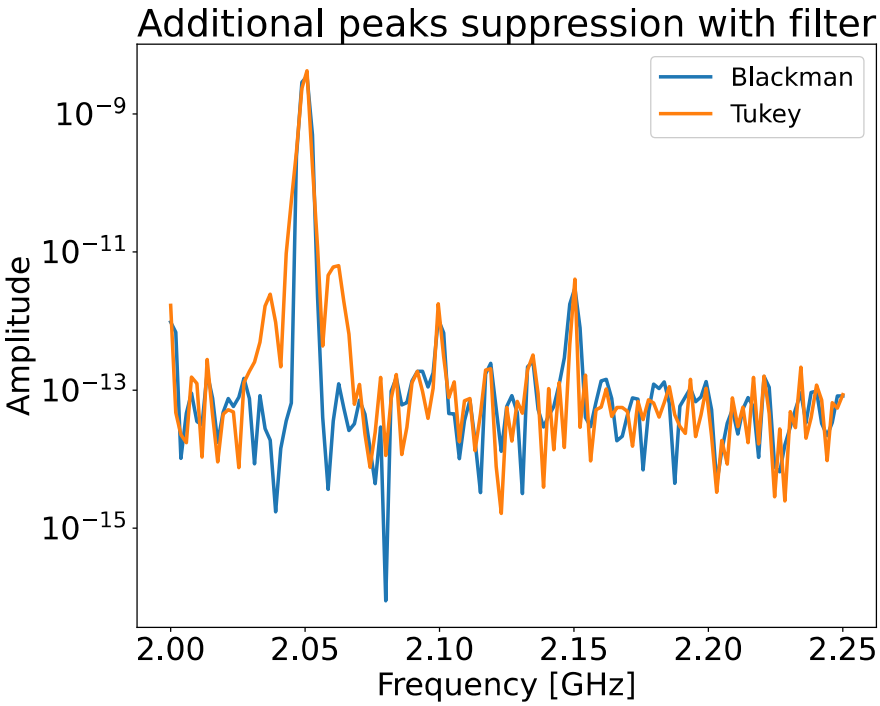

Figure 5.9: Comparison of signal reconstructed using the Tukay and Blackman filters. Using the Blackman filter the additional peaks generated by the discrete Fourier transform are suppressed.

Fourier component of the spectrogram. The relative error performed in the reconstruction is shown in Fig. 5.10

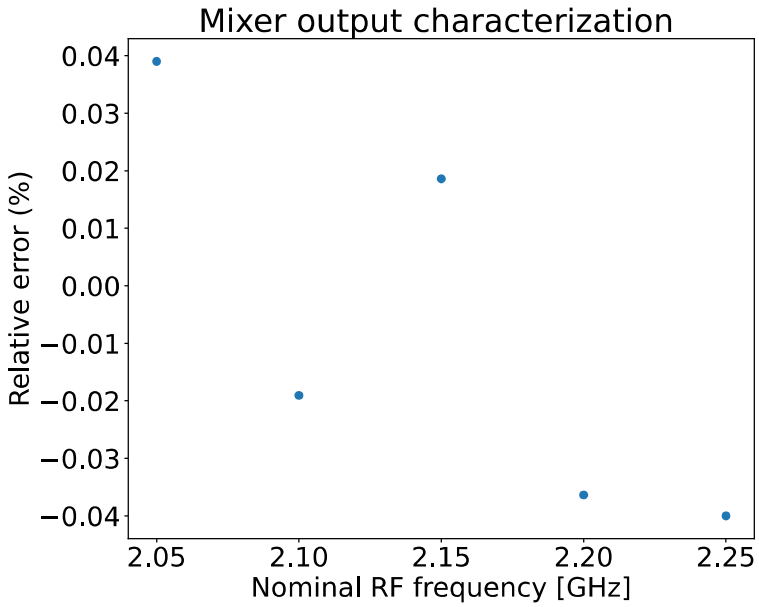

Figure 5.10: Relative error in the RF signal reconstruction

The relative error is quite small in the entire region covered by the ADC and negligible with respect to the other sources of uncertainties in the system.

5.4.2 Red Pitaya Acquisition in Streaming Mode

From the Red Pitaya GUI interface, the streaming options can be set, as shown in Fig. 5.11. In particular, the resolution, the sampling rate and the format of the file can be chosen.

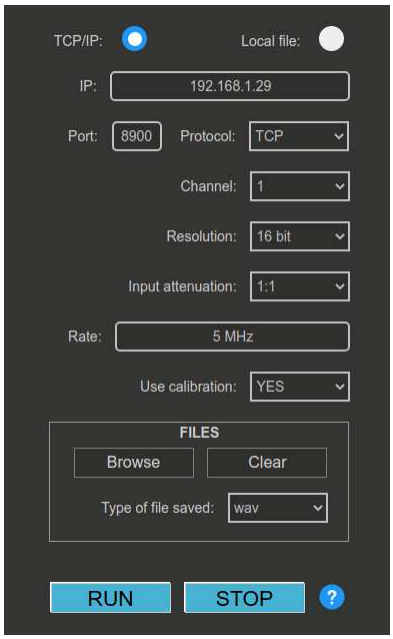

Figure 5.11: Red Pitaya streaming server setup

Both "wav" and "tdms"[2] formats are available but when saving in wav the amplitude of the signal is normalized, effectively losing the information on the signal strength. This has lead to choosing the tdms format instead even if it requires supplementary libraries for reading and handling the data. Using a function generator the Red Pitaya was used to acquire sinusoidal signals of known frequency with different sampling rates to study the ADC losses and their effect on the frequency determination. It is not possible to set arbitrary sample rates but only integer fractions of the maximum sample rate of 125 MS/s and the division factor is called decimation. In Fig. 5.12 the spectrograms of a signal at 5 MHz sampled at different frequencies are shown as an example.

It can be noticed how the amount of losses, corresponding to the interruptions along a line, increase with the sampling rate and that this is accompanied by a shift toward higher frequencies of the maximum Fourier component in the graph. To improve the determination of the frequency a correction factor can be included in the nominal sample rate given as input for the creation of the spectrogram. As the Red Pitaya writes in a log file the amount of data packets lost, an effective sample rate can be defined as the mean rate of acquisition of correctly sampled data points

$$f_s^\star = \frac{1}{1 + \frac{Losses}{Samples}} f_s \tag{5.5}$$

A comparison between the nominal sample rate and the corrected one for a signal at 5MHz and one at 10 MHz are compared in Fig. 5.13

As expected the nominal and corrected values converge for high decimation factors, where the sampling rate is low and so are the losses. The maximum corrected sample rate is of $\approx 40MHz$ and so using this setup only waves with frequencies ≤ 20 MHz can be measured when using the maximum allowed sample rate. The reconstructed frequencies are compared to the nominal value for the two signals in Fig. 5.14 and the improvement obtained with the correction can be noticed.

The deviation of the 10 MHz signal sampled at 21 MHz from the nominal value is due to the fact that the effective sample rate falls under the Nyquist frequency $f_s^\star < 2f$ and so the reconstruction is incorrect.

A scan over the signals at the same frequency but with different amplitudes was also performed to check the linearity of the ADC and the relation linking the nominal amplitude with the corresponding Fourier amplitudes. The scan was performed using a sinusoidal signal coming from the function generator with a frequency of 5 MHz and a sample rate of 62 MHz.

[2]Native format developed by National Instruments

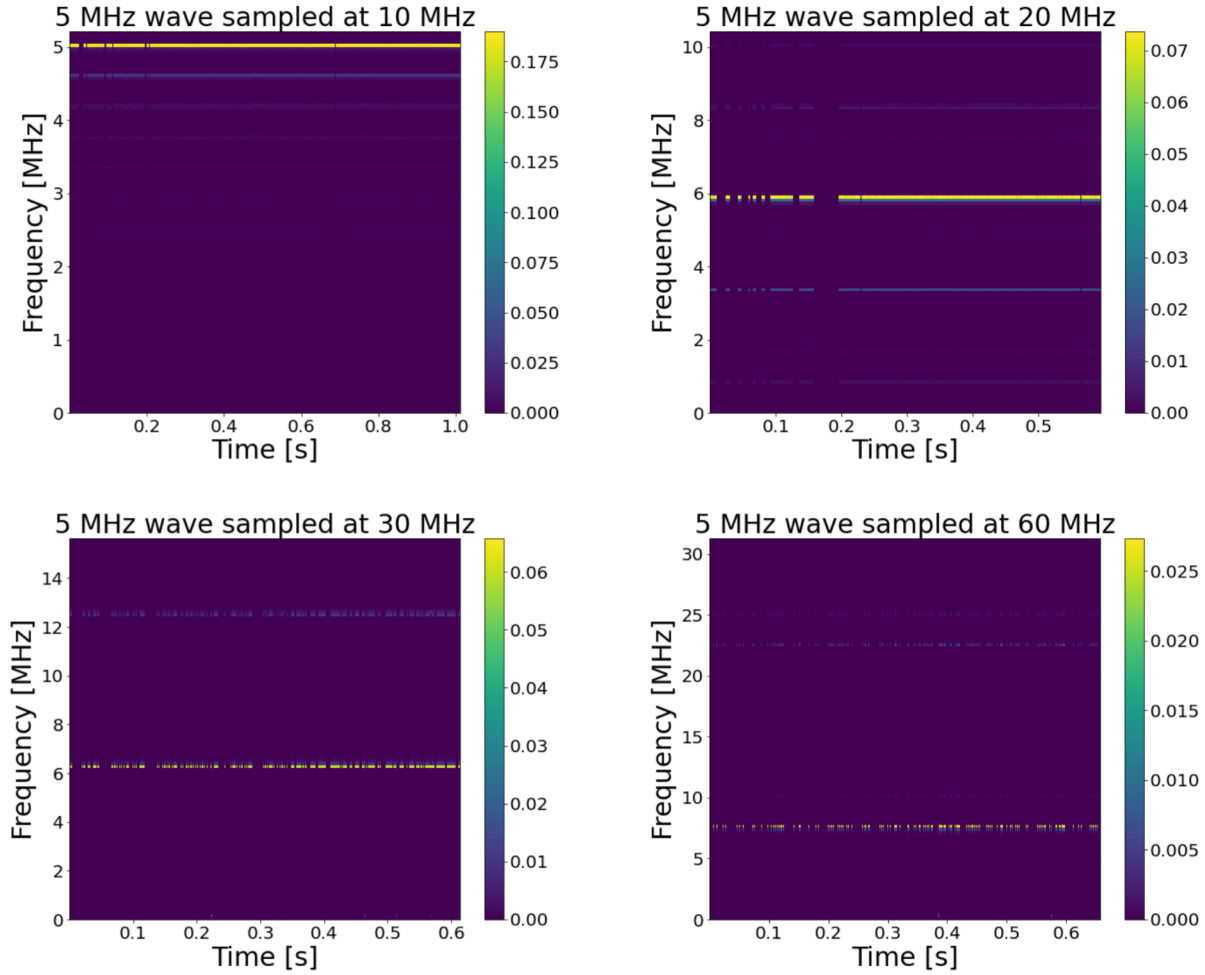

Figure 5.12: Red Pitaya acquisition of 5 MHz signal in streaming mode. Increasing the sampling rate also increases losses and the error in the frequency determination.

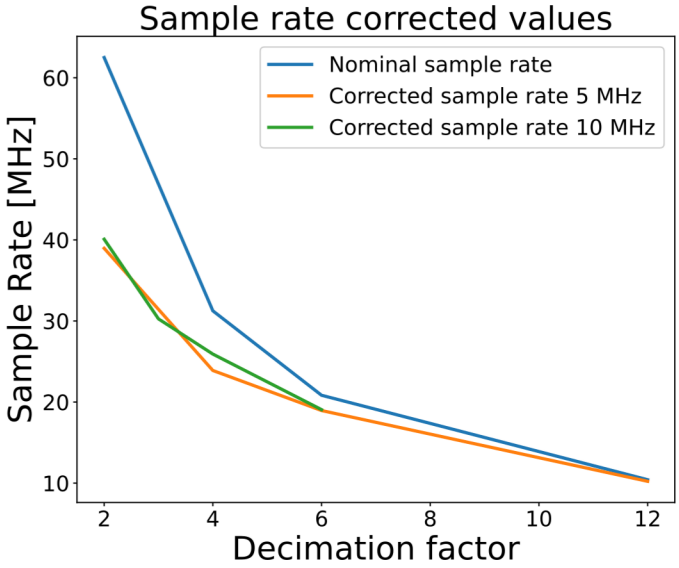

Figure 5.13: Nominal and corrected sample rates. The effective maximum sample rate is of 40 MHz.

In Fig.5.15 it can be seen that the ADC is indeed very linear and the residuals from the line of best-fit decrease with the strength of the signal. Analogously the Fourier components are well represented

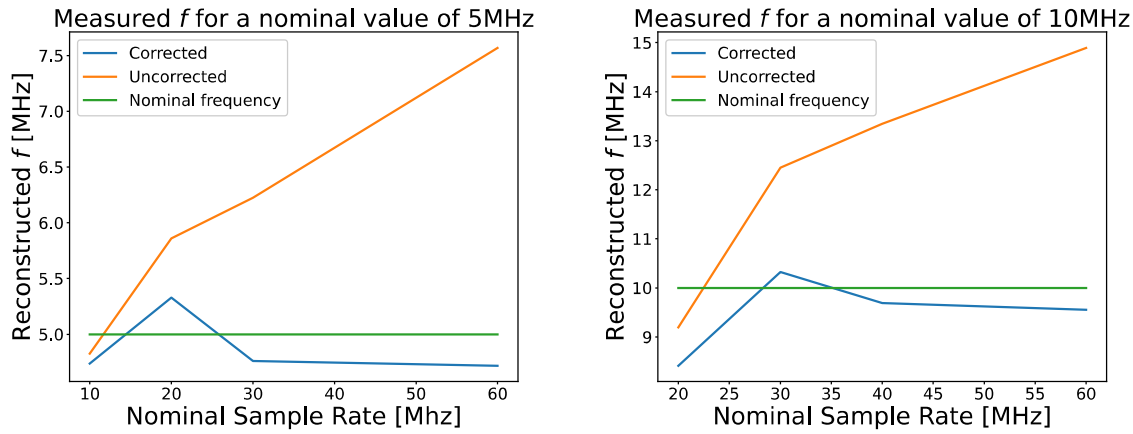

Figure 5.14: Nominal and corrected frequency determination. Using the correction factor, the error on the measured frequency becomes significantly lower at high sample rates.

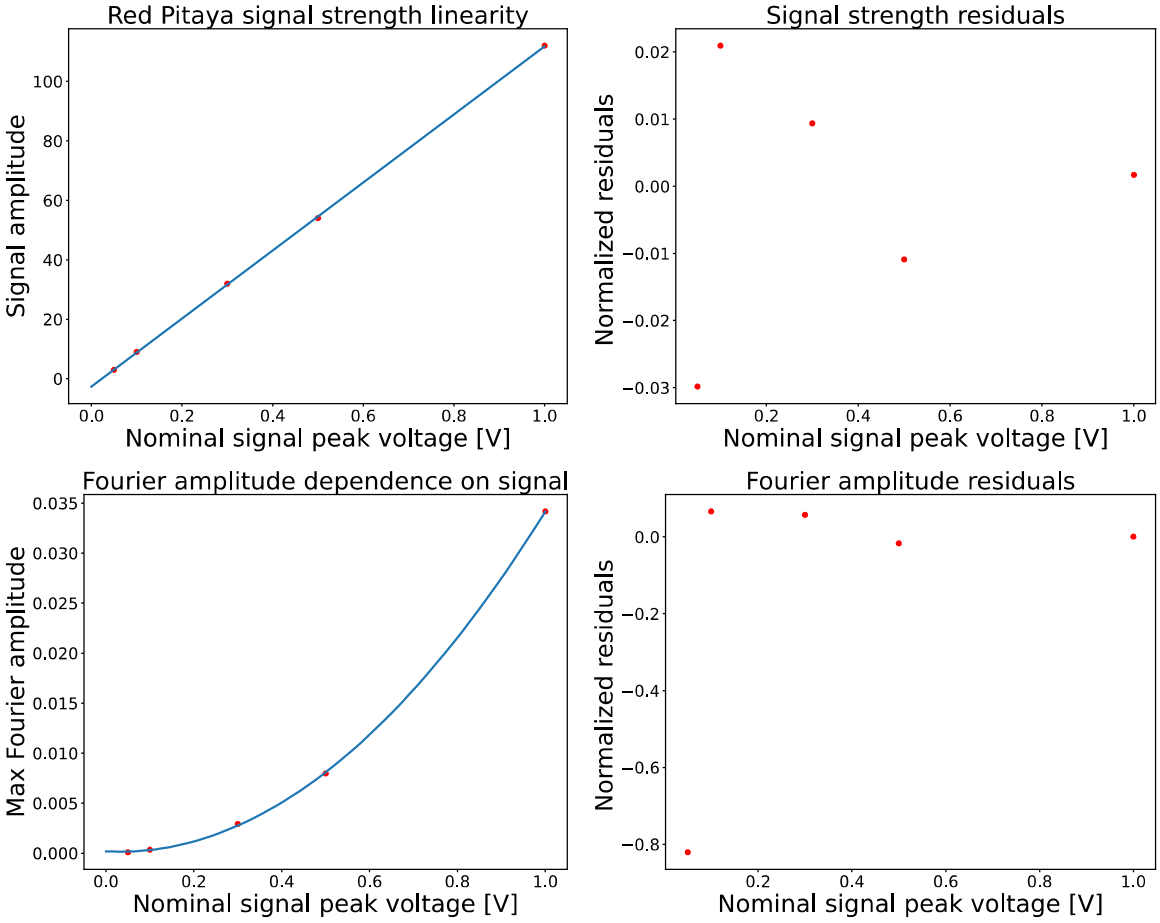

Figure 5.15: Red Pitaya signal linearity. The response is strongly linear with the amplitude of the signal with slightly larger errors at lower signals.

by a quadratic function but in this case, a larger deviation is present at very small signal strength. This is attributable to the small signal-to-noise ratio at such low signals.

5.5 Control system

NORTH is controlled by a PC situated in the control room that can be accessed remotely and so potentially suited for remote experimentation. The system is controlled by a Labview script with a

graphical interface where the characteristics of the discharge can be set. In particular, the different sections of the interface allow the user to

- Monitor the pressure inside the system and set the target pressure of the gas, which will then be puffed in the vacuum chamber before the discharge by a valve.
- Set the position of the Langmuir probe via the manipulator and the trigger delay after which the probe measurement starts. For the measurements using the oscilloscope as ADC, the same trigger has been used for both diagnostics.
- Set the target power and delay for both the HFS and LHS heating systems. Each system allows to set up 4 target heating powers to be reached after different delays and this allows to perform more complex experiments, for example performing scans over the power in a single shot or switching the power above and below a certain threshold.
- Set and vary the magnetic field during the discharge by setting either the current in the coils or directly the desired magnetic field. A similar 4-point control system exists as for the heating system.
- Set the discharge length, distribute the Shot number and start the discharge

The shot distribution system controls the entire system in a coordinated and modular way. Each part of the system is independent and shares information with a common MySQL database. When in standby, every independent section listens for a change in the Shot number, that acts as a pre-trigger. Once a component notices a change in the shot number it will prepare for the acquisition and log the relevant information to the database. This operation lasts in the order of a second and once everything is ready for the shot the "CRIO" light will turn from red to green in the control panel. At this point "Start Discharge" will send a physical trigger, much faster than communicating via database, to the different systems and the discharge will start. All the data is saved directly to the database and is accessible remotely for data analysis. A picture of the control panel is shown in Fig.5.16.

Figure 5.16: Control Panel to start NORTH discharges

This setup has been used to control the PDI experiments that are described in the next chapters.

Chapter 6

PDI experiments on NORTH

The radiometer designed and commissioned as part of this work has been used to characterize both the HFS and LFS heating system. This allowed checking the nominal characteristics given by the manufacturer and the coupling of the heating system to the vacuum vessel. Measuring how the heating frequency varies with power is also useful to determine the characteristics a notch filter would need to have in order to shield the radiometer from the high power pump wave while still allowing it to measure the daughter waves. The results of the characterization are reported in section 6.1. The power dependence and spatial variation of the plasma density and temperature were studied using the Langmuir probe to validate the assumptions made in chapter 3 and the results for both hydrogen and helium are reported in section 6.2. The measurements with the radiometer made in a helium plasma and a hydrogen plasma are reported in sections 6.3 and 6.4 respectively.

6.1 Heating System Characterization

The heating system is composed of two SAIREM GMP 30 magnetrons with a nominal frequency of (2.45 $\pm$ 0.025) GHz. In practice, the spectrum is not composed of a single 2.45 GHz line but it is more complex and it evolves with power. The system was characterized experimentally using the radiometer in order to distinguish the peaks measured during PDI experiments due to plasma effects from the ones coming from the coupling of the heating system to the vacuum vessel acting as a cavity and so independent of the plasma. To compare spectra at the two ends of the possible input powers allowed by the system, in Fig. 6.1 the spectra measured by the radiometer for the HFS system running at 400 W and 3 kW are shown.

The spectrum is rich in features in both cases and it is vital to distinguish these peaks from the ones coming from the parametric decay instability. The first features that can be noticed are related to the main peak: the heating frequency shifts to higher frequencies at higher powers and the width of the main peak decreases with power. As when dealing with reference signals in chapter 5, signals at the two and three times the mixed-down frequency are present, they are generated by the mixer and not by the heating system but they are easily distinguishable. An identical peak at 2.5 GHz is present in both cases. This peak is present also when the heating system is completely turned off and when the antenna is not connected to the mixer. The signal is either being generated or picked up by the VCO but it is identical in all spectra and can easily be disregarded. Additional peaks, such as the 2.404 GHz peak for the 400 W signal, are given by the mixing of the pump wave with the 2.5 GHz signal coming from the VCO. In the case of the 3 kW signal, the 2.436 GHz signal and the 2.564 GHz signal correspond to the sum and difference of the pump wave frequency with the 2.45 GHz signal. The mixing of the pump wave with this signal leads to a peak shifted of some MHz to the left of the pump wave, exactly where the parametric decay is expected and so particular care should be taken in not confusing the two types of signals. The frequency drift with power for the HFS magnetron is shown in figure 6.2

The drift in the operative region of the magnetron is of about 10 MHz. While this value is much smaller than the bandwidth of the oscilloscope, allowing to set a constant LO frequency for any heating power, due to the smaller bandwidth of the Red Pitaya either the VCO frequency must be changed

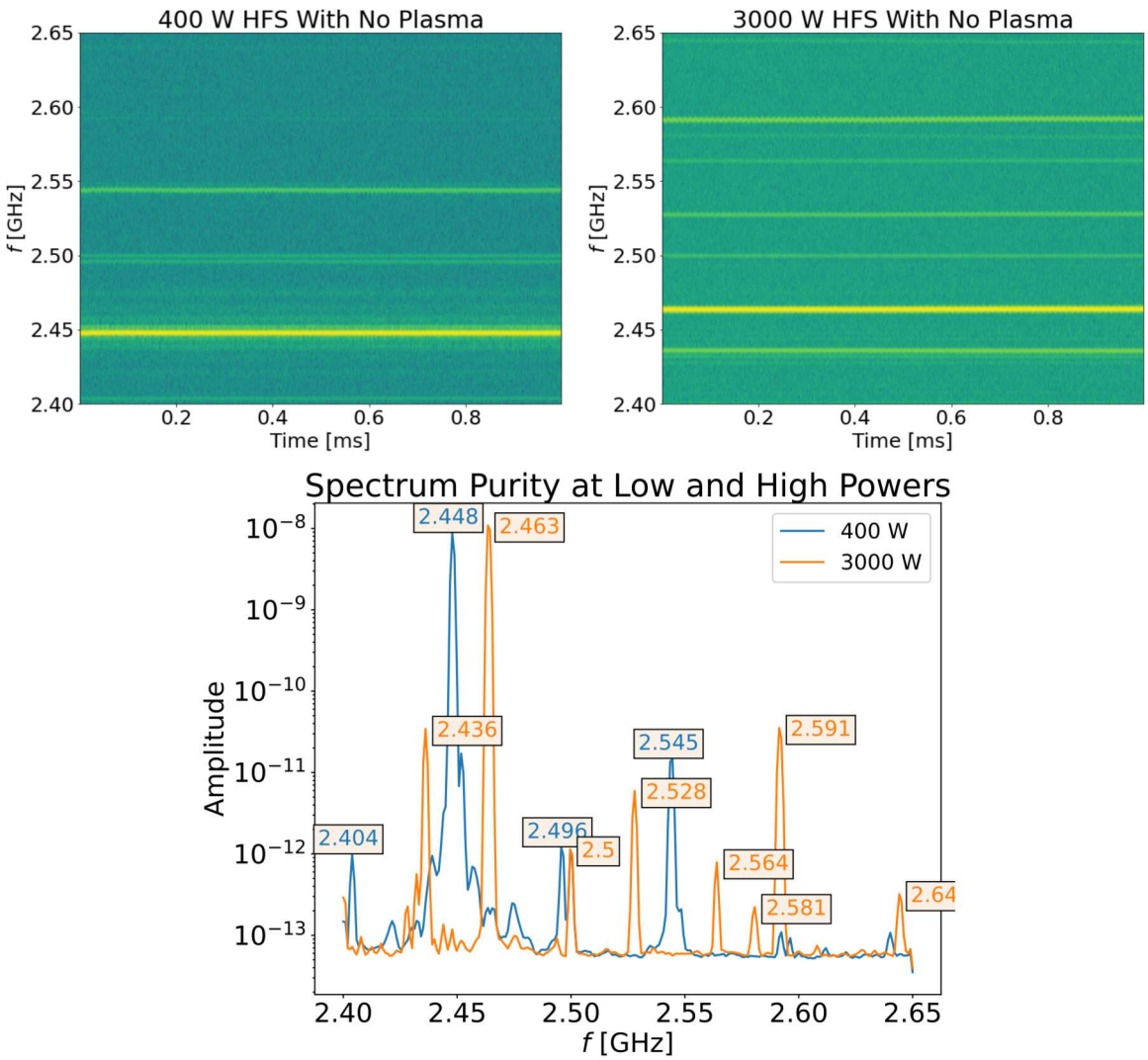

Figure 6.1: Comparison of magnetron spectra at 400 W and 3 kW for HFS magnetron with no plasma. The main peak at in the 3kW shot is more defined.

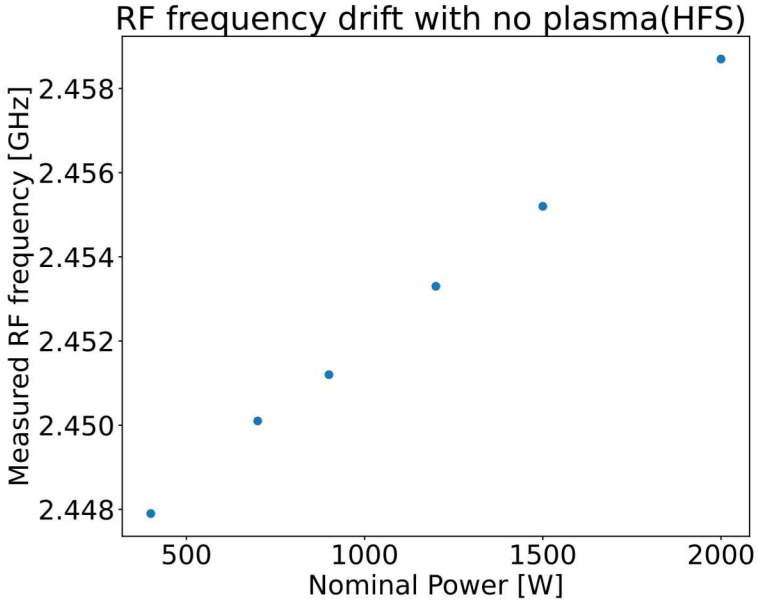

Figure 6.2: Frequency drift with power (HFS)

depending on the requested power or a homodyne system should be used instead of a heterodyne one. While it is possible to change the LO frequency to a lower value and shift all the frequencies upwards in order to free the region near the pump wave from unwanted signals, this would bring the frequencies out of the Red Pitaya bandwidth range. Alternatively, the LO frequency could be increased but this could make the frequency of the down-shifted high-frequency daughter wave smaller than the LO one and lead to a measured frequency of

$$f_2^\star = f_{VO} + |f_{VO} - f_2| \tag{6.1}$$

which is mirrored around f_{VO} and would complicate the interpretation of the spectrum.

6.2 Plasma Temperature and Density Characterization

After having studied the response of the heating system and the radiometer in vacuum, in the following section, the response of helium and hydrogen plasmas are studied to confirm that the characteristic quantities assumed in chapter 3 are representative of the system. The electron temperature and density characteristics were studied, using the Langmuir probe described in section 5.2, for different heating powers using both the LFS and HFS magnetrons. It is instructive to start from the analysis of a single shot before moving on to the study of the parameters variation with the heating power. In Fig. 6.3 is shown the output of the control diagnostics for shot 2162, performed with 500 W of nominal heating power from the LFS in helium. In particular, starting from the top and moving towards the bottom, different control quantities are shown: the current in the toroidal coils (proxy for the magnetic field), the pressure inside the vacuum vessel, the power of the LFS magnetron and the output of the photo-diode.

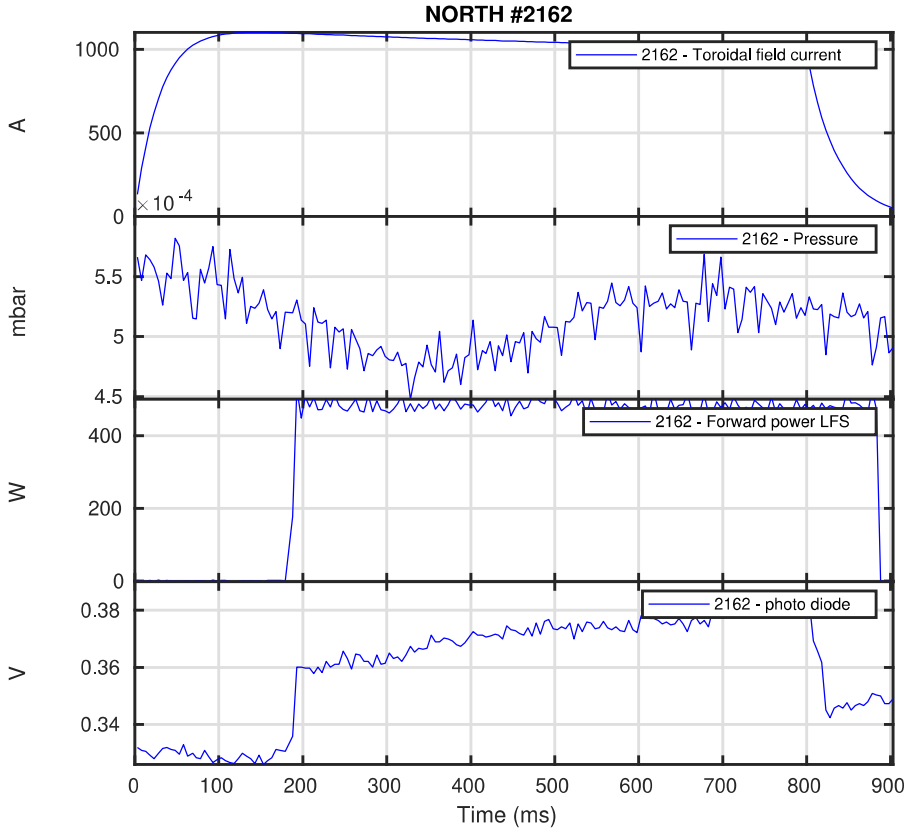

Figure 6.3: Control diagnostic output for shot 2162. From top to bottom: Toroidal field current, vacuum vessel pressure, LFS heating power and photo-diode output.

The requested pressure for this shot, without the gas-correcting factor (section 5.1), was of 5×10^{-4} mbar and at t = 300 ms, when the pressure falls under the requested value, the gas valve is engaged to

puff additional fuel, with a subsequent increase in pressure. This gas puffing feature has been disabled during the PDI shots. It is also important to note how the plasma is not started at time t=0, as can be seen from the LFS power output and confirmed from the photo-diode. This is due to an intrinsic random delay of the magnetrons in the order of 100-300 ms. After start-up, the requested power level is reached in a few ms. To extract the information on the electron density and temperature from the Langmuir probe, each scan over the range [-30 V : 30 V] can be fitted using eq. (5.1) as shown in Fig. 6.4 and from the uncertainty in the fit parameters an error for both quantities can also be estimated.

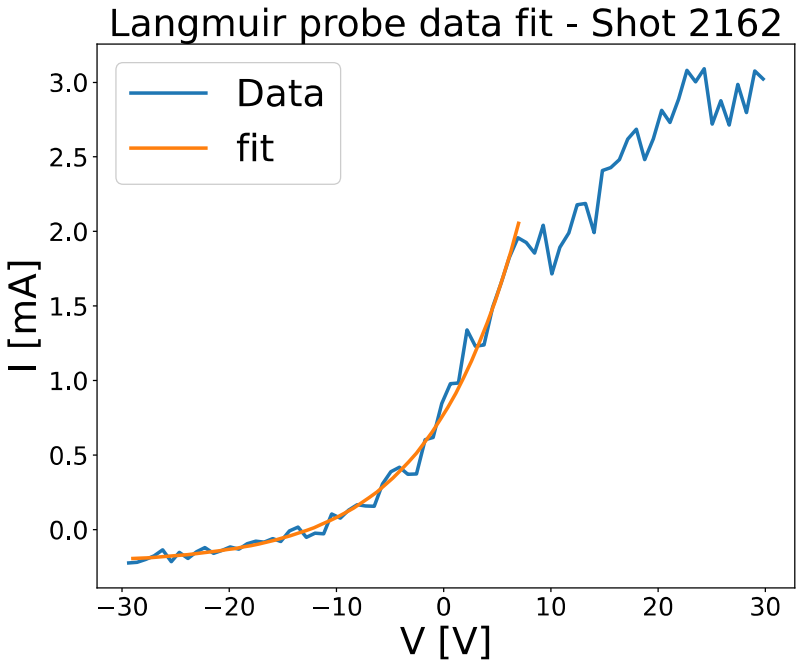

Figure 6.4: Example fit of Langmuir probe data

Putting together the information from the consecutive scans, the time evolution of the system can be determined. In Fig. 6.5 the electron density and temperature with the related uncertainties for the duration of example shot 2162 are shown.

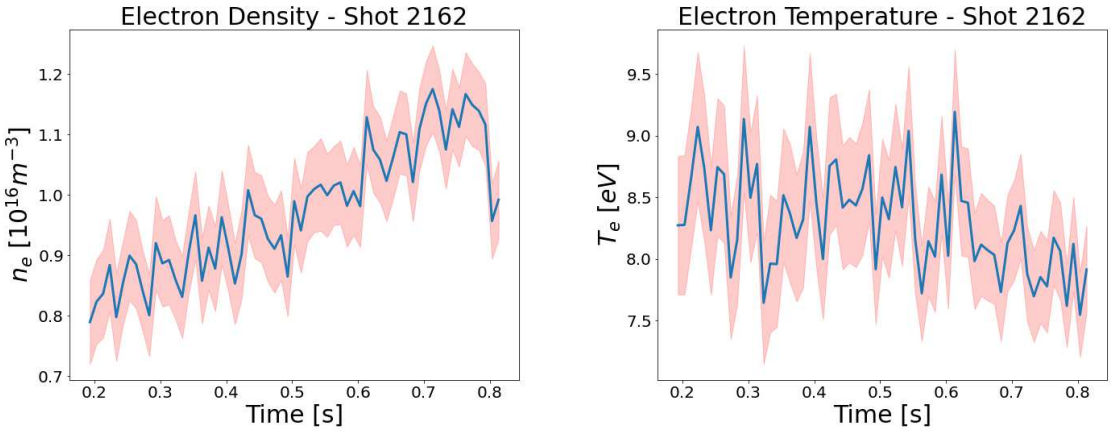

Figure 6.5: n_e and T_e time evolution during shot 2162. The red shaded area indicates covers ± one standard deviation.

The density increase is correlated with the light output increase visible in Fig. 6.3. The increase in density will lead to a shift in the position of the Upper Hybrid layer and from Fig. 3.15 this would lead to an expected shift in the frequency of the daughter waves of a couple of MHz during the shot. The temperature, instead, appears to be approximately constant during the shot. In Fig. 6.6 a scan

of the maximum n_e and T_e during shots with different nominal heating power is shown. The different curves represent shots using either only the LFS magnetron, only the HFS one or both the heating systems with equal power to each magnetron.

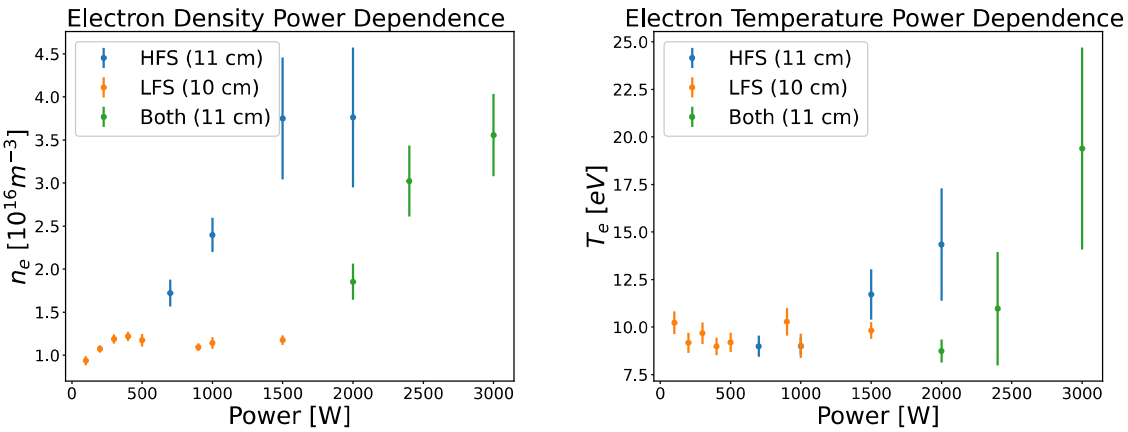

Figure 6.6: Lagmuir probe n_e and T_e heating power scan in He. Using the HFS higher n_e and T_e can be reached.

It appears that the LFS heating quickly saturates the density to the typical values of $n_e \approx 10^{16}\text{m}^{-3}$ and $T_e \approx 10$ eV while the HFS is able to reach higher densities and temperatures. The reason for this has not been investigated further but a reasonable explanation would be that in the absence of the O-X and O-X-B conversion mechanisms the steady-state conditions are reached at higher densities and temperatures as the heating is more efficient. When both heating systems are used at the same time, the final n_e and T_e reached appear to be comparable with the ones reached by the HFS alone, suggesting once again that the power from the LFS is lost through other means than absorption in the plasma.

A radial scan was performed for helium using the LFS heating system and for hydrogen using either LFS or HFS heating to determine the radial profile of T_e and n_e. For each shot, only one of the two heating systems was used and the power was kept constant at 900 W. The resulting profiles are shown in Fig. 6.7 where the distance is measured from the Langmuir probe manipulator. The maximum distance from the manipulator corresponds to a probe tip location ≈ 3 cm from the wall.

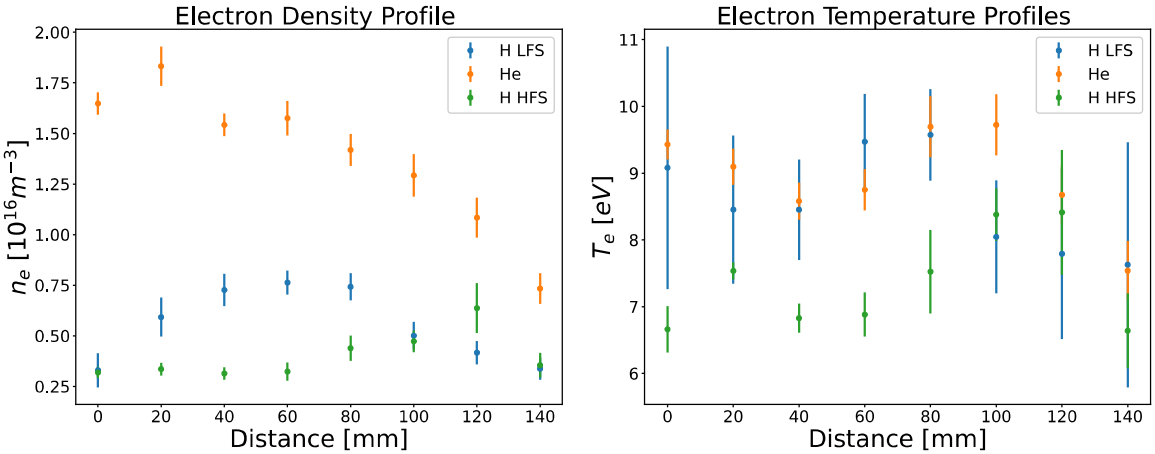

Figure 6.7: Radial density and temperature profiles for He and H. The temperature profiles have roughly constant temperature while the density profiles show peaks in different positions depending on operating gas and type of heating used.

The density profiles appear significantly different in the different cases. In the case of helium it appears that the density is peaked on the outer side while for hydrogen the density peak is towards the center. As the central solenoid has not been used to allow for longer shots, the plasma is not

completely confined as it lacks the radial drift averaging that is vital in increasing the confinement times in tokamaks. These radial drifts lead to a density peaked toward higher radii and that decays towards the HFS. The reason leading instead to the peaked profile in hydrogen is not well understood but it may be related to some current drive that generates partial confinement. When heating from the HFS the density peak appears to be more shifted toward the HFS itself even though the electron cyclotron resonance and the upper hybrid resonance are expected roughly in the core of the plasma where the hydrogen density peak when heating from the LFS can be found. This may be due to the X waves being reflected as electron Bernstein waves by the upper hybrid layer when coming from the HFS but further studies would be needed to prove it. The most relevant feature is that the density profiles are not sharply peaked, as it could be expected from operating the tokamak without the central solenoid, leading to the inhomogeneity of the magnetic field begin the driving inhomogeneity in bringing the threshold for the parametric decay up to 100's of W. The difference in absolute values for the three density profiles is due to different gas pressures in the different campaigns and holds no intrinsic meaning. The temperature profiles appear flat overall and with no significant change when using hydrogen instead of helium. When heating from the HFS T_e appears to be generally lower but with a more peaked profile in the same inner region as the n_e peak. In general, the value of T_e can be considered approximately spatially constant and the initial estimate used in chapter 2 of $T_e \approx 10$ eV appears reasonable.
The validity of a set of density and temperature measurements when predicting the behaviour of the system in subsequent shots operating in the same nominal conditions could be questioned. In order for the radial profiles and power scans to be informative on the behaviour of the tokamak, they must be repeatable. To this end in Fig. 6.8 shot 2183 and shot 2185, both with the same nominal conditions, are compared.

The radial profiles are mostly compatible, within experimental error $T_e \approx \pm 1eV$ and $n_e \approx 0.1 \times 10^{16}\mathrm{m}^{-3}$. The main discrepancy comes from the random delay intrinsic of the power system and the background gas pressure that is being driven by a puffing system periodically activated which leads to slightly different pressures if the shots are started at different times between one puff and the next.

6.3 Helium Operation

Shots at different power using the HFS and the LFS have been performed in helium. According to the results in chapter 3 the HFS has always been operated above threshold. However, even if the threshold is reached and the instability is triggered, this does not mean that the daughter waves can be measured as the amplitude of the fraction of the EBW that is not absorbed by the plasma and is able to escape may be too small to be measured, in particular when compared to the nearby pump wave which acts as a source of background. Before looking for PDI's it is necessary to identify the different peaks in the spectrum, which can be done by comparing shots in different conditions. The shots in this section have always been performed at the nominal neutral pressure of $8 \cdot 10^{-4}$ mbar that corresponds to $4.7 \cdot 10^{-3}$ mbar in He. Starting from the LFS, an example of a shot at the low power of 200 W is shown in Fig. 6.9 while a shot with the higher power of 1500 W in Fig. 6.10

As mentioned in section 6.1 the spectrum is significantly cleaner at higher powers and so its use has been preferred for the successive studies even if in principle not required to see the decay according to the prediction in chapter 3. The peaks at 2.47 GHz and 2.525 GHz likely come from the mixing of the 2.5 GHz signal with the pump wave. A peak can be seen in the 1500 W HFS shot at 2.494 GHz. Such a peak is commonly present and attributed to the mixing of the 2.5 GHz signal with signals that after being mixed-down are of a few MHz. The advantage of using the LFS is that the measured value of the frequency is much closer to the nominal one of 2.45 GHz than in the HFS case at higher powers. For example, considering the 1500 W case, the lack of the additional peak coming from the mixing of the pump wave with the 2.5 GHz signal makes the spectrum much cleaner. The peak of 2.433 GHz is at ≈ 18 MHz from the main peak and is perfectly in line with PDI predictions but is a signal always present at the same frequency and so unrelated to the EBW waves that are expected to drift in power following the pump wave. Using higher powers should increase the height of a possible PDI peak, but it would also shift the main peak away from the 2.45 GHz mark and so lead to the generation of a

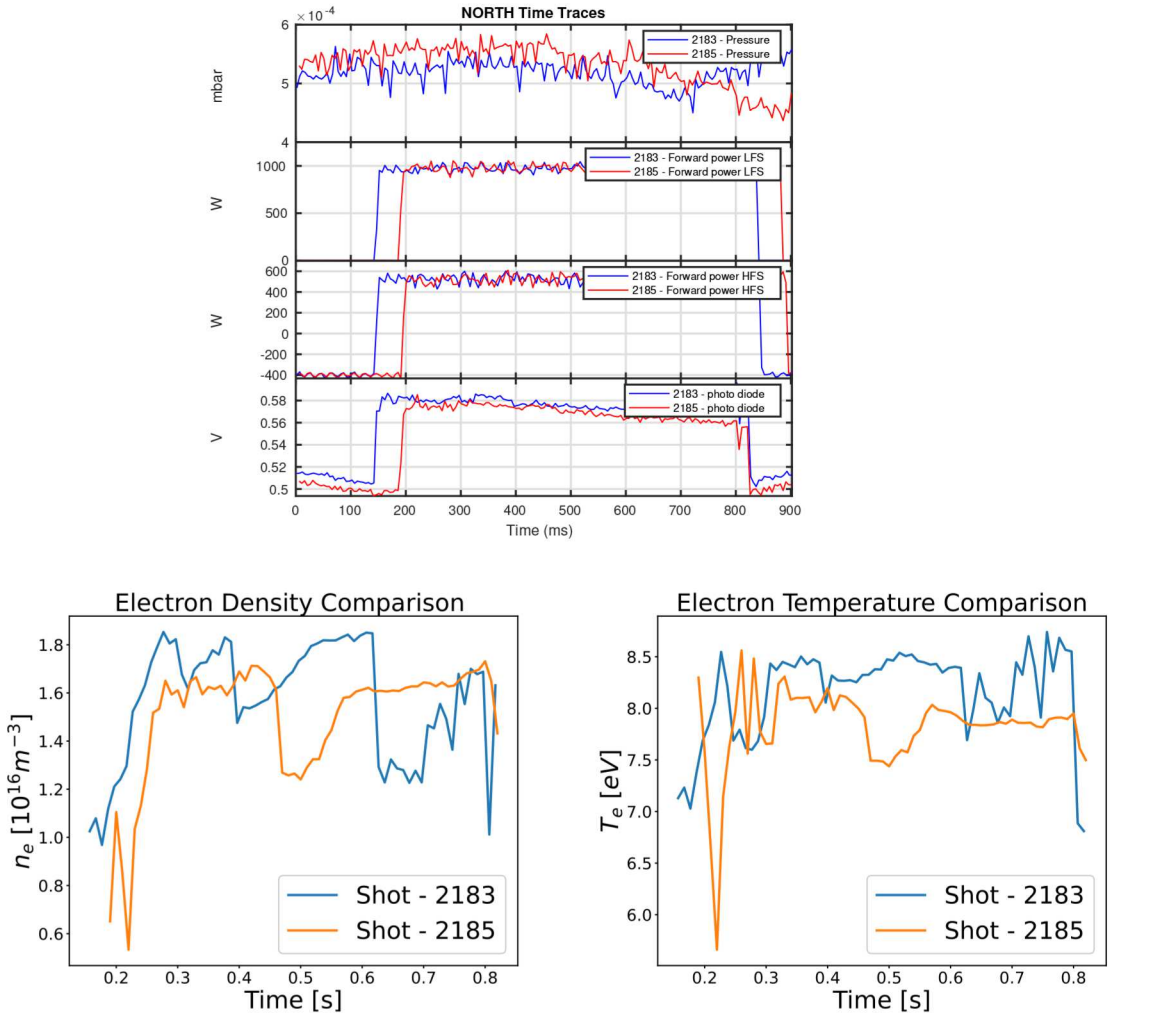

Figure 6.8: Radial density and temperature profiles comparison for shot 2183 and 2185.

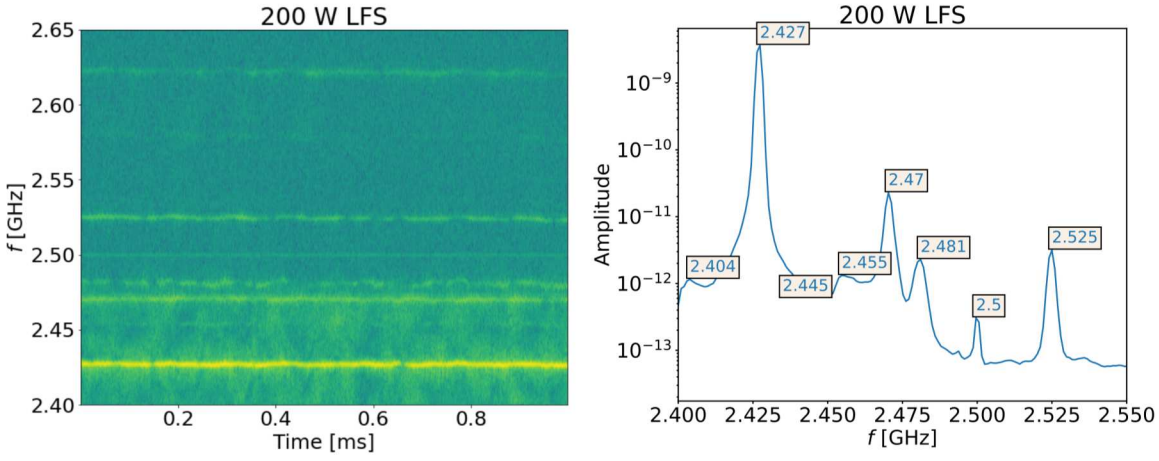

Figure 6.9: Shot with 200 W of LFS heating. At very low powers the magnetron spectrum is not clean and produced additional peaks.

secondary peak from the mixing with the 2.5 GHz signal, which would be mirrored around 2.45 GHz and would end up covering the signal of interest. Moving instead to the HFS magnetron, from the comparison of a shot with 1200 W of heating power injected from the HFS into an empty vessel or into a plasma, shown in Fig. 6.11, it is clear that no additional peaks are present in the case with plasma that could be related to PDI's as they are probably covered by the mixing peak at 2.446 GHz.

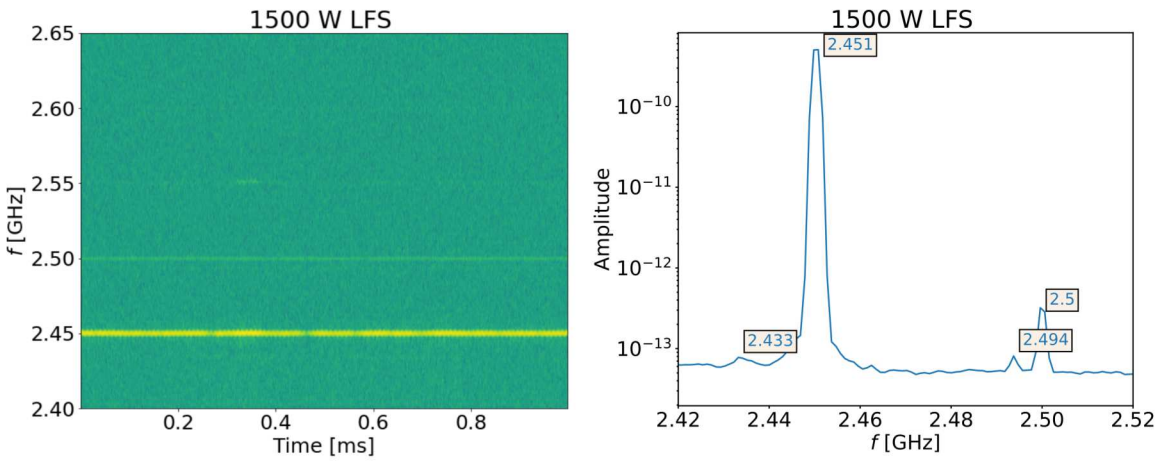

Figure 6.10: Shot with 1500 W of LFS heating. At higher powers the magnetron spectrum becomes cleaner.

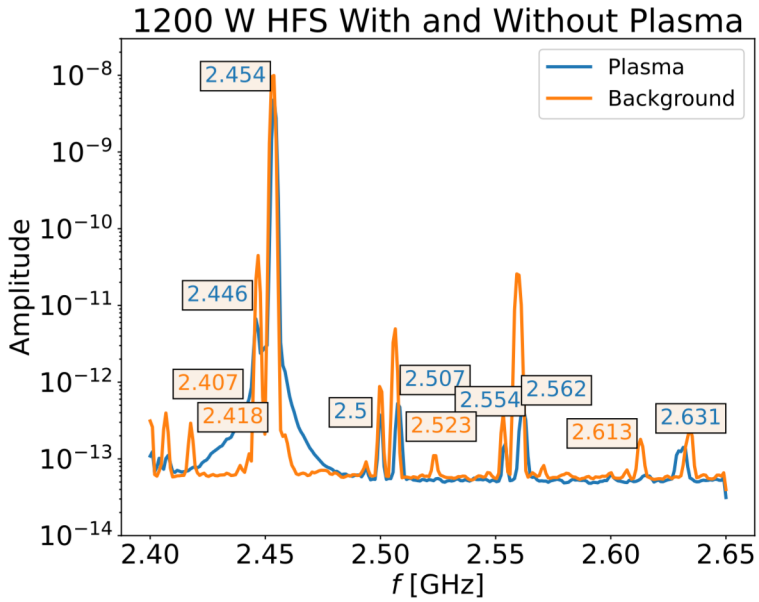

Figure 6.11: Comparison of shot with 1200 W of HFS heating power to the background taken by launching the microwaves in the empty vessel. The presence of a plasma widens the pump peaks.

It can also be noticed that the amplitude is generally lower when a plasma is present as it absorbs part of the heating power and that when a plasma is present the two main lines, due to the heating system at 2.454 GHz and its mixing with the 2.5 GHz line, are less sharply peaked. As usual, the harmonics of the mixed-down signal of the heating system can also be seen at 2.507 GHz and 2.462 GHz. The spectrum without plasma shows some additional low-intensity lines but these are absorbed by the plasma and they are not usually visible. An oscillation in the HFS pump with a frequency of $\approx$ 10 kHz is also present and can be seen for example for a 2000 W HFS shot in Fig. 6.12. The origin of this oscillation is not known but it is supposed to be intrinsic of the magnetron. A possible hypothesis related to the mechanical vibrations of the system generated by the turbomolecular pump was tested by performing some shots with the pump off but the oscillations were still measured. In Fig. 6.13 two shots with the same amount of heating power using either the HFS or LFS launcher are shown. It can be seen that the signal strength is lower when using the LFS with respect to the HFS and this leads to only the strongest lines being visible. It can also be seen that the HFS uses slightly higher frequencies and this has been confirmed over all the operative region through a power scan for both HFS and LFS shown in Fig. 6.14, where the power scan into an empty vessel is also reported for comparison.

As it could be expected, the plasma does not have a significant effect on the frequency of the HFS

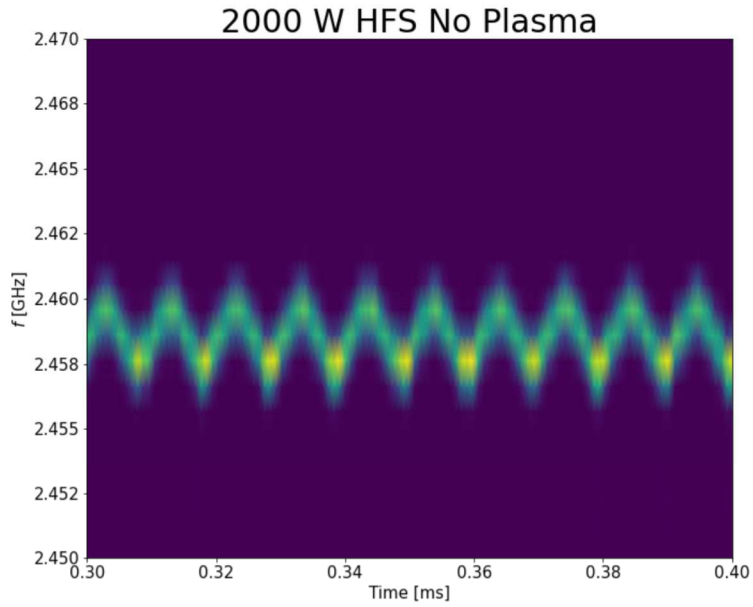

Figure 6.12: Oscillation of HFS pump frequency with no plasma.

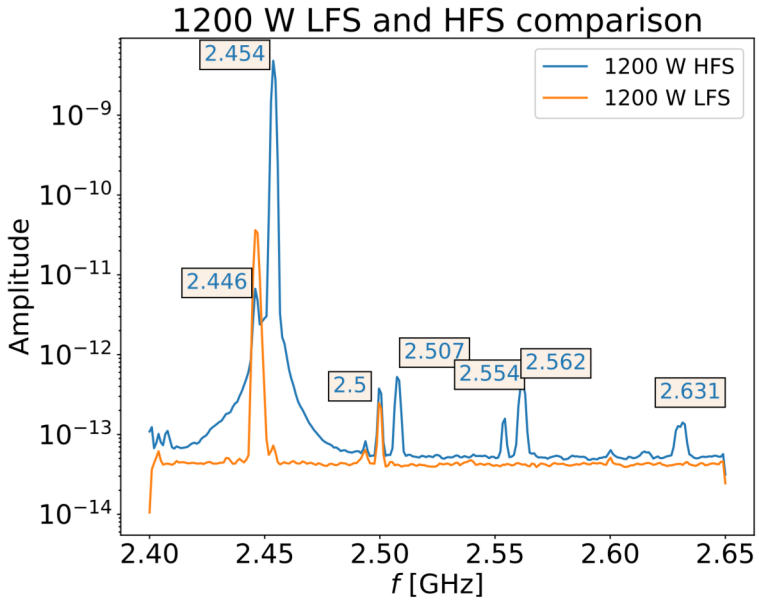

Figure 6.13: Comparison of shots with 1200 W from either the LFS or HFS. The presence of a peak in the HFS case at 2.446 GHz comes from the mixing with the 2.5 GHz signal.

heating. The frequency of the LFS system is consistently 5-10 MHz lower than the HFS one and this places the LFS peak near where the down-shifted high-frequency wave would be expected. This complicates the measurement further when trying to use both heating systems at the same time and suggests that switching to hydrogen is required to measure the decay. It is also worth noting that the frequency drift is significantly larger for the LFS and this may affect the design of an improved version of the radiometer that uses a notch filter instead of the attenuators. Unfortunately, the power that leads to a pump frequency of 2.45 GHz for the HFS magnetron, useful to reduce the number of lines in the spectrum, is of only $\approx$ 700 W, far from the maximum power reachable by the system. A spectrum taken with 700 W of HFS power is shown in Fig. 6.15.

While the main peak is asymmetrical in the region of interest, meaning that a signal may be present there, the measurement is non-conclusive. Spectra taken at many different powers using either the LFS or the HFS magnetron are compared in Fig.6.16

The drift of the peak centroid with frequency can be seen in both cases as well as the reduction

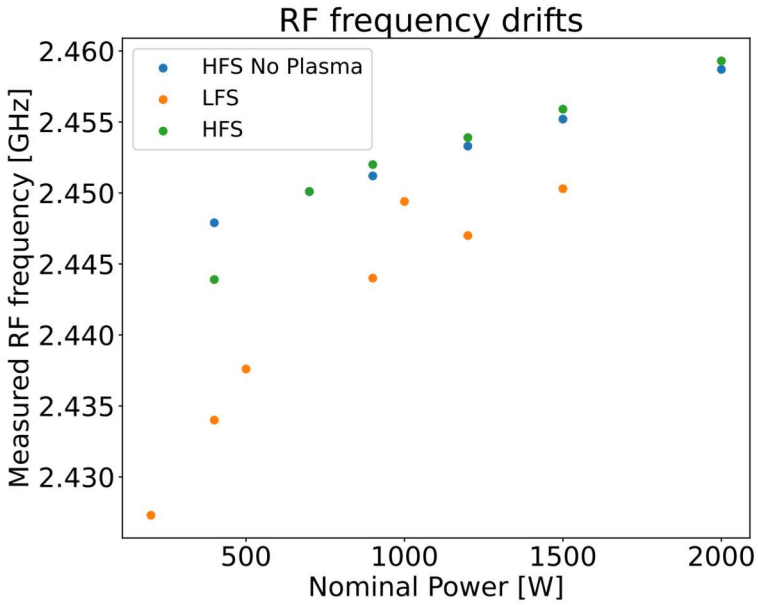

Figure 6.14: Frequency drift with power for HFS and LFS magnetron in a helium plasma. The frequency drift for the empty vessel is also reported

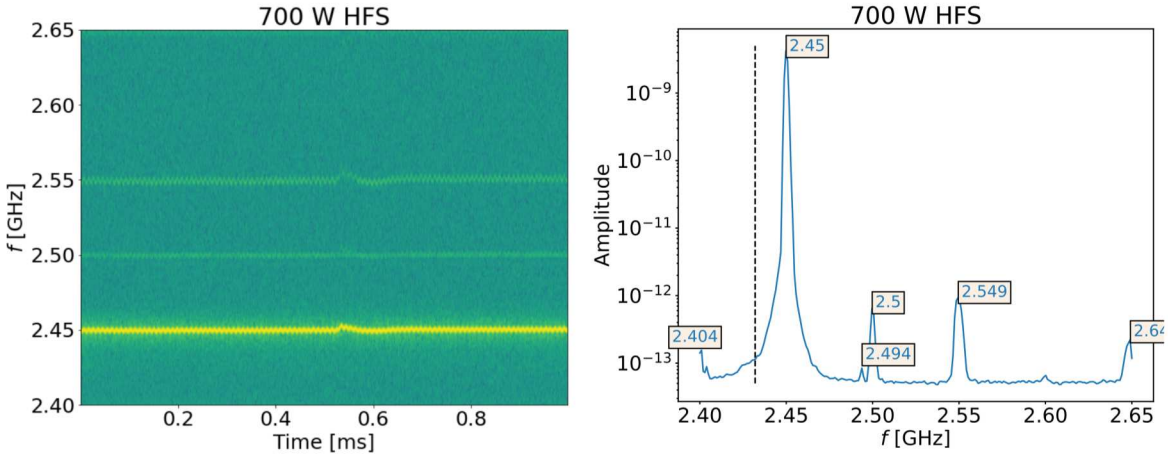

Figure 6.15: Shot with 700 W of HFS heating. The black dotted line represent where a peak at 2.33 GHz would be expected

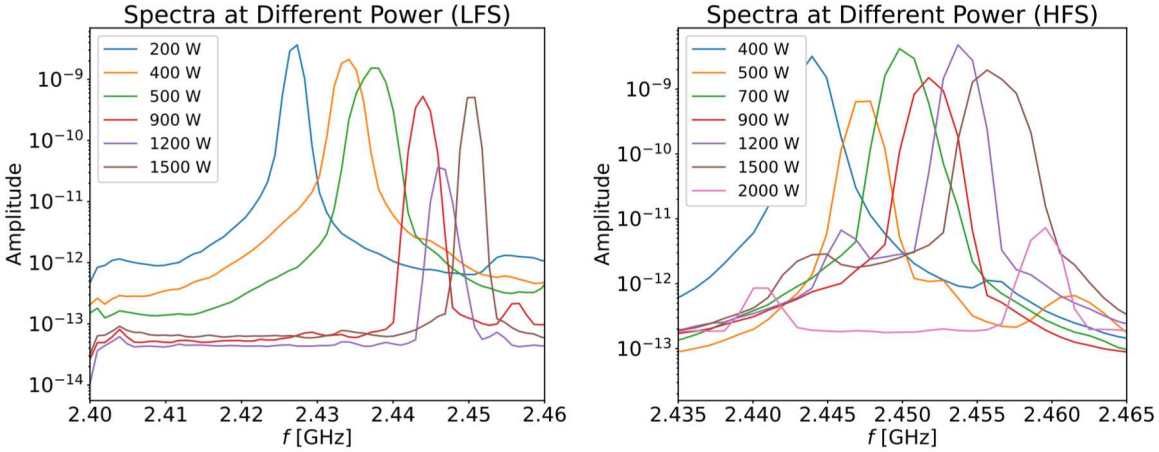

Figure 6.16: Specrtum evolution with heating power using either only the LFS (left) or only the HFS(right). The additional peaks to the left of the main peak in the HFS case are due to mixing effects and not to PDI's.

in background and more sharp peaks typical of high-power regimes. In the LFS case, no additional peaks to the left of the main peak are present. This is not obvious a priori as for high enough power the fraction of O waves converted to X waves could be high enough to trigger the instability in a similar way to what was observed on ASDEX, but it does not appear to be the case on NORTH at the reported power levels. When using the HFS at high enough power $P_{HFS} \geq 1200W$ an additional peak emerges to the left of the main peak. The frequencies of this peak are comparable to what would be expected from the down-shifted high-frequency daughter waves but they are generated from the mixing with the 2.5 GHz signal from the VCO and completely cover the region where the decay would be expected. No additional peak could be identified as coming from a PDI process. The fact that these peaks are not originated from the PDI process can also be seen by centering the spectra at different powers in the same position, as done in Fig. 6.17

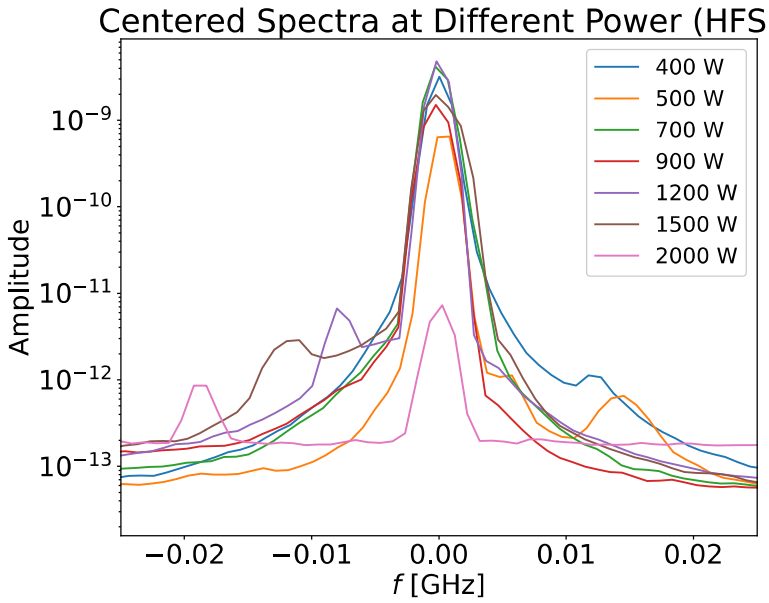

Figure 6.17: Frequency drift with power of mixed-down peak for HFS magnetron in a helium plasma. The frequency dift of the additional peak is too large to be explained by parametric decay.

The distance of the sub-peak from the main peak clearly increases with power while the daughter waves should be shifted of a value f_1 which is about constant. While it is true that at higher heating power corresponds a higher density, the measured n_e variations with power shown in Fig. 6.6 show a variation of a factor ≈2-3, that from Fig. 3.15 lead to an expected frequency variation of a $\approx 3-5MHz$, well below the shift of the mixing sub-peak of 20 MHz. It could be argued that using only the HFS magnetron is not consistent with the treatment performed in chapter 3, as the assumption is to be injecting waves into a plasma with a certain density while using only the HFS means injecting waves into a neutral gas. This means that until the plasma is fully formed the model is not completely representative of the system. To this end, some shots were performed where the plasma was initially formed with the LFS launcher and only then X waves were injected. In Fig. 6.18 a shot with 900 W from both HFS and LFS is shown.

The two main peaks for the two magnetrons are present as well as the signal at 2.45 GHz and its mixing with a 6MHz signal. It can be seen how the LFS pump wave is ≈ 7 MHz to the left of the main peak and covers the region where a signal from PDIs could be expected. No additional peak that could be attributed to parametric decay is visible. During the measurement campaign in helium it was not possible to have both heating systems on and an HFS power greater than 1500 W. In Fig. 6.19 the shot with the maximum allowed power on the HFS is shown. At these HFS power levels, the peak related to PDI's still does not appear visible. To increase the amplitude of the daughter waves the possibilities are to increase the heating power, increase the plasma density by increasing the neutral gas pressure or decreasing the attenuation of the signal. To distinguish the peak more easily from the background, switching to a hydrogen plasma is preferable. All of these possibilities are realized in the

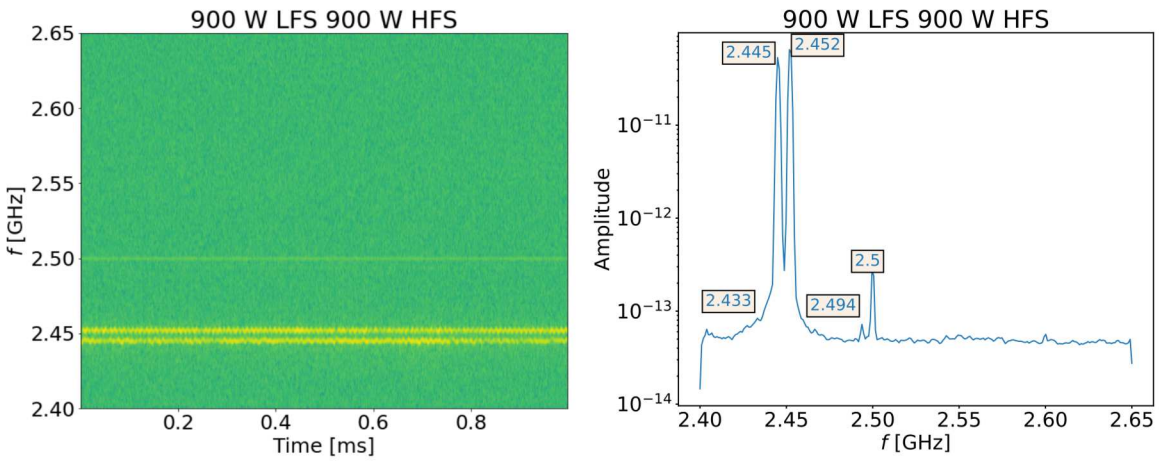

Figure 6.18: Shot with 900 W of both HFS and LFS heating

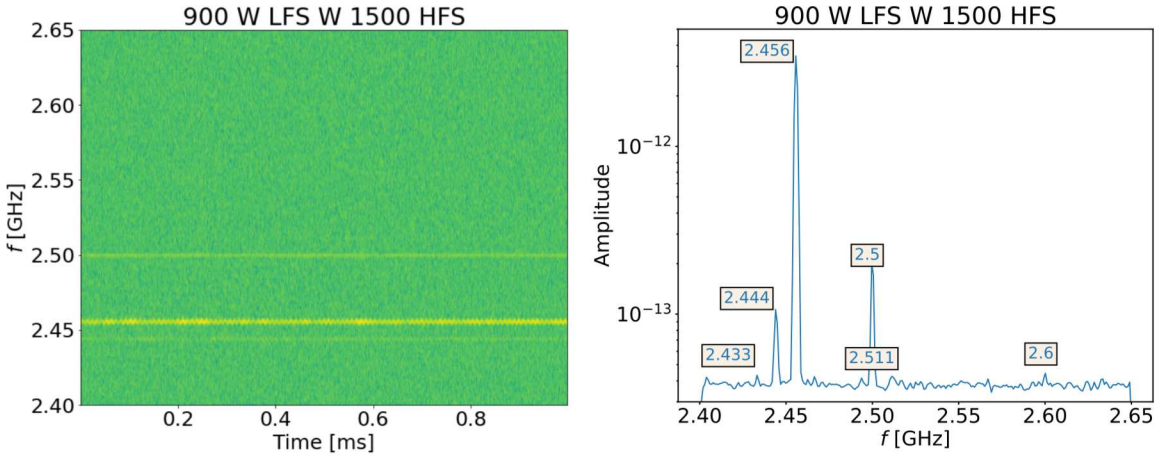

Figure 6.19: Shot with 1500 W of HFS and 900 W of LFS heating

next section, describing the experiments in hydrogen.

6.4 Hydrogen Operation

After changing the operating gas to hydrogen and reducing the signal attenuation on the radiometer, a similar measurement to Fig. 6.19 was performed. The shot, having 1500 W of HFS power and 900 W of LFS power with the same nominal pressure of $8 \cdot 10^{-4}$ mbar, is compared in Fig. 6.20 with shots using either HFS or LFS heating.

It can be noticed that the amplitude of the signal is much higher and that additional peaks are visible, but these can all be related to signals that are also visible without plasma and so cannot be generated by parametric decays. It is clear how the region to the left of the HFS pump wave is full of additional signals that cover the one of interest. Both pump waves, at 2.455 GHz for the HFS and 2.445 for the LFS, are surrounded by the subpeaks at $\approx \pm 4MHz$. These peaks may be related to the parametric decay into IBW mentioned in chapter 4 but they may also be unrelated. In this case, the mixing of the HFS peak with the 2.45 GHz one happens to give a signal at the same frequency of the LFS heating system but this is, in general, a further confounding element. The peak at 2.469 GHz is symmetric to the 2.441 GHz one with respect to the HFS pump at 2.455 GHz and the frequency difference between the two is of 14 MHz. It could be due to a combined mixing involving the 4 MHz peak and the 10 MHz of difference between the LFS and HFS heating frequencies. In Fig. 6.21 the spectra corresponding to two shots at the maximum HFS heating power of 3000 W and 900 W of LFS at different pressures are compared with a shot using LFS heating and a shot using HFS heating into the vacuum vessel. The reasons for using a shot for the HFS performed without a plasma are that

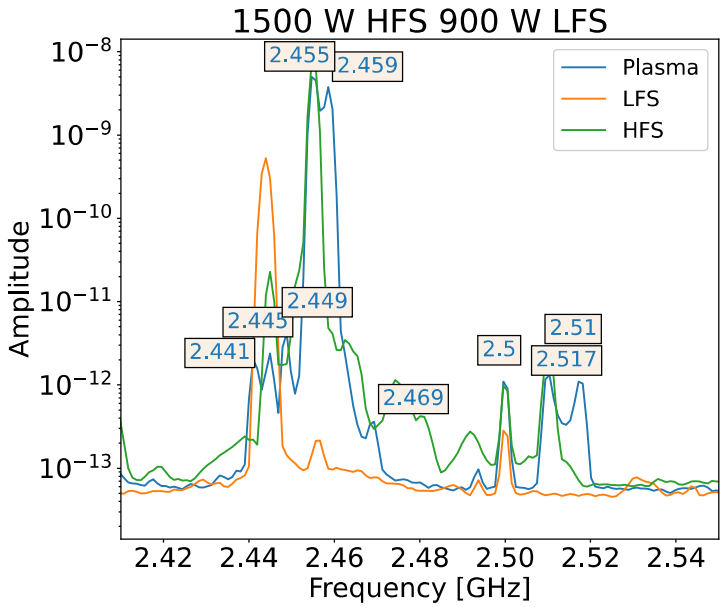

Figure 6.20: Shot with 1500 W of HFS and 900 W of LFS heating power compared with shots with only HFS or LFS heating. The peaks to the left of the main peak are due to the LFS pump and the mixing of other peaks in the mixer.

it allows recognizing immediately peaks that cannot be coming from PDI's and that it shows small peaks that may be absorbed when a plasma is present and only the HFS is used but they are still signals not related to the decay of interest.

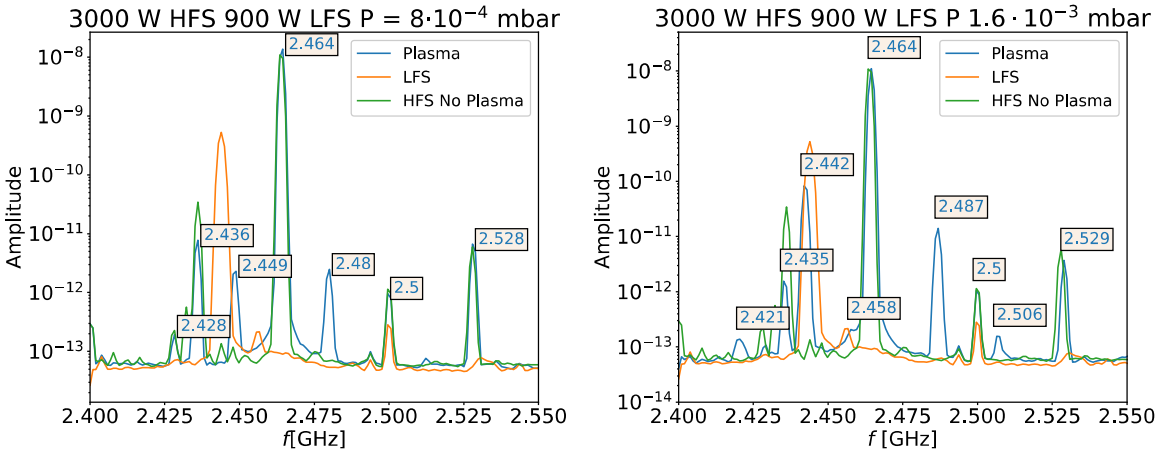

Figure 6.21: Shot with 900 W of LFS and 3000 W of HFS heating at nominal pressures of $8 \cdot 10^{-4}$ (left) and $1.6 \cdot 10^{-3}$ (right). They are compared to a shot using LFS heating and a shot using HFS heating into the vacuum vessel.

The main peak that can be noticed, at 2.464 GHz, comes from the HFS heating. The signal at 2.5 GHz and the peak at 2.436 GHz coming from the mixing with the pump wave are present in both cases. The harmonic of the pump wave signal is also present at 2.528 GHz in both cases. The 2.428 GHz, could be related to the mixing of the second harmonic of the mixed-down pump wave with the 2.5 GHz signal or to the mixing between the pump and the 2.436 GHz, that already comes out of the mixing of two signals. It is also possible that it is due to the mixing of the 2.436 GHz signal with the 8 MHz one that also generates the peak at 2.292 GHz. In the $1.6 \cdot 10^{-3}$ case, the height of the 2.428 GHz peak seems strongly reduced while the signals at 2.5 GHz and 2.529 GHz have comparable strength which seems to exclude the first possibility considered. In the low pressure shot the LFS heating frequency is shifted towards higher frequencies with respect to the case using only the LFS system, at 2.449 GHz instead of 2.445 GHz. The origin of this shift is not known and it is not visible

in the 1500 W shot or in the high-pressure one. At 2.48 GHz a symmetric peak to the LFS heating one with respect to the HFS pump wave can be noticed, with a similar amplitude to the LFS pump one. The presence of a symmetric peak to the LFS heating one will be present in many subsequent shots. Its origin comes from higher-order mixing in the radiometer and it is not related to the physics of the problem. Furthermore, it is located at higher frequencies with respect to the HFS pump wave and so far from the region of interest. In the high-pressure case, a few more peaks can be seen. The 2.5 GHz signal is mixed with a 6 MHz signal to generate the two neighbouring peaks and similarly the 2.458 GHz peak is one of the two peaks coming from the mixing of the 2.464 one, with the other not being visible. The signal at 2.421 GHz comes from the mixing of the LFS and HFS pump waves at 2.442 and 2.464 GHz respectively. Shots with the same heating power but at different pressures are compared in the same plot in Fig. 6.22

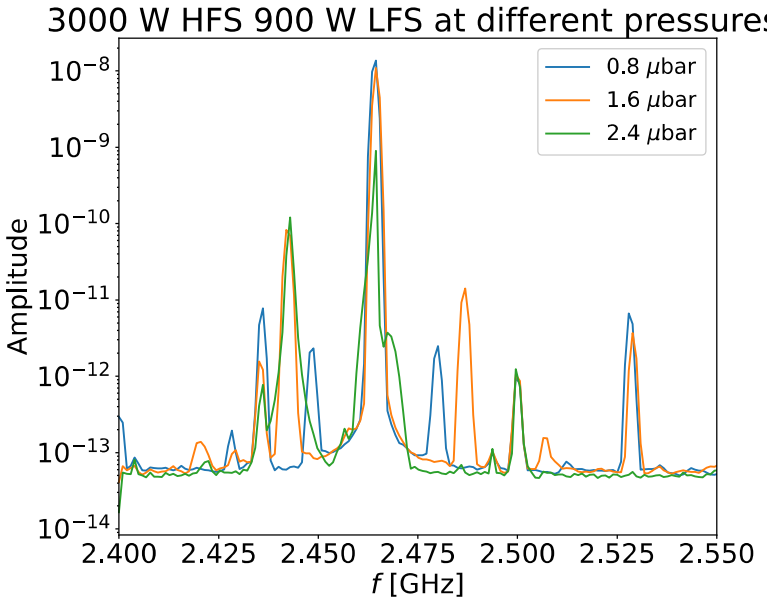

Figure 6.22: Shots with 3000 W of HFS and 900 W of LFS heating power at different pressures.

It is then clear that even at the highest pressure values attainable with the system, no unaccounted-for peaks appear in the spectrum. It is interesting to note that for the highest pressure the symmetric peak to the LFS pump wave does not appear but the reason for this behaviour is not clear. The presence of the mixing peaks does not allow to determine the presence of eventual daughter waves and additional measures must be taken to reduce the measured background.

6.4.1 Low LO Frequency Operation

To clean the spectrum further, it is possible to lower the frequency of the LO as to increase the frequency of the mixed down signal from 50 MHz to a few hundred Hertz, so that the mixing peaks between the known signals will appear at lower frequencies and will avoid overlapping with the region of interest. This will increase the bandwidth required to see the entire spectrum, however, and will make the use of the Red Pitaya not possible in the current design for the radiometer. The next series of measurements were performed with a LO frequency of 2.3 GHz, which will correspond to a frequency of ≈ 150 MHz for the pump waves and of 200 MHz for the 2.5 GHz signal. A shot taken with 900 W of HFS and LFS power in these conditions is shown in Fig. 6.23

It can be noticed how in this case the mixing peaks related to the 2.5 GHz signal are shifted to lower frequencies, significantly clearing the region just to the left of the pump waves. Increasing the HFS power to the maximum allowed leads to the shot in Fig. 6.24

In addition to the HFS and LFS pump waves at 2.464 and 2.446 GHz, the signal at 2.5 GHz and the 2.336 GHz signal generated by the mixing of the 2.5 GHz and 2.464 GHz signal can be seen as always. The peak at 2.472 is generated by the mixing of the 2.464 GHz with the 2.308 GHz one. That the height of the 2.472 GHz peak is lower than the 2.308 GHz one would lead to the conclusion that

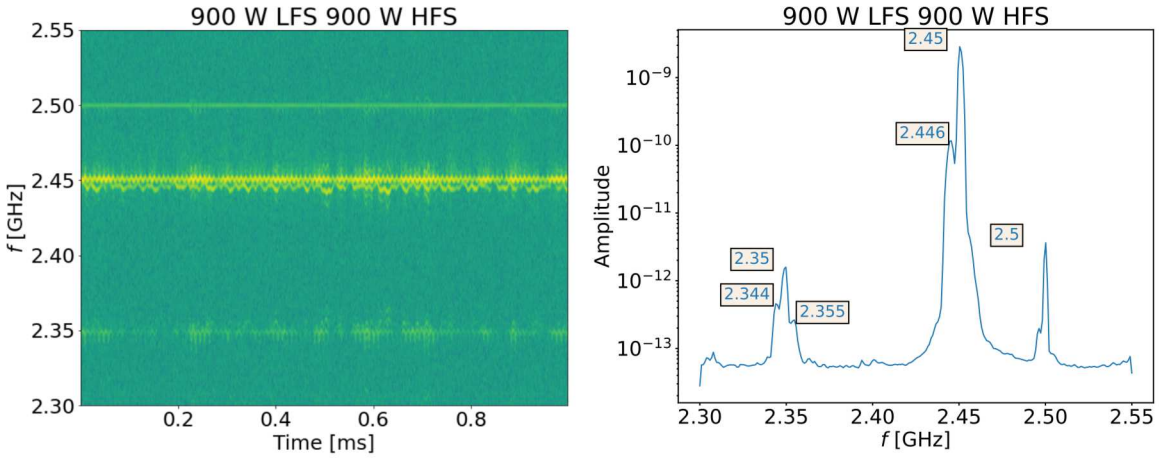

Figure 6.23: Shot with 900 W of LFS and HFS heating at the nominal pressure of $8 \cdot 10^{-4}$

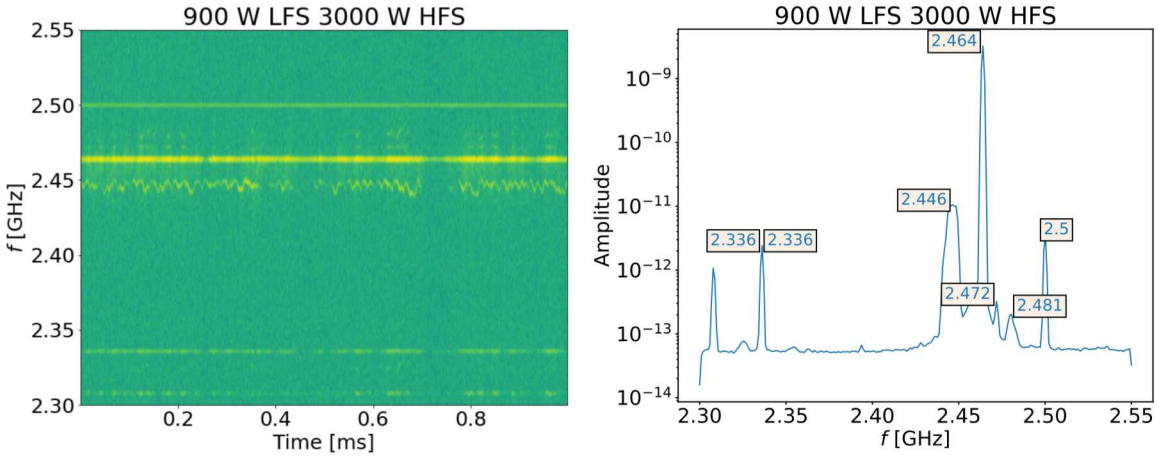

Figure 6.24: Shot with 900 W of LFS and 3000 W of HFS heating at the nominal pressure of $8 \cdot 10^{-4}$

these peaks at ≈ 8 MHz peaks cannot be due to decays into IBW, but the signal at 2.308 GHz could also be due to the sum of many contributions at 8 MHz from the decays into different branches but this seems unlikely. The peak at 2.481 is the symmetric of the LFS pump wave with respect to the HFS one. Increasing the pressure once again to $1.6 \cdot 10^{-3}$ mbar leads to the shot in Fig. 6.25

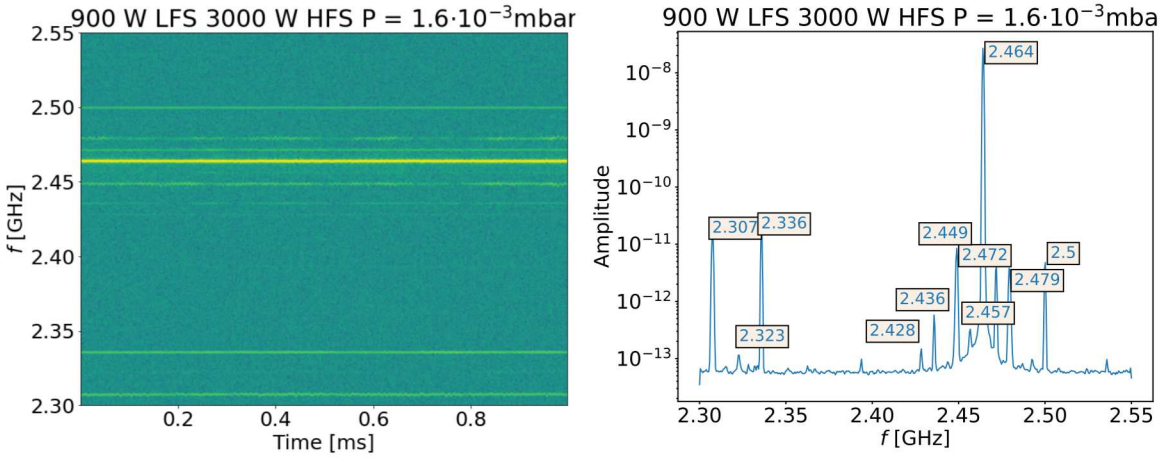

Figure 6.25: Shot with 900 W of LFS and 3000 W of HFS heating at the nominal pressure of $1.6 \cdot 10^{-3}$

In this case, the oscillations of the LFS heating frequency are much smaller and this leads to much sharper peaks. The HFS pump wave can be seen at 2.464 GHz along with the mixing with the 2.307

GHz signal, generating peaks at 2.457 and 2.472 GHz. The LFS pump wave and its symmetric peak can be seen at 2.449 and 2.479 GHz. The peak at 2.436 GHz, at a distance of ≈ 28 MHz from the pump wave, could be the EBW daughter wave or alternatively the second harmonic of some mixing between the HFS and LFS pump waves or from the recombination of the 2.472 GHz and 2.336 GHz peaks. The additional peak at 2.428 GHz is generated by the mixing of the 2.307 GHz and the 2.336 GHz peaks, which could also be interpreted as a successive parametric decay into IBW. To verify this a shot with only 3000 W of HFS power was performed for the two mentioned pressures and the spectra are shown in Fig. 6.26

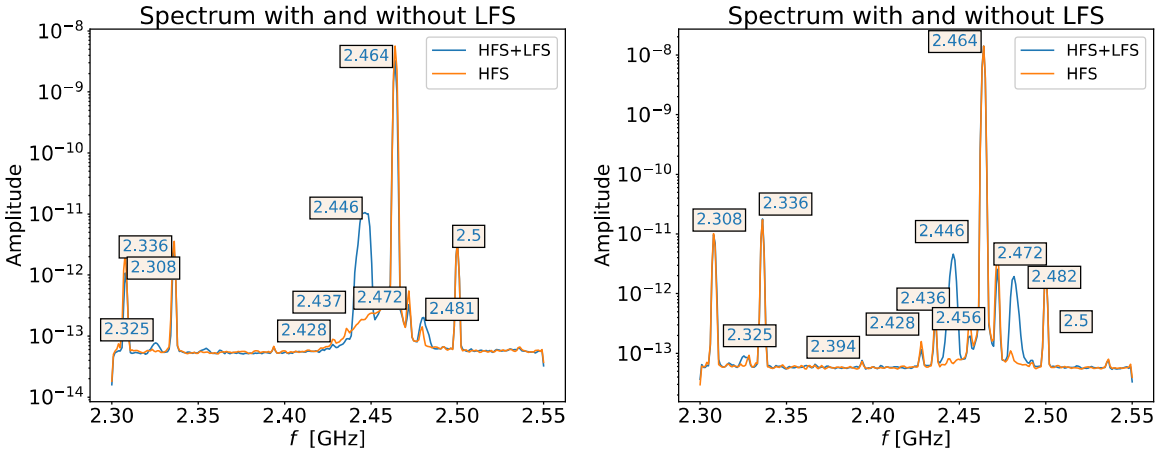

Figure 6.26: Shot with 3000 W of HFS heating at the nominal pressure of $0.8 \cdot 10^{-3}$ (left) and $1.6 \cdot 10^{-3}$ (right)

The only peaks missing from the two spectra are the LFS pump wave and its symmetric, suggesting that the remaining peaks are independent of the LFS heating. This, however, is not giving concluding proof of the distinction between a parametric decay into LH waves or just mixing of the 2.472 GHz and 2.336 GHz signals. It could be argued that if the peak at 2.436 GHz is the result of mixing, a peak at the sum of the frequencies would also be expected and it is not seen but it is still far from concluding evidence. Shots at different pressures are compared in Fig. 6.27

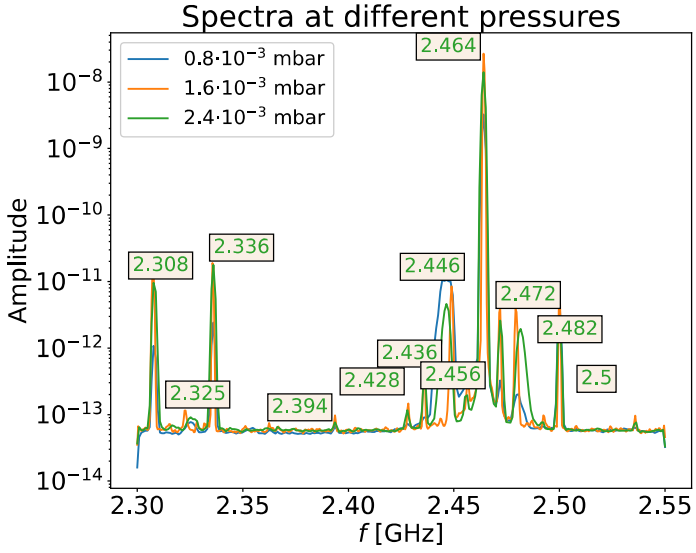

Figure 6.27: Shots with 3000 W of HFS and 900 W of LFS heating power at different pressures.

Once again no additional peaks can be seen while moving at higher pressure, where the daughter wave amplitude should be greater. Unfortunately, it was not possible to perform a shot with the same heating powers but without plasma, as in the absence of an absorbing medium the stray radiation in the room was too high and the security system automatically shut off the heating. A shot with the highest power injected without triggering the system, 900 W with both HFS and LFS heating is

shown in Fig. 6.28

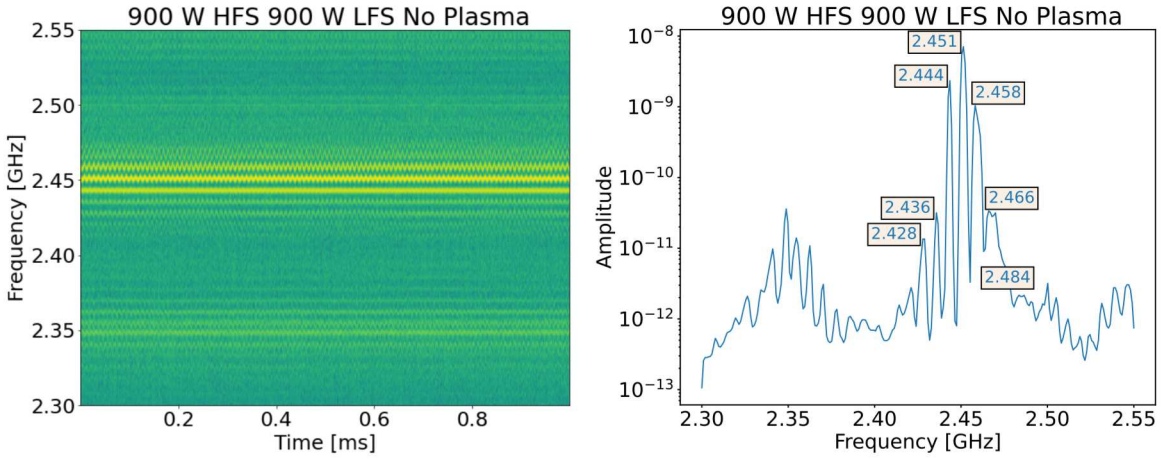

Figure 6.28: Shot with 900 W of LFS and HFS heating with no plasma. A large number of peaks created in the mixer and shifted by 7 MHz can be seen.

While the frequency of the HFS is lower due to the lower power, it is still evident that even at these lower powers the spectrum can very quickly be filled with harmonics that obscure the signal of interest. The presence of peaks at 2.436 and 2.428 GHz is not definitive proof of their origin unrelated to PDI's, as for these shot this frequencies happen to match a multiple of the frequency difference between the HFS and LFS pump wave. Another way to determine if a peak is due to PDI's is to compare spectra taken at different magnetic fields, as for lower and lower magnetic fields such a peak should vanish. This is done in Fig. 6.29, where the high-frequency and low-frequency ranges are shown separately to aid visualization.

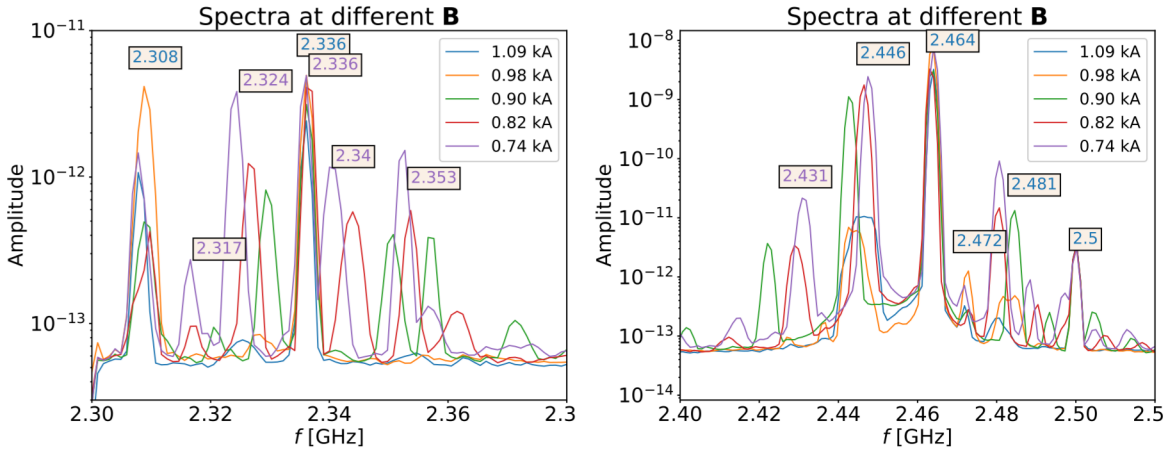

Figure 6.29: Shot with 900 W of LFS and 3000 W of HFS heating with different currents in the coils, proxy for different magnetic fields. High frequency range (left) and low frequency range (right)

The HFS pump wave and its mixing with the 2.5 GHz seem to be independent of the magnetic field both in frequency and amplitude while the LFS pump wave shows a higher amplitude with lower field. The signal at 2.308 GHz also seems to be independent of the magnetic field, which seems to exclude the possibility of decay into IBW. Consequently, the peaks coming from the mixing of the HFS pump wave and the 2.308 GHz signal and the relative harmonics appear roughly independent on the field. At lower frequencies, the spectrum becomes much more complex at lower fields, where the recombinations of different mixing peaks all become visible. As the strength of the 2.472 GHz and 2.336 GHz peaks does not seem too strongly dependent on the field, a possible dependence of the 2.436 GHz signal on **B** would be useful in ruling out one of the two possibilities, but due to the low strength of the signal, it is not possible to show with certainty its origin.

Chapter 7

High-Frequency Probe measurements of PDI

To look for the low-frequency daughter wave, it is possible to measure the oscillations of the floating potential on a Langmuir probe inserted in the plasma. Furthermore, using a probe designed to transmit high frequencies, the EBW waves can also be looked for using the probe, as they result in density oscillations that modify the floating potential. To this end, a high-frequency probe installed during the last experimental campaign for turbulence studies was used to look for the daughter waves of the parametric decay.

7.1 Measurements of EBW Daughter Waves

As for the radiometer, the lack of an acquisition system fast enough to sample the high frequencies lead to the use of the same electronic chain used for the radiometer but substituting the antenna with the signal coming from the probe. A series of measurements with different heating powers was performed but no clear indication of an additional line can be seen. Considering for example the shot with 900 W of LFS power and 2500 W of HFS power shown in Fig. 7.1, the two heating frequencies are present along with the peaks resulting from their mixing but no EBW wave can be discerned.

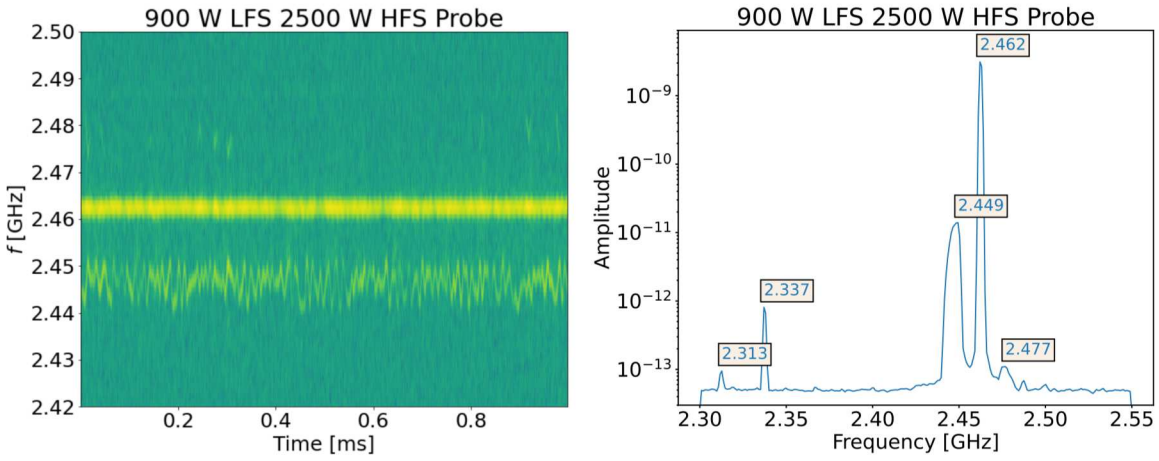

Figure 7.1: Floating potential measurement of high-frequency Langmuir probe of shot with 900 W of LFS and 2500 W of HFS heating

It is also interesting to note how the behaviour of the floating potential at the two frequencies is significantly different, probably due to the different powers involved. Trying to clear the spectrum from the LFS peak using only HFS heating at 3 kW results in a shoulder to the left of the peak, as shown in Fig. 7.2. To create a plasma the shot is started with 1 kW of heating power and then the power is increased to 3 kW for a short burst during which the measurement is taken.

The shoulder, however, is not really a distinguished peak and it is displaced from the pump wave

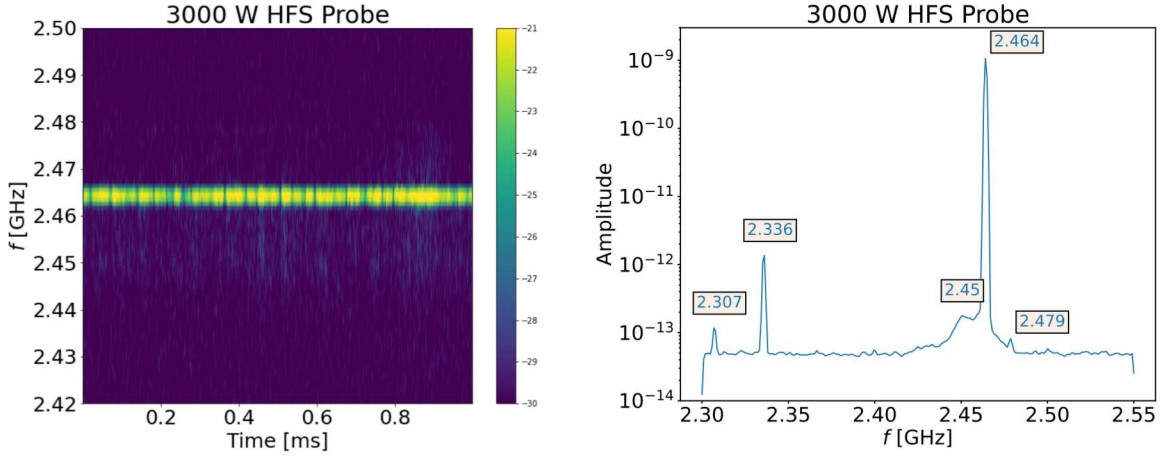

Figure 7.2: Floating potential measurement of high-frequency Langmuir probe of shot with 3 kW of HFS power

of only ≈ 15 MHz. It is worth noting that it is improbable that the shoulder is due to residual low-frequency radiation from the start-up period operating at lower powers. When in subsequent shots the start-up power was increased as to always have a frequency higher than 2.45 GHz, no visible effect on the shoulder frequency could be noticed. It was then concluded that the strength of the pump signal was too high to allow the measurement of the high-frequency daughter of interest without some kind of selecting dampening of the pump wave. This was achieved in the experiments on ASDEX through a notch filter, a component able to attenuate a specific band of frequencies. The only available notch filter for this work that could cover the band of interest covered a band of 100 MHz, from 2.4 to 2.5 GHz, thus also covering the region where the EBW was expected. A set of measurements was taken with the notch filter nonetheless, in the hope to measure higher-order decays, at frequency shifts multiples of the LH daughter frequency, and so out of the frequency region attenuated by the filter. By connecting the Langmuir probe to the notch filter, granting an attenuation of 40 dB in the 2.4 - 2.5 GHz range, and then to a 20 dB amplifier before the electronic chain developed for the radiometer, a large number of additional lines become visible. This can be seen for example the shot with 900 W of LFS and 3000 W of HFS heating power shown in Fig. 7.3

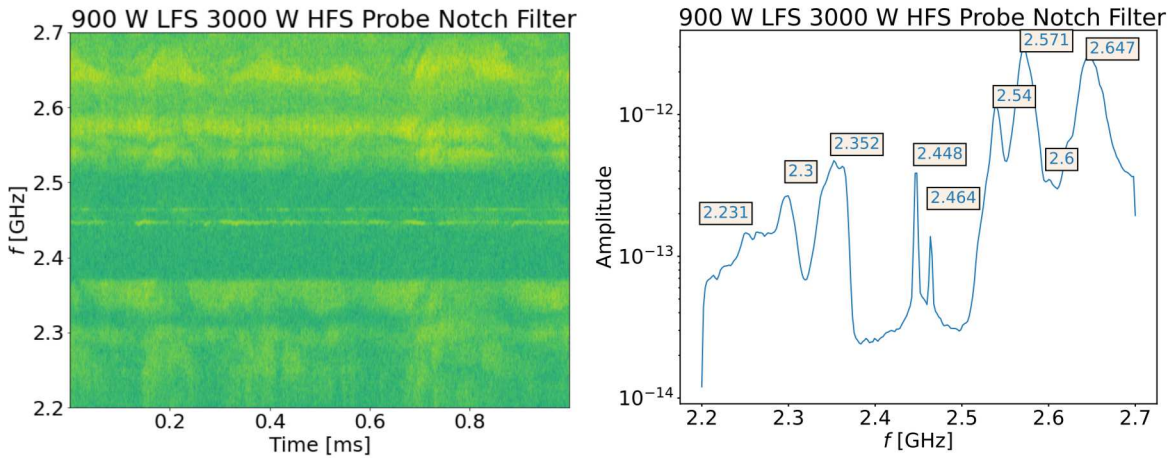

Figure 7.3: Floating potential measurement of high-frequency Langmuir probe using the notch filter. Focus on high frequencies.

In the center of the spectrum the region suppressed by the notch filter can be noticed, where the two pumps are still visible but at a strongly reduced amplitude. Out of the suppressed region, a number of broad peaks are visible but none of them are readily attributable to higher-order PDI's involving LH waves. No scaling with power of any of the peaks could be identified, which would be expected from PDI as using higher powers leads to higher densities, and so it appears that without a

notch filter covering a more narrow band it is not possible to measure the high-frequency daughter as the signal of the pump wave is too strong with respect to the one from the EBW daughter.

7.2 Measurements of LH Daughter Waves

Sampling the signal from the high-frequency probe after a low pass filter with a threshold frequency of 225 MHz allows measuring directly the low-frequency region of the spectrum, where the LH daughters are expected. Not requiring the mixer to lower the frequency of the signal also removes one of the main causes of background signals in the measurement, given by the mixing of multiple signals together. In Fig. 7.4 the low-frequency spectrum for the same shot in Fig. 7.3 is shown.

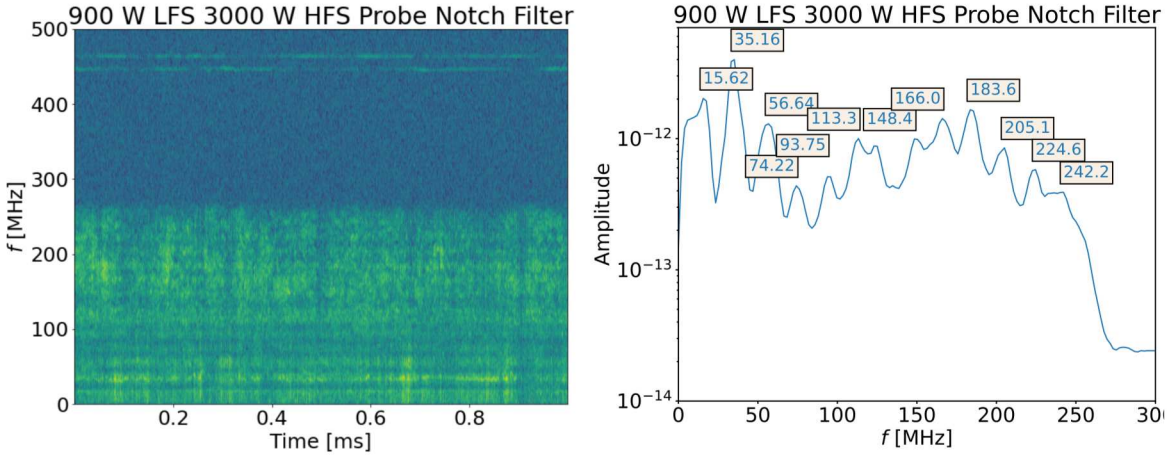

Figure 7.4: Floating potential measurement of high-frequency Langmuir probe using the notch filter. Focus on low frequencies.

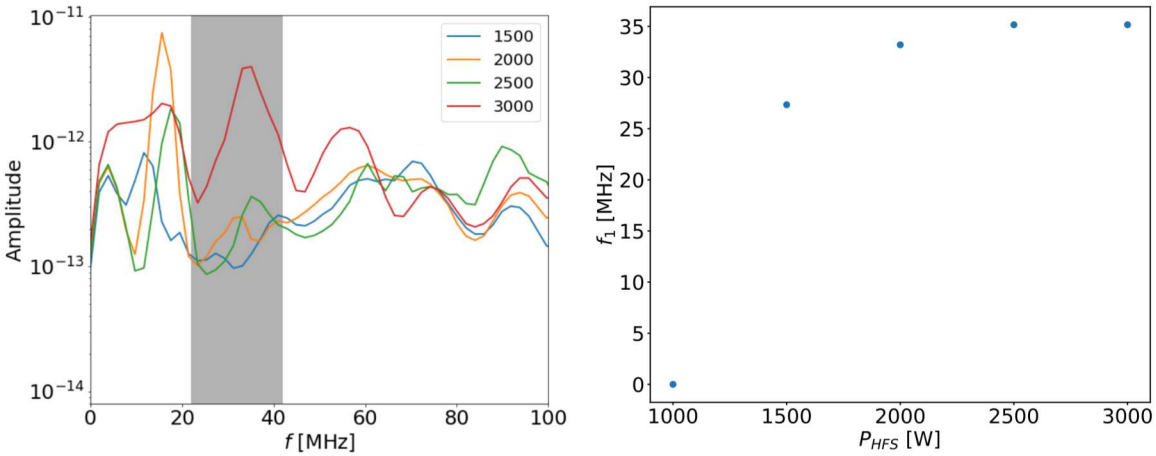

Figure 7.5: Floating potential measurement of high-frequency Langmuir probe using the notch filter. Focus on low frequencies. Spectra at 900 W LFS and varying HFS power (left) with the shaded region presenting the peak of interest and frequency dependence of the peak on HFS power (right). At 1 kW HFS power no peak at those frequencies could be distinguished.

Multiple peaks can be seen that cover the entire allowed band until the cutoff of the low pass filter. The peaks at lower frequencies appear in general more defined and the highest peak is found at the frequencies where the LH daughter is expected. The origin of the other peaks is not known for certain but they are also visible at low power. Multiple explanations could be possible, such as standing waves in the wires connecting the probe to the electronic chain, and studies to reduce the background in this region will be the topic of possible future studies. A set of measurements in different experimental conditions was performed to study the variation of the frequencies with the injected HFS power, the pressure and the magnetic field. A peak in the region of interest was not found for shots with 1 kW

of HFS power and 900 W of LFS power. Increasing the HFS power while keeping the LFS power at 900 W leads to the spectra in Fig. 7.5. In the shaded region, the peak that was identified as the LH daughter can be seen. It can be noticed how the frequency increases with power, as it would be expected by increasing the density of the plasma. The height of the peak also increases with power, both in absolute terms and when compared to the surrounding background peaks, as would be expected from PDI. It is important to note that neither of these effects is visible in the other peaks, which suggests that this peak is different from the others. Varying the magnetic field and the pressure also leads to a distinctive variation of the LH daughter frequency, shown in Fig. 7.6, that is not seen in the other peaks.

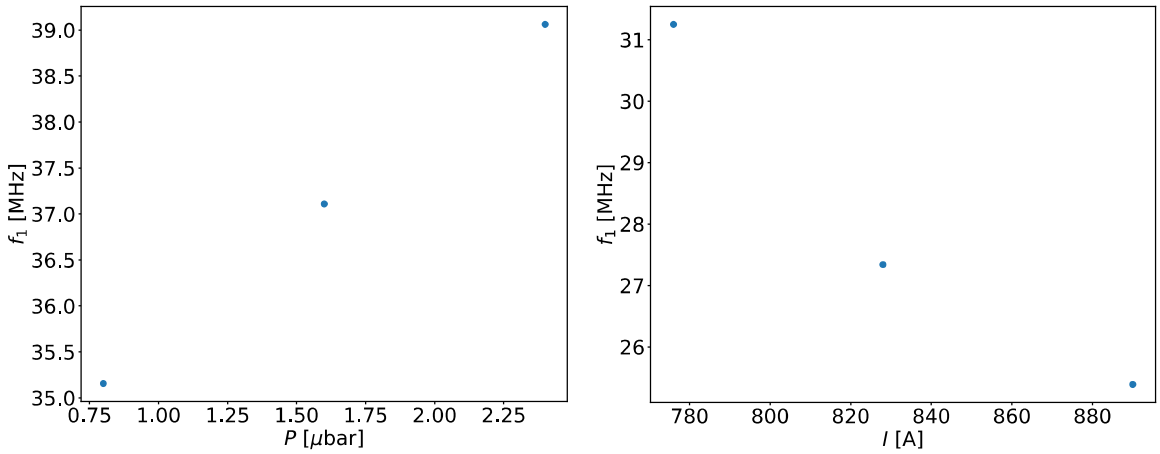

Figure 7.6: Measured LH daughter frequencies with 900 W LFS and 3 kW HFS power at different background pressure(left) and field (right). The measured coil current is used as a proxy for the field. The LH frequency rises with the pressure and decreases with higher field

As expected the LH frequency rises with the background pressure as it leads to a higher density. The behaviour of the frequency with the magnetic field cannot be explained immediately. While it is true that to a lower field corresponds a lower LH frequency according to the analytical model (2.79), it is also true that changing the field moves the position of the UH layer, affecting the effect of the heating on the density profile and so having an effect that is difficult to predict without a simultaneous measurement of the density profile. When moving to even higher fields, the LH peak stops being visible while moving to lower fields does not allow the plasma to form. To explain this behaviour, the geometrical configuration of the system was studied with a ray-tracing code, Warmray, to check the position of the resonances inside the machine. While for these studies NORTH has been run without poloidal field, and so not as a proper tokamak as assumed in Warmray, the results should not be significantly different as long as the density gradient between the center and the edges is low and representative of the system under study. These should be taken as preliminary results and a more thorough study will be possible when the probe array currently under development will allow measuring the entire density profile during every shot. Considering the maximum on-axis field supported by the machine of $B = 0.08$ T, the same low and high-density case studied in chapter 4 corresponding to $n_e = 0.75 \cdot 10^{16}\mathrm{m}^{-3}$ and $n_e = 5 \cdot 10^{16}\mathrm{m}^{-3}$ are reported in Fig. 7.7

It can be seen how the both the EC and UH resonance are near the center of the machine and that the UH resonance moves towards higher radii with increasing density. The X waves will travel through the EC resonance first, which will absorb a fraction of the power and it is a possible explanation on why the LH wave was not observed when operating at these high fields. Lowering the field to $B = 0.585$ T, corresponding to $I = 780$ in Fig. 7.6, leads for the high-density case to the results shown in Fig. 7.8

By lowering the field, the EC resonance moves past the injection point and so the waves reach directly the UH resonance without being absorbed first. While there is an intersection between the X waves and the EC resonance, it is outside the plasma, where the absorption will be negligible. In the low density case the UH layer will also be shifted to lower radii, past the injection point. For the UH resonance to exist the plasma needs to be formed first, but a possible explanation is that the plasma

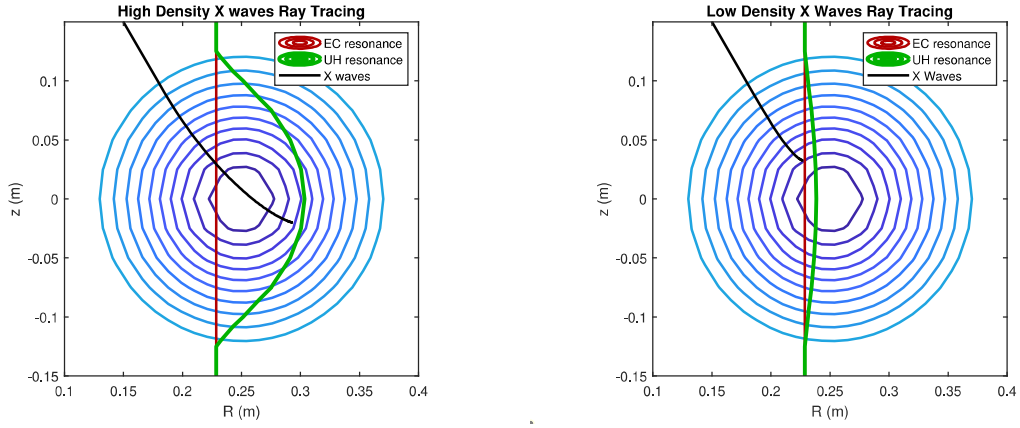

Figure 7.7: Ray tracing using Warmray with a field of $B = 0.08$ T and an on-axis density of $n_e = 5 \cdot 10^{16}\mathrm{m}^{-3}$ (right) and $n_e = 0.75 \cdot 10^{16}\mathrm{m}^{-3}$ (left).

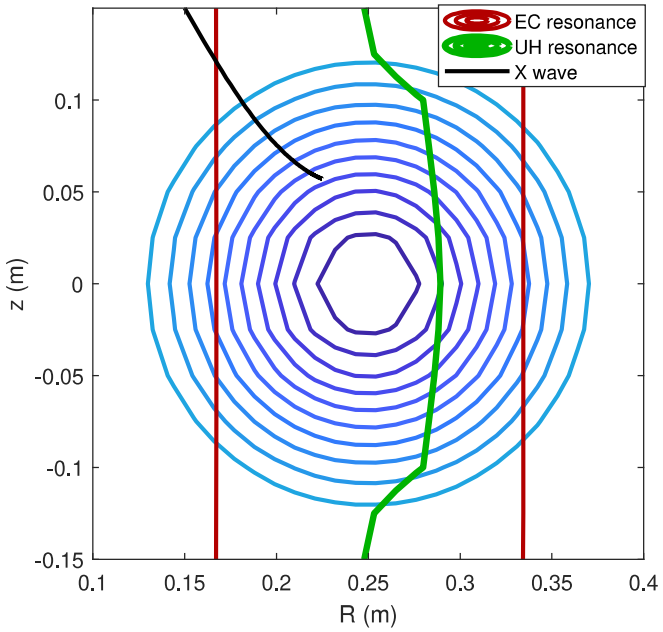

Figure 7.8: Ray tracing using Warmray with a field of $B = 0.585$ T and an on-axis density of $n_e = 5 \cdot 10^{16}$.

is initially formed by the X waves reaching the resonance after being reflected by the walls. As the density is raised, the UH resonance shifts to higher radii until it moves past the injection point and it contributes to the absorption, raising the density even further until steady state is reached. The measurement of the density profile is then important to determine the position of the UH resonance and so the distance from the injection point. When the probe array will be operational it will be possible to optimize the magnetic field configuration and shift the position of the resonance to maximize the efficiency of the parametric decay and study its properties.

Conclusions

In this work, the parametric decay of electron cyclotron resonance heating microwaves at the upper hybrid layer into lower hybrid and electron Bernstein waves in the NORTH tokamak has been investigated. An analytical model initially developed to study the same phenomenon on the ASDEX-U tokamak was used to make predictions on the power threshold of the instability and the frequency of the daughter waves. This allowed testing the validity of the model predictions on a system with very different scales than the ones for which the model was initially developed and in particular where the wavelength of the microwaves are comparable with the size of the machine. While both f_1 and P_{th} depend on the experimental conditions, the typical values predicted by the model are of $P_{th} \approx 100$ W and $f_1 \approx 20 - 30$ MHz for hydrogen, the operating gas found to have the larger f_1 between the choices available on NORTH. The predictions regarding f_1 were validated using particle in cell simulations with the EPOCH code, leading to similar results to the ones given by the analytical model. It was not possible to validate the P_{th} estimates using the EPOCH code due to the large computational requirements of running 2D simulations for the system of interest. A radiometer composed of an antenna and an electronic chain to mix down the frequency of the signal to values compatible with the sampling frequency of the ADC was developed. Using the radiometer it was possible to characterize the power dependence and spectrum purity of the magnetrons and measure the frequency stability of the generated microwaves. It allowed testing the parametric decay predictions experimentally by measuring the radiation coming out of the plasma, an approach similar to the one used to detect the parametric decay in ASDEX-U. Using the radiometer no high-frequency daughter waves could be detected. This is due to two effects: the strong signal of the high field side pump wave that could not be suppressed without also attenuating the daughter wave signal and the presence of additional background peaks generated by the low field side pump and non-ideal effects in the mixer covering the region of interest of the spectrum, at 10-30 MHz less than the high field side pump wave. The electron Bernstein waves were also looked for using an high-frequency Langmuir probe but they were not observed due to the same reasons. Evidence of the lower hybrid daughter waves was found, instead, using the probe. While many signals at the low frequencies were present, only a single peak was present where the low-frequency daughter wave was expected and, unlike signals at the other frequencies, the signal of interest scaled with power, pressure and magnetic field. Increasing the power and the pressure leads to an increase in n_e, which in turn increases f_1 while an increase in B leads to a decrease in f_1. The analytical model predicts an increase of f_1 with B if the density is kept constant, but changing B in a tokamak-like scenario leads to a shift in the position of the upper hybrid resonance and so also of the density, making the dependence on B more difficult to determine. The lower hybrid daughter signal was only observed when working with magnetic fields lower than the typical operating field of $B = 0.08$ T. A possible explanation for this, explored using the Warmray ray-tracing code, is likely to be that at lower field the injection happens past the electron cyclotron resonance and so the X waves reach the upper hybrid resonance without being strongly absorbed by the electron cyclotron resonance first.

In the future, better measurements will be possible that will allow measuring both the high and low-frequency daughter waves. In particular, the use of a suitable Notch filter will allow the suppression of only the pump wave without damping the daughter wave and the relevant region of the spectrum will be cleaned by exploring experiments using only the high field side and substituting the electronic chain with a fast digitizer. Measuring the electron Bernstein wave will also allow determining the lower hybrid signal among the background peaks more easily as the typical frequency difference between the background peaks is of $\approx$ 10-15 MHz, large enough to ascertain which peak respects the selection

rules along with the measured high-frequency daughter wave.
Further studies on parametric decay instabilities on NORTH are also expected, dealing for example with the parametric decay of 2nd harmonic X-waves, and they allow to develop the current understanding of the phenomenon further before testing it on larger experiments such as the W7-X stellarator. The developments in the field will then be useful to account for these effects in the design of the heating systems and the operating conditions of large scale reactors such as DEMO.

Bibliography

[1] Glasstone S and Lovberg R 2012 Controlled thermonuclear reactions: An introduction to theory and experiment

[2] Wesson J and Campbell D 2011 *Tokamaks* International Series of Monogr (OUP Oxford) ISBN 9780199592234 URL https://books.google.it/books?id=XJssMXjHUr0C

[3] Nielsen S, Gryaznevich M, Jacobsen A, Jensen T, Jessen M, Korsholm S, Rasmussen J, Salewski M, Senstius M, Naulin V, Nem R, Korsgaard M, Nilsson A, Dam F, Goltermann A, Pedersen A, Sutherland M, Aalto T, Hokkanen A, Salmi A and Tala T 2021 *Fusion Engineering and Design* **166** 112288 ISSN 0920-3796 URL https://www.sciencedirect.com/science/article/pii/S0920379621000648

[4] Eurofusion 2021 *NORTH, NORdic Tokamak device.* URL https://www.euro-fusion.org/media-library/photostories/highlights-from-2019/

[5] Landau L D and Lifshitz E M 1976 *Mechanics, Third Edition: Volume 1 (Course of Theoretical Physics)* 3rd ed (Butterworth-Heinemann) ISBN 0750628960 URL http://www.worldcat.org/isbn/0750628960

[6] Boyd R W 2008 *Nonlinear Optics, Third Edition* 3rd ed (USA: Academic Press, Inc.) ISBN 0123694701

[7] Chen F F 1974 *Introduction to plasma physics* (New York: Plenum Press)

[8] Swanson D 2003 *Plasma Waves, 2nd Edition* Series in Plasma Physics (Taylor & Francis) ISBN 9780750309271 URL https://books.google.it/books?id=l2X95_N6qk0C

[9] Gusakov E Z and Popov A Y 2017 *Plasma Physics and Controlled Fusion* **60** 025001 URL https://doi.org/10.1088/1361-6587/aa8fdf

[10] et al J F 2019 Generation of suprathermal ions in ecr heated plasmas in the stellarator tj-ii.

[11] Hansen S K, Jacobsen A S, Willensdorfer M, Nielsen S K, Stober J, Höfler K, Maraschek M, Fischer R and Dunne M G 2021 *Plasma Physics and Controlled Fusion* URL http://iopscience.iop.org/article/10.1088/1361-6587/ac0fd0

[12] Popov A Y and Gusakov E Z 2015 *Soviet Journal of Experimental and Theoretical Physics* **120** 147–154

[13] Hansen S, Nielsen S, Salewski M, Pedersen M and Stober J 2017 *Plasma Physics and Controlled Fusion* **59** ISSN 0741-3335

[14] Senstius M, Nielsen S, Vann R and Hansen S 2020 *Plasma Physics and Controlled Fusion* **62** ISSN 0741-3335

[15] Stix T 1992 *Waves in Plasmas* (American Inst. of Physics) ISBN 9780883188590 URL https://books.google.it/books?id=OsOWJ8iHpmMC

[16] Amano T and Okamoto M 1969 *Journal of the Physical Society of Japan* **26** 529–540 (*Preprint* https://doi.org/10.1143/JPSJ.26.529) URL https://doi.org/10.1143/JPSJ.26.529

[17] Hansen S 2019 *Parametric Decay Instabilities in the Electron Cyclotron Resonance Heating Beams at ASDEX Upgrade* Ph.D. thesis

[18] Senstius M 2020 *Simulations of Three-Wave Interactions in Microwave Heated Fusion Plasmas* Ph.D. thesis

[19] Bellan P M 2006 *Fundamentals of Plasma Physics* (Cambridge University Press)

[20] Hansen S 2016 *Parametric Decay and Anomalous Scattering from Tokamak Plasmas* Master's thesis Technical University of Denmark

[21] Porkolab M 1974 *The Physics of Fluids* **17** 1432–1442 (*Preprint* https://aip.scitation.org/doi/pdf/10.1063/1.1694910) URL https://aip.scitation.org/doi/abs/10.1063/1.

1694910
[22] Porkolab M 1978 *Nuclear Fusion* **18** 367–413 URL https://doi.org/10.1088/0029-5515/18/3/008
[23] Kasymov Z Z, Näslund E, Starodub A N and Stenflo L 1985 *Physica Scripta* **31** 201–204 URL https://doi.org/10.1088/0031-8949/31/3/008
[24] Weiland J and Wilhelmsson H 1977 *Oxford Pergamon Press International Series on Natural Philosophy* **88**
[25] Berger R L, Chen L, Kaw P K and Perkins F W 1977 *The Physics of Fluids* **20** 1864–1875 (*Preprint* https://aip.scitation.org/doi/pdf/10.1063/1.861804) URL https://aip.scitation.org/doi/abs/10.1063/1.861804
[26] Rosenbluth M N 1972 *Phys. Rev. Lett.* **29**(9) 565–567 URL https://link.aps.org/doi/10.1103/PhysRevLett.29.565
[27] Arber T D, Bennett K, Brady C S, Lawrence-Douglas A, Ramsay M G, Sircombe N J, Gillies P, Evans R G, Schmitz H, Bell A R and Ridgers C P 2015 *Plasma Physics and Controlled Fusion* **57** 113001 URL https://doi.org/10.1088/0741-3335/57/11/113001
[28] Hansen S K, Nielsen S K, Stober J, Rasmussen J, Salewski M and Stejner M 2019 *Physics of Plasmas* **26** 062102 (*Preprint* https://doi.org/10.1063/1.5091659) URL https://doi.org/10.1063/1.5091659
[29] Hutchinson I H 2002 *Principles of Plasma Diagnostics* 2nd ed (Cambridge University Press)
[30] Stangeby P 2000 The Plasma Boundary of Magnetic Fusion Devices The Plasma Boundary of Magnetic Fusion Devices. Series: Series in Plasma Physics